

CURRENT INDUCED SPIN DYNAMICS IN ANTIFERROMAGNETS

by

Egecan Cogulu

A DISSERTATION SUBMITTED IN PARTIAL FULFILLMENT

OF THE REQUIREMENTS FOR THE DEGREE OF

DOCTOR OF PHILOSOPHY

DEPARTMENT OF PHYSICS

NEW YORK UNIVERSITY

MAY, 2022

Prof. Andrew D. Kent

© EGECAN COGULU

ALL RIGHTS RESERVED, 2022

DEDICATION

To my parents Nurgül and Ruhi and to my partner Erica, for their love and support.

ACKNOWLEDGEMENTS

I am grateful to the many people who helped me — academically and personally — during my time at New York University.

First of all, I would like to thank my thesis advisor Prof. Andrew Kent. Without his continuous support and mentorship, I wouldn't be the researcher that I am today. He guided and pushed me to become a better physicist while always being kind and caring. It was a great pleasure to be a part of the Kent Lab, I couldn't ask for a better environment or an advisor. I also would like to thank the members of my thesis committee Prof. Aditi Mitra, Prof. Javad Shabani, Prof. Dries Sels. and Prof. Andrew MacFadyen for their valuable feedback on my work over the years.

I was lucky to work with many wonderful members of the Kent group over the years: Debansu Roy, Laura Rehm, Eason Chen, Volker Sluka, Jamileh Beik Mohammadi, Junwen Xu, Yasmine Quessab and Nahuel Statuto. I thank them for their friendship and for all the things they taught me. Also, I am thankful to many collaborators that I had to pleasure to work with: Hendrik Ohldag, Rajesh Chopdekar, Alpha N'Diaye, Arun Parthasarathy, Yang Cheng, Hantao Zhang, Prof. Fengyuan Yang and Prof. Ran Cheng. Without their help, the works highlighted in thesis wouldn't be possible. And I would like to thank my professor from Bogazici University, Prof. Ozhan Ozatay who gave me the opportunity to be an undergraduate researcher in his lab and helped me to get into graduate school, without him I wouldn't be at New York University, in the first place.

I would also like to thank my close friends and roommates Talha Can İşsevenler and Muath

Natsheh for the good memories and for their support over the years. Also my friends from high school and university who made my transition from Istanbul to New York a fun and enjoyable experience: Ali Kavakdere, Cemil Dibek, Çağın Arlsan, Çağla Çimendereli, Deniz İnal, Hakan Memişoğlu, Sercan Altundemir, Yalçın Özhabeş and Zeynep Ekmekçi. I never felt alone or homesick thanks to them especially in my first few years in New York.

I would like to thank my family, especially my mom Nurgül Sarıbulbul and my dad Ruhi Çoğulu for always believing in me and supporting me with their love and compassion. And finally, I am grateful to my partner Erica Kotta for her love, support and for being a continuous inspiration for me. The best part of graduate school was meeting her and I look forward to next step in our lives. I also have to thank her for convincing me to adopt our cat Pokki.

Also I would like to acknowledge the funding agencies and programs for supporting my work over the years: "Quantum Materials for Energy Efficient Neuromorphic Computing (Q-MEEN-C) an Energy Frontier Research Center funded by the U.S. Department of Energy (DOE), Office of Science, Basic Energy Sciences (BES), under Award DE-SC0019273", "National Science Foundation NSF-DMR-2105114", "National Science Foundation NSF-DMR-1610416", "Air Force Office of Scientific Research under Grant No. FA9550-19-1-0307" and "MRSEC Program of the National Science Foundation under NSF-DMR-1420073."

ABSTRACT

This thesis focuses on experimental investigations of detection and control of Néel order in insulating antiferromagnetic thin films, specifically α -Fe₂O₃ and NiO. Antiferromagnetic materials have been getting increasing attention from the spintronics community because of their interesting properties and for potential applications in information processing. Some of these properties are zero net magnetization, low magnetic susceptibility, and very fast intrinsic spin dynamics with frequencies in the THz regime. Detecting and manipulating antiferromagnetic order electrically and reliably is a crucial milestone for realizing antiferromagnetic devices, but also an experimentally challenging one.

Magnetic switching reported in antiferromagnetic thin films thus far is overwhelmingly based on electronic transport methods, which provide only spatially averaged information on antiferromagnetic states. In addition, the resulting magnetoresistance from switching is usually less than 1% and can be masked by other effects due to the large current densities (e.g. electromigration, heating, thermal stresses, etc.). So, it is not always possible to identify the source of the observed magnetoresistance signal. To tackle this problem, we first took a direct approach of imaging the magnetic domains using soft X-rays, with a technique known as X-ray Magnetic Linear Dichroism - Photoemission Electron Microscopy (XMLD-PEEM). This technique takes advantage of the dependence of the absorption of incoming light on its polarization and the underlying anisotropies of the material – in this case magnetic ones. The main advantage of using a microscopy technique is that it can provide local information on antiferromagnetic domains which can help to reveal the

principal switching mechanism. In our experiments, we observed the repeatable current-induced switching of antiferromagnetic moments consistent with the electrical measurements. Our analysis of individual light polarizations as a function of sample rotation revealed the position of the Néel vector in 3D space. Furthermore, we identified two types of switching based on the location and repeatability: reversible and irreversible switching. For regions that switch once and are outside of current path, magneto-elastic effects are the most likely dominant switching mechanism. But for reversible and along the current path regions, both spin-orbit-torques and magnetoelastic could be the contributors.

Our second approach for understanding current-induced antiferromagnetic dynamics was to design and conduct an experiment that measures the torque on the Néel vector. This is done with harmonic Hall measurements in antiferromagnet/heavy metal bilayer structures. Harmonic measurements on ferro- and ferrimagnetic systems have been used before to characterize spin-orbit torques (SOT), which are one of the most effective ways to manipulate magnetic order. However, their effectiveness is less well-explored and quantified for antiferromagnets. SOT are a result of the spin-Hall effect in the heavy metal, in which a charge current leads to a spin accumulation at the interface. They can modify the orientation of the AFM Néel vector and this change can be detected electrically because of spin Hall magnetoresistance. In our work, we demonstrated a way to extract SOTs by fitting harmonic responses to a simple model. Surprisingly, we found that the field-like torques are two orders of magnitude larger than damping-like torques in our α -Fe₂O₃ /Pt heterostructures, implying that the spin-mixing conductance of the interface has the unusual property of having a large imaginary component. This also points to magneto-elastic effects likely being the dominant mechanism of current-induced switching studies.

We also used harmonic measurements to detect spin transport in ferrimagnet/ antiferromagnet/ heavy metal trilayer heterostructures. A spin current generated by a thermal gradient – also known as the spin Seebeck effect – in a ferrimagnet can travel across antiferromagnetic NiO layer and be detected by inverse spin-hall effect in the heavy metal layer. Our results showed that not

only is spin transport possible through thin NiO layers but there is also a sharp increase in the spin Seebeck effect magnitude at intermediate temperatures. These results suggest that this technique can be used to characterize the response of thin antiferromagnetic materials and optimize their spin-transport characteristics.

In summary, we first show control of antiferromagnetic order using electrical pulses while detecting the resulting changes using x-rays. Then, we used harmonic measurements to quantify spin-orbit torques present in the same system. We also extended the harmonic studies to trilayer structure to explore spin transport across antiferromagnetic layer. Overall, our studies open up a promising path for future studies similar AFM/HM heterostructures, as well as a means that can be used in optimizing SOT on AFM for applications.

CONTENTS

Dedication	iii
Acknowledgments	iv
Abstract	vi
List of Figures	xiii
List of Tables	xxvi
1 Introduction	1
1.1 Antiferromagnetism and Spintronics	1
1.2 The Terahertz Gap and Applications of Antiferromagnets	3
1.3 Antiferromagnetism	5
1.3.1 Magnetic Energies	6
1.3.2 Néel Vector	11
1.3.3 Magnetic Susceptibility	12
1.4 Detecting Antiferromagnets	15
1.4.1 Spin Hall Effect and Inverse Spin Hall Effect	15
1.4.2 Spin Hall Magnetoresistance	18
1.4.3 Harmonic Measurements	20

1.4.4	X-ray Magnetic Dichroism	22
1.5	Controlling Antiferromagnets	25
1.5.1	External Field	25
1.5.2	Spin-Orbit Torques	26
1.5.3	Magneto-elastic Effects	27
1.6	Dynamics of Antiferromagnets	28
1.6.1	Landau-Lifshitz-Gilbert Equation	30
1.6.2	Spin Torques	30
1.7	State of the Art and Overview of Dissertation	32
1.7.1	Antiferromagnetic Oscillator	32
1.7.2	Subterahertz Spin Pumping from Antiferromagnet	34
1.7.3	Electrical Switching of an Antiferromagnet	35
1.7.4	Overview of the Dissertation	39
2	Imaging Antiferromagnetic Order using X-Rays	41
2.1	Introduction	41
2.2	Imaging Experiments on α -Fe ₂ O ₃	42
2.2.1	Sample Characteristics	42
2.2.2	Experimental Setup	43
2.2.3	Electrical Measurement Configuration	45
2.2.4	Imaging Antiferromagnetic Domains	47
2.2.5	Imaging Current Induced Changes	50
2.2.6	Spin contrast from XMLD images	58
2.2.7	Spins canted out-of-plane equilibrium state	61
2.2.8	Current distributions	63
2.2.9	Temperature profiles	65

2.2.10	Stress Distributions	68
2.2.11	Conclusion	69
2.3	Imaging Experiments on NiO	69
2.3.1	Sample Characteristics	70
2.3.2	Experimental Setup	71
2.3.3	Imaging Antiferromagnetic Domains	72
2.3.4	Conclusion	75
3	Quantifying Spin Orbit Torques using Harmonic Measurements	76
3.1	Introduction	76
3.2	Sample Characteristics and Experimental Setup	77
3.3	Modeling the Harmonic Response	79
3.4	Separating the Hall Effect and the Spin Seebeck Contributions	84
3.5	Spin-mixing Conductance of the AFM/HM Interface	86
3.6	Field Dependence of the Harmonic Signal	88
3.7	Finite Element Simulations of Oersted Fields	89
3.8	Current Dependence of Harmonic Signals	90
3.9	Effects of Field-like and Damping-like Torques	91
3.10	Calculation of the spin-mixing conductance	93
3.11	Conclusion of the Chapter	96
4	Conclusion and Perspectives	98
A	Appendix	104
A.1	Sample Characteristics and Measurement Geometry	104
A.2	Measuring the Spin Seebeck Effect	105
A.3	Temperature Dependence of the Spin Seebeck Effect	107

A.4	Field Dependence of the Spin Seebeck Effect	108
A.5	Thickness and Temperature Dependence of the Exchange Bias Effect	109
Bibliography		111

LIST OF FIGURES

1.1	Schematic representation of spin configurations for different types of magnetism in solid materials. (a) Ferromagnetism is the configuration where spins are aligned in parallel to create a net magnetic moment. (b) Ferrimagnetism is the configuration where spins are aligned in antiparallel fashion but opposing magnetic moments are not equal in magnitude, so there is still a non-zero moment. (c) In antiferromagnetism, spins are aligned in anti-parallel fashion and they are equal in magnitude so they cancel each other out. (d) In paramagnetism, thermal energy is strong enough to shuffle the spins in random directions, so they are not ordered. It is also the state, ferromagnets, ferrimagnets and antiferromagnets transition above their critical temperatures T_c and T_N	2
1.2	The electromagnetic spectrum and some example technologies that work on the specific wavelengths. The terahertz gap is between the highest frequencies of the radio spectrum and lowest frequencies of optical infrared detectors. The figure is adapted from [4].	5

1.3	Crystal structures and spin arrangements of the antiferromagnets α -Fe ₂ O ₃ and NiO. (a) Hexagonal crystal structure of α -Fe ₂ O ₃ is shown with magnetic moments of Fe atoms coupled ferromagnetically inside the [0001] planes and antiferromagnetically across them. (b) Cubic crystal structure of NiO with Ni moments coupled ferromagnetically inside [111] easy planes and antiferromagnetically across them. Inside the [111] easy-planes [11 $\bar{2}$] directions are the easy axes.	6
1.4	(a) Dzyaloshinskii–Moriya interaction generated by antisymmetric exchange of two atomic spins and an atom with a strong spin-orbit coupling. (b) Interfacial DMI generated at the interface of a magnetic and metallic layer. Figures are adapted from [6].	11
1.5	Comparison of magnetic susceptibilities of (a) paramagnets, (b) ferromagnets and (c) antiferromagnets. For antiferromagnets, below the Néel temperature, T_N , there are two different magnetic susceptibilities: χ_{\parallel} and χ_{\perp} . These are susceptibilities parallel and perpendicular to easy axes respectively. The figure is adapted from [7].	14
1.6	Schematic representation of different types of (a) spin Hall effect and (b) inverse spin Hall effect. Through these mechanisms spin currents and electrical currents inside a metal wire, can be converted to one another.	17
1.7	Illustrations of mechanisms that give rise to the spin Hall Effect. Red and blue electrons are spin-up and spin down electrons. Green spheres are the scattering locations. And the green arrows represent the magnetic fields. (a) Extrinsic spin skew scattering, (b) extrinsic side-jump scattering, (c) intrinsic SHE coming from the band structure of the metal. Figure is adapted from [15].	18

1.8	Comparison of ferromagnetic (top row) and antiferromagnetic (bottom row) spin Hall magnetoresistance (SMR). The magnitude of SMR is based on conversion of charge currents J_c and spin currents J_s . In both ferromagnetic insulator (FMI) and antiferromagnetic insulator (AFI) cases, the resistance of the heterostructure is large when the spin current back flow is small J_s^{back} (a,e). And the resistance is small when J_s^{back} is large (b,d). The main difference is caused by difference in coupling of FMI and AFI to the external field. FMI couples in a parallel fashion whereas AFI couples perpendicularly. This causes a 90° shift on angular dependence of SMR between FMI and AFI. Figure is adapted from [22].	21
1.9	(a) Demonstration of XMLD effect on NiO absorption spectrum. Linearly polarized light yields different amounts of photoelectrons at Ni L_2 edge energies, depending on the underlying domain structure. (b) Demonstration of XMCD effect on Fe absorption spectrum. Circularly polarized light yields different amounts of photoelectrons at Fe L_2 and L_3 edge energies, depending on the underlying domain structure. The figure is adapted from [25].	23
1.10	(a) Schematic of the experimental geometry of photoemission electron microscopy. (b) Illustration of generation and scattering of secondary electron which mostly probe the top 2-10 nanometers of the sample surface. The figure is adapted from [25].	24
1.11	Magneto-elastic energy in α -Fe ₂ O ₃ /Pt Hall bars with 10 μ m channel width as a function of angle of external magnetic field at different magnitudes of (a) positive and (b) negative currents. Inset in (a) shows magnetostriction effect induced by compressive stresses associated with Joule heating in a Hall-bar. Figure is taken from [31].	28

1.12	(a) Precession of magnetization around an effective magnetic field H_{eff} , according to the LLG equation. Blue arrow represents the torque associated with H_{eff} which drives the precession. Red arrow represents the Gilbert damping torque, which makes the magnetization settle decay into equilibrium. (b) Spin torque, τ_{ST} , in the form on anti-damping, $\mathbf{m} \times (\mathbf{p} \times \mathbf{m})$, counteracts the effect of damping and keeps the precession going.	31
1.13	(a) An insulating AFM/HM heterostructure. Current density J_c creates a spin accumulation at the interface, which in turn drives the AFM. The detection is done by two voltmeters detecting the resistance changes via spin-Hall magnetoresistance. (b) Phase diagram of a SHNO based on NiO/Pt bilayer structure, showing stable oscillations and proliferation phases. Figures are taken from [34]	33
1.14	Illustration of spin-pumping from antiferromagnet Cr_2O_3 and spin current injection to heavy metal Pt. (b) Magnetic-resonance frequency as a function of the applied magnetic field along c axis of Cr_2O_3 . Eigenmodes of right-handed (c) and left-handed (d) antiferromagnetic resonance (AFMR). (f) Eigenmode of quasiferromagnetic resonance (QFMR) after spin-flop field. Figure is taken from [35].	34
1.15	Evolution of spin dynamics of MnF_2 across the spin-flop transition. Illustration of sublattice magnetizations M_1 and M_2 at 4 different resonance points as a function of applied magnetic field. Figure is taken from [36].	35
1.16	(a) Optical microscopy image of the 8-legged device and schematic of the measurement geometry. (b) Change in the transverse resistance after applying writing pulses. Figure is adapted from [37].	36
1.17	(a) Crystal structure, tri-axial anisotropy and schematic of the eight-leg Hall cross of Fe_2O_3 / Pt bilayer. Figure is adapted from [29].	37

1.18	(a) Electrical "switching" signal in transverse resistance of Pt grown on Si, MgO and glass substrates, without any antiferromagnetic layer. (b) Comparison of transverse resistances in NiO/Pt and only Pt. All samples show saw-tooth behavior which is associated with electromigration in Pt, rather than antiferromagnetic switching. Figures are adapted from [41, 42].	38
2.1	(a) Hexagonal crystal structure of antiferromagnetic α -Fe ₂ O ₃ . Fe moments are ferromagnetically coupled within c-planes, and antiferromagnetically coupled across c-planes. (b) STEM image of the cross section of α -Fe ₂ O ₃ (30)/Pt (2) bilayer. The inset shows the atoms with higher adjusted brightness. (c) X-ray diffraction of epitaxially grown α -Fe ₂ O ₃ on Al ₂ O ₃ . $2\theta / \omega$ scan shows α -Fe ₂ O ₃ (006) peak indicating high crystalline quality. Figure is adapted from [29].	43
2.2	σ and π polarizations of x-rays and their projections on the sample at ALS PEEM3 Beamline 11.0.0.1. In rotation experiments, the sample was rotated by the small azimuthal angle ϕ , projections along π and σ polarizations can be varied.	44
2.3	(a) Commercially available leadless chip carrier that holds the sample. There are total of 6 possible connection where 2 of them are connected to the ground. (b) Custom PEEM sample holder for electrical measurements at ALS Beamline 11.0.1.1.	45
2.4	(a) Circuit diagram for measuring the Hall voltage of 6-legged Hall-cross. (b) Transverse resistance measurements in response to 4 mA, 10 ms pulses A and B along two of leads coinciding with easy-axes. The two-point resistance of the sample measured is approximately 5 k Ω . The resistors are chosen so that they compensate for the small differences in resistance coming from different leads. . .	46

2.5	Switching amplitude as a function of pulse width and pulse amplitude (a) Heat-map. (b) 3-D Phase diagram. Both of the plot show the same data, just different representation.	47
2.6	Figure 2. (a) Optical microscopy image of the original 8-legged Hall-cross. Field of view is 0.5 mm (b) XMLD-PEEM image of antiferromagnetic domains in the same sample. (c) XMLD-PEEM image of antiferromagnetic domains in the 6-legged Hall-cross. Dark regions are Pt and bright regions are bare α -Fe ₂ O ₃ . In both samples, domains are visible in bare regions and through the 2 nm platinum layer. Images are calculated by taking asymmetry at L _{2a} and L _{2b} edges and normalized to L ₂ pre-edge. Field of view is 5 μ m.	48
2.7	XMLD-PEEM Images of the region of interest before (a) the pulse. Both images are calculated by taking asymmetry of L _{2a} and L _{2b} edges, then normalizing with L ₂ pre-edge. (b) Asymmetry of before and after images. Antiferromagnetic domain structure shows small changes after the current pulse, which can be seen as black and white spots in the image. Largest changes are circled in yellow. Field of view is 10 μ m.	49
2.8	(a) Schematic of the experimental setup showing the two incident X-ray polarizations, σ and π , and their projections on the sample. The sample was rotated by a small azimuthal angle, ϕ , so that the [1000] and [0100] crystal axes have different projections along π and σ polarizations. (b) XMLD-PEEM image of the 6-legged Hall cross with AFM domains visible both on bare Fe ₂ O ₃ regions (lighter regions) and under the 2 nm thick Pt layer (darker regions). The scale bar indicates the percentage contrast, relative the to background.	50

2.9	(a) Left: PEEM image with a schematic of the circuit. Bright regions correspond to Pt covered areas and dark regions to bare Fe_2O_3 . Pulses were applied from “+” to the ground, “-”, for both pulse generators. Right: Pulse A and Pulse B panels show the current path for each pulse. The dark line at the bottom of the central part of the Hall cross is a cut disconnecting the two bottom leads from the current path. (b) Transverse resistance measurements in response to 4 mA, 10 ms pulses A and B on a sister sample with the bottom leads connected.	51
2.10	AFM domain changes in response to current pulses. (a) XMLD images showing a $4 \times 4 \mu\text{m}^2$ field of view. Image I shows the sample before current is applied; Images II, III and IV are images taken after the application of 20 current pulses of type A, type B and then type A, respectively. The pulse amplitude is 4 mA for all the images in the sequence. (b) Differences of XMLD images in panel (a) to highlight the pulse induced changes to AFM domain structure. The color scale in (b) is expanded to highlight changes.	52
2.11	(a) σ and π projections of Image III in Fig. 2.10a. Bright regions indicate that the AFM order is aligned perpendicular to the polarization direction whereas dark regions indicate that the AFM order aligns parallel to the polarization direction. (b) σ (top panel) and π (bottom panel) projections of the difference images in Fig. 2.10b. The same scale bar is used on both panels to highlight the larger contrast in the π polarization images. The marks on the σ color scale bar show the maximum and minimum values for σ (red marks) and π (blue marks) polarization difference images.	54

2.12	AFM domain response to larger amplitude current pulses. (a) Image I shows the initial sample state which is State A. Followed by images II, III and IV taken after $20 \times B$ pulses, $20 \times A$ pulses and $20 \times B$ pulses respectively. In each case the current amplitude was 6 mA. (b) Differences of XMLD images in panel (a) highlight the pulse induced changes, with an expanded color scale, the same as the that of Fig. 2.10(b).	56
2.13	Schematic of the switching of the Néel vector between easy axis directions that cant out of the film plane, which is consistent with both the XMLD-PEEM results and the Hall response. \vec{n}_A and \vec{n}_B are the orientations of the Néel vector after Pulse A and Pulse B respectively. The dotted lines with arrows shows the switching direction of the Néel vector in response to the pulses. These arrows associated with Pulse A and Pulse B correspond to blue and red changes, respectively, in the difference images in Fig. 2.10(b) and Fig 2.12(b).	58
2.14	Lower panel: Absorption spectra of α -Fe ₂ O ₃ showing the photo-electron intensity versus x-ray energy. Arrows indicate pre-L ₂ , L _{2a} and L _{2b} Fe edges at 718, 721.4 and 723 eV, respectively. Top panel table shows PEEM images obtained at the different photon energies (columns) and polarizations (rows).	59
2.15	A schematic of the steps for creating the final XMLD images from images taken with polarizations σ and π and at energies -pre-L ₂ , L _{2a} and L _{2b}	60
2.16	Polarization σ and polarization π projections as a function of in-plane sample rotation angle ϕ . The images are taken from an unpatterned Pt(2)/ α -Fe ₂ O ₃ (30) sample that was grown under the same conditions as that of the patterned samples studied. All images were aligned with respect to each other and use the same color scale. The red square is there to highlight the same particular sample region in all six images.	62

2.17	(a) Current distributions for pulse A and pulse B configurations. Labels at the edge of leads show where each pulse originates and terminates. The flux of the streamlines is proportional to the magnitude of the current density. (b) Angle between current distributions for pulse A and pulse B at each point of the Hall cross. (c) Norm of cross product of current distributions A and B.	64
2.18	Finite element simulations for temperature distribution in both pulse configurations, for both pulse amplitudes. The block size is $5 \times 5 \times 5 \text{ } \mu\text{m}^3$. Two bottom leads of the Hall cross are omitted because they were electrically disconnected.	65
2.19	(a) Current density amplitude and (b) temperature gradient profiles across the leads, for pulse A and pulse B configurations.	66
2.20	Finite element simulations for stress distributions σ_{xx} and σ_{yy} in both pulse configurations, for both pulse amplitudes.	68
2.21	(a) FCC crystal structure of NiO. Ni (red and blue) moments are along the confined to the $\{111\}$ easy-planes and along the easy axis $\langle 11\bar{2} \rangle$. Because of the cubic symmetry of the crystal there are four equivalent $\{111\}$ planes and 3 equivalent $\langle 11\bar{2} \rangle$ directions. (b) 3 equivalent $\langle 11\bar{2} \rangle$ directions within the easy plane. Figure is taken from [61]	71
2.22	Illustration of geometry of incident X-rays and polarizations. Black arrow represents the Poynting vector of incoming x-rays with a grazing angle of 18° . The gray square represents the sample surface. Polarizations 100, 123, 145 167 and 190 are represented by arrows with different colors as indicated. All polarization lie in a plan that is perpendicular to the plane normal to the Poynting vector.	72
2.23	XMLD-PEEM image of NiO sample as a function of sample rotation and x-ray polarization. All images show roughly the same area indicated by the defect on the sample. Blue and red arrows indicate the relative orientation of sample. Field of view is $7 \text{ } \mu\text{m}$	73

2.24	Relative XMLD contrast in arbitrary units as a function of x-ray polarization for (a) majority domains and (b) minority domains. The dots are the data points and the lines are the fits with crystal field.	74
3.1	a) Transverse measurement configuration showing the Pt Hall cross with 5 μm channel width. An AC current J_{AC} is applied in the \hat{x} -direction, and the transverse voltage V_{xy} is measured with a lock-in amplifier. b) Modeling geometry. D represents both the DMI vector and the hard axis direction that defines the easy plane. \mathbf{m}_1 and \mathbf{m}_2 are the sublattice moments and \mathbf{H} is the external magnetic field. The spin accumulation σ_{AC} is in the \hat{y} -direction. The resulting spin-orbit torques on the sublattice moments are decomposed into field-like (τ_{FL}) and damping-like components (τ_{DL}).	78
3.2	Angular dependence of 1 st and 2 nd harmonic (columns) resistance signals in XY, XZ and YZ scans (rows) at $\mu_0 H = 3$ T. The current amplitudes are 100 μA and 1.5 mA in the 1 st and 2 nd harmonic measurements, respectively. The blue dots are the data points whereas, the red line is the fit resulting from the model. The geometry of magnetic field scans in the 3 principal planes (XY, XZ and YZ scans) and the definition of the angles α , β and γ are shown at the top. The magnitude of longitudinal SMR is approximately 0.02% and it is consistent with studies on similar AFM/HM systems [21, 31]	80

- 3.3 Separating Hall effect and spin Seebeck effect contributions. a) Field dependence of 1st harmonic response in YZ scan, from 0 to 8 T as indicated by the legend. b) The Hall effect in 1st harmonic YZ scan (a), as a function of applied field. The linear trend line supports the claim that the origin of the signal is the ordinary Hall effect. c) Field dependence of 2nd harmonic response in XY scan, which shares the same legend as (a). d) Antiferromagnetic spin Seebeck effect (SSE) separated from field-like SOT in 2nd harmonic XY scan (c), as a function of applied field. The field-like component scales as $1/H$, whereas the SSE component scales linearly with H 85
- 3.4 a) Imaginary (left) and real (right) parts of the spin mixing conductance ($g = g_r + ig_i$) of an AFM/NM interface. The scale is indicated by the shared color bar on the right, with units of \hbar per unit area a^2 on the interface, where a is the lattice constant. b) Ratio of $|g_i|$ to $|g_r|$. As λ approaches zero $|g_i|$ dominates over $|g_r|$. The dashed line shows $|g_i| = |g_r|$, which separates the field-like torque dominating region ($g_i > g_r$) on the left from the damping-like torque dominating region ($g_r > g_i$) on the right. The color bar scale is logarithmic in this case. The inset shows a line cut of g_r and g_i vs. λ at $\delta=0.25$. Even though they both approach zero as λ goes to zero, g_r decreases faster than g_i and their ratio g_i/g_r diverges. 87
- 3.5 Full angular dependence of 1st and 2nd harmonic (rows) resistance signals in XY, XZ and YZ scans (columns) as a function of magnetic field strength. External magnetic field strength is scanned from 0 to 9 T as indicated by the legend. Geometry of magnetic field scans in the 3 principal planes (XY, XZ and YZ scans) and the definition of the angles α , β and γ are shown at the top. The current amplitudes are 100 μA and 1.5 mA in the 1st and 2nd harmonic measurements, respectively. The current is always along \hat{x} direction and the resulting spin accumulation σ_{AC} is in the \hat{y} direction. 88

3.6	Finite-element simulation of Oersted fields created by a metal wire of dimensions of $5\ \mu\text{m} \times 5\ \text{nm}$. The current is in $+z$ direction which is perpendicular to the page. Yellow arrows show the direction of local magnetic field vector and are proportional to its magnitude. The contour color map also indicates the norm of the magnetic field. In very close vicinity of the Pt surface ($< 30\ \text{nm}$), the amplitude of the Oersted fields is around $2 \times 10^{-5}\ \text{T}$	89
3.7	Current dependence of 1 st and 2 nd harmonic voltages in log-log scale. The slopes of the curves indicates exponent of the current dependence ($V \sim I^n$). As expected, the 1 st harmonic voltage signal depends linearly on the current, whereas the 2 nd harmonic voltage depends quadratically on the current.	90
3.8	Time evolution of sublattice moments \mathbf{m}_1 and \mathbf{m}_2 under the effect of (a) external field only and (b) external field and field-like torque from a spin accumulation σ . In both cases external field \mathbf{H} is in \hat{x} -direction and in (b) σ is in \hat{y} - direction indicated by the coordinate axes. Transparent arrows represent the arbitrarily chosen initial state. In case (a) at equilibrium state \mathbf{n} is perpendicular to \mathbf{H} and in case (b) \mathbf{n} is perpendicular to vector addition of σ and \mathbf{H}	91
3.9	Time evolution of sublattice moments \mathbf{m}_1 and \mathbf{m}_2 under the effect of (a) external field and small damping like torques and (b) external field and large damping like torques. In both cases external field \mathbf{H} is in \hat{x} -direction and σ is in \hat{y} - direction similar to Fig. 3.8. Transparent arrows represent the arbitrarily chosen initial state. In case (a), at equilibrium state sublattice moments start to precess around the spin accumulation σ , but the anti-damping effect is not large enough to sustain the oscillations so it reaches equilibrium state that is perpendicular to \mathbf{H} . In case (b), the anti-damping effect is large enough to overcome damping and \mathbf{n} starts rotating in the XZ plane which is perpendicular to σ	93

3.10	a) Illustration of spin-flip scattering at the AFM/NM interface. b) Coordinate system on the interface. c) The region of integration is shaded, where k_y and k_z satisfy $2 \cos \frac{k_y a}{\sqrt{2}} \cos \frac{k_z a}{\sqrt{2}} < 1$. Figure is taken from [90].	95
A.1	Optical microscopy image of a Hall-bar structure. Darker regions are electrically insulating NiO and lighter regions are highly conductive Pt. The scale bars visible for each image.	105
A.2	(a) Schematic of sample and measurement geometry. The current is always is \hat{x} -direction and the magnetic field \vec{B} is scanned in the XY plane where the angle θ is measured from the x-axis. (b) Example fit of the second harmonic response at $T = 300$ K and $ \vec{B} = 0.5$ Tesla.	106
A.3	(a) Temperature dependence of the Spin Seebeck Effect on YIG/Pt and YIG/NiO/Pt layers. The sharp increase of amplitude only present in the sample with NiO. (b) .	107
A.4	SSE amplitude as a function of temperature at different external field amplitudes $ \vec{B} = 0.1, 0.5$ and 1 Tesla. The peak at 110 K is visible at all 3 curves but the amplitude of the peak clearly increases with increasing external field amplitude. .	108
A.5	(a) An example M-H curve of the tri-layer structure YIG/NiO(5)/Pt at $T = 50$ K. Coercive fields H_{c1} and H_{c2} are marked by green arrows and the average of the two coercive fields is calculated as exchange bias amplitude H_{ex} . (b) Exchange bias amplitude H_{ex} as a function of thickness of the NiO layer and the temperature.	109

LIST OF TABLES

1.1	Néel temperatures of some antiferromagnets.	12
2.1	Material properties used in COMSOL simulations at 293 K.	69

1 | INTRODUCTION

1.1 ANTIFERROMAGNETISM AND SPINTRONICS

Magnetism that we are familiar with from our daily lives, originates microscopically from the spin and orbital magnetic moment of electrons inside magnetic materials. While spin is an intrinsic property of the electron and correspondingly fixed magnetic moment, orbital magnetic moment depends on the specific atom that the electron is bound to. Interplay between spin, orbital magnetic moment and other sources, like coupling between electron spins and crystal structure of the material, can give rise to a wide range of behavior of magnetism inside solid state materials. The most common way to classify different types of magnetic materials, is to look how they behave with and without the presence of an external magnetic field. According to this classification, there are five major groups: ferromagnetism, ferrimagnetism, antiferromagnetism, paramagnetism and diamagnetism. For the context of this dissertation, the most relevant category is antiferromagnetism. But since it is defined by negation, it always makes sense to start talking about antiferromagnetism after a brief introduction to ferromagnetism.

Ferromagnetism is where the electrons inside a material align their spins in the same direction — usually this direction is set by an external magnetic field. This collective behavior of electrons, gives rise to macroscopic permanent or temporary magnets that we are all familiar with. Where as in antiferromagnetism, neighboring electrons align their spins in an anti-parallel fashion which results in zero net magnetic moment. In this context zero magnetic moment means, no

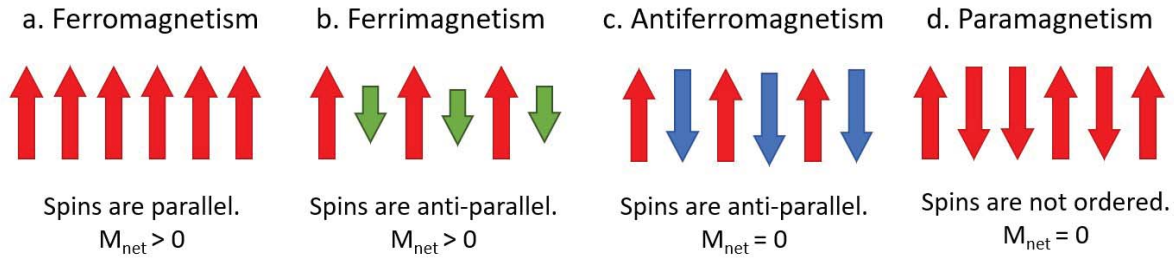


Figure 1.1: Schematic representation of spin configurations for different types of magnetism in solid materials. (a) Ferromagnetism is the configuration where spins are aligned in parallel to create a net magnetic moment. (b) Ferrimagnetism is the configuration where spins are aligned in antiparallel fashion but opposing magnetic moments are not equal in magnitude, so there is still a non-zero moment. (c) In antiferromagnetism, spins are aligned in anti-parallel fashion and they are equal in magnitude so they cancel each other out. (d) In paramagnetism, thermal energy is strong enough to shuffle the spins in random directions, so they are not ordered. It is also the state, ferromagnets, ferrimagnets and antiferromagnets transition above their critical temperatures T_c and T_N .

macroscopic magnetic behavior, but still, there is growing interest in antiferromagnetic materials, especially in the field of “spintronics.”

Spintronics, which is a blend of the words spin and electronics, is the study of the spin of the electron and its associated magnetic moment, in addition to its charge. The field emerged in 1980s with the discoveries of spin-polarized currents and associated magneto-resistance effects [1, 2], which can be summarized as spin-dependent electron transport phenomena in solid-state devices. Most of the initial efforts were focused on ferromagnetic materials, where various useful effects were discovered and studied extensively. During those times antiferromagnetic materials were flying under the radar, because of their hard-to-study nature. Their main use in those times was as passive layers to “pin” the direction of the magnetic moment of a ferromagnetic layer through what is known as the exchange bias effect. This effect uses the fact that AFM can have large magnetic anisotropies that can be “imprinted” on the ferromagnet and that AFM are insensitive to applied magnetic fields. But thanks to the advancement of the technology and our understanding of antiferromagnetism, today antiferromagnetic materials are gathering more and more attention. Antiferromagnets are considered promising for spintronic applications

thanks to their advantageous properties like high frequency internal dynamics, zero net magnetization which makes them insensitive to external magnetic perturbations and also the fact that they exhibit most of the well-studied effects of ferromagnetic materials in some form. Within this framework, we have decided to study insulating antiferromagnetic materials NiO and α -Fe₂O₃. The reason for the choice of these materials will become clear as we discuss our research goals.

1.2 THE TERAHERTZ GAP AND APPLICATIONS OF ANTIFERROMAGNETS

In his 1970 Nobel lecture, Louis Néel famously said for antiferromagnets: "They are for extremely interesting from the theoretical viewpoints, but do not seem to have any applications" [3]. From the theoretical point of viewpoint antiferromagnets are at least as interesting as ferromagnets, as they can be studied as two coupled ferromagnets in an antiparallel fashion. The main reason it seemed like antiferromagnets don't have any applications, is because they are very unresponsive to external manipulation, as well as their magnetic data susceptibility looked like that of paramagnets.

Interestingly nowadays, this same property is considered to be an advantage, as it allows close packing of bits compared to ferromagnets in potential devices. Since antiferromagnets produce weaker stray fields and are affected less by it, cross-talk between bits is reduced significantly. Another advantage of antiferromagnets are their ultra-fast internal dynamics that can allow realization of devices operating in the terahertz regime. Their antiferromagnetic exchange coupling amplifies the spin-wave frequency which is known as "exchange amplification." It multiplies the anisotropy in the spin-wave dispersion relation which results in significantly faster spin dynamics. And finally, antiferromagnets are significantly more abundant in nature compared to ferromagnets. This gives a lot of options in terms of other properties of antiferromagnetic materials. They can

be metallic or insulating oxides. Their exchange interactions can much be more complex than a simple Heisenberg model - e.g. they can be non-collinear and chiral. Their magneto-elastic coupling can be strong. To summarize antiferromagnets might be challenging to study but they are still promising because they are very rich in spin-dependent phenomena.

So after half a century from Louis Néel's Nobel lecture, not only antiferromagnets are being used as passive elements for providing fixed layers in commercially available devices, they are at focus of a research effort to use them as active elements due to their many advantageous properties. A lot of interesting aspects of antiferromagnets has been discovered in the last decades and they are now one of the prime candidates for applications in the growing field of antiferromagnetic spintronics.

One is practical problem that antiferromagnets can potentially solve is called the "terahertz gap." In the field of communications engineering, most of the electromagnetic spectrum is sufficiently used for transmission of information depending on the circumstances of the application - except for a specific range of frequencies in the terahertz regime. This regime, also known as the terahertz gap, is a frequency range in the electromagnetic spectrum where practical and affordable technologies is seriously lacking for generating and detecting electromagnetic radiation, especially compared to other parts of the spectrum (see Fig. 1.2). It is roughly —and somewhat arbitrarily— defined wavelengths ranging from 30 μm to 3 mm which corresponds to frequencies from 100 GHz to 10 THz.

Currently, transmission or emission of electromagnetic waves with frequencies within this range are either inefficient or very costly. Although there are existing technologies operating in the terahertz frequencies including magnetrons, gyrotrons, synchrotrons and free electron lasers, due to their size and their cost, they usually only exist in university or government research labs or other dedicated facilities. Research that attempts to resolve this issue has been conducted since the late 20th century as these applications are also important to other fields such as astronomy, biology, chemistry and material science. With their characteristic frequencies in the THz regime,

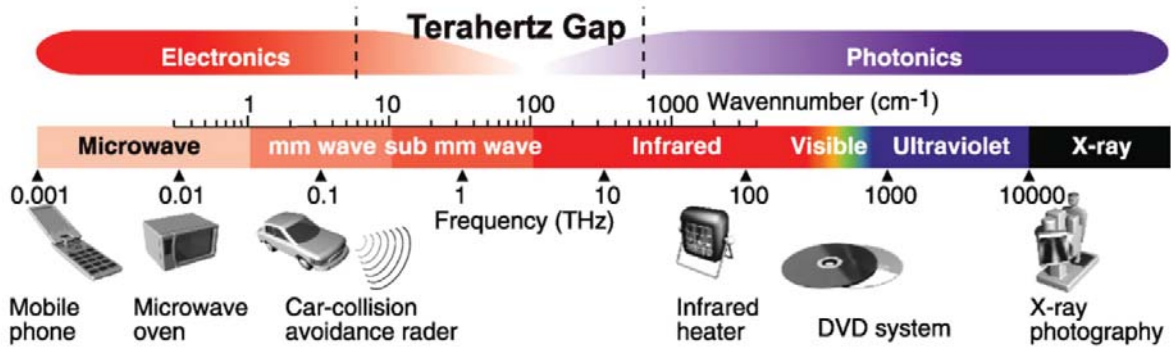


Figure 1.2: The electromagnetic spectrum and some example technologies that work on the specific wavelengths. The terahertz gap is between the highest frequencies of the radio spectrum and lowest frequencies of optical infrared detectors. The figure is adapted from [4].

antiferromagnets are prime candidates from bridging the terahertz gap. Oscillators, resonators, and narrow band detectors have been theoretically proposed and studied. And first experimental realizations are becoming slowly available, showcasing the application potential of antiferromagnetic materials.

1.3 ANTIFERROMAGNETISM

As it was mentioned before, antiferromagnetism is the type of magnetism where spins show long range order but arrange themselves in an antiparallel (or generally opposing) fashion so that net magnetization is canceled out.

The simplest way to describe the magnetic properties and behavior of antiferromagnets is to look at a general magnetic Hamiltonian consisting of multiple terms, each describing a specific interaction or energy.

$$H = H_{\text{Zeeman}} + H_{\text{Exchange}} + H_{\text{Anisotropy}} + H_{\text{DMI}} + \dots \quad (1.1)$$

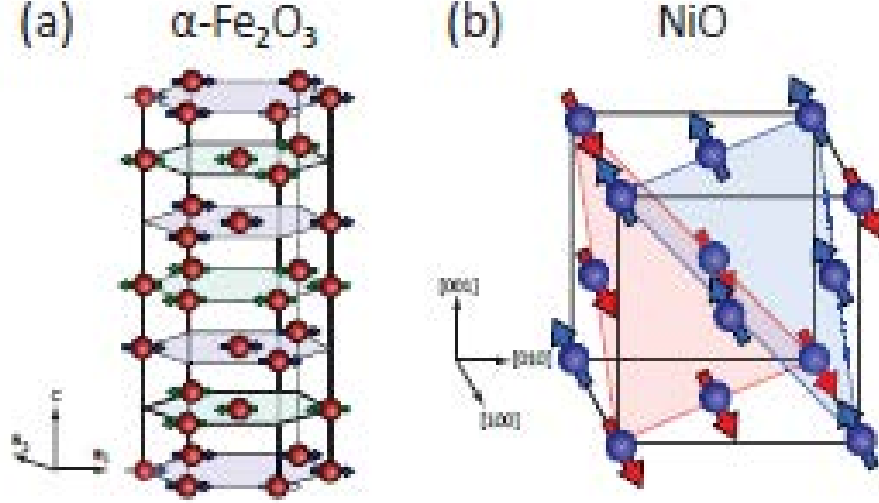


Figure 1.3: Crystal structures and spin arrangements of the antiferromagnets $\alpha\text{-Fe}_2\text{O}_3$ and NiO. (a) Hexagonal crystal structure of $\alpha\text{-Fe}_2\text{O}_3$ is shown with magnetic moments of Fe atoms coupled ferromagnetically inside the $[0001]$ planes and antiferromagnetically across them. (b) Cubic crystal structure of NiO with Ni moments coupled ferromagnetically inside $[111]$ easy planes and antiferromagnetically across them. Inside the $[111]$ easy-planes $[11\bar{2}]$ directions are the easy axes.

1.3.1 MAGNETIC ENERGIES

In this section, I will briefly introduce and discuss each type of magnetic interaction and their associated energy term, mentioned in equation 1.1: Zeeman, exchange, anisotropy and Dyazolinskii-Moriya interaction (DMI). These interactions will be relevant to understand and explain the behaviors of the antiferromagnetic materials which are relevant to the studies of this dissertation which are $\alpha\text{-Fe}_2\text{O}_3$ and NiO.

ZEEMAN INTERACTION

The most simple and common interaction between a magnet and a magnetic field is called the Zeeman interaction. It is responsible for aligning the magnetic moment and magnetic field colinearly. When a magnetic moment μ enters an external magnetic field H , a torque will be present on the magnetic moment. And it will depend on the relative orientation of the magnetic

moment and the external field. This torque is given by:

$$\boldsymbol{\tau} = -\mu_0 \boldsymbol{\mu} \times \boldsymbol{H} \quad (1.2)$$

As the cross product suggests, this torque will be maximum when $\boldsymbol{\mu}$ and \boldsymbol{H} are perpendicular and will be zero when they are along the same axis. The Zeeman interaction term in the spin Hamiltonian, describing this behavior is given by:

$$H_{\text{Zeeman}} = -\mu_0 \boldsymbol{\mu} \cdot \boldsymbol{H} \quad (1.3)$$

Overall this term favors parallel alignment between $\boldsymbol{\mu}$ and \boldsymbol{H} . In ferromagnetic materials, it is the dominant factor when it comes to determining the equilibrium direction of the magnetization. Whereas for antiferromagnetic materials, it is usually not the dominant term, as they have zero or a very small net magnetic moment.

EXCHANGE INTERACTION

The exchange interaction originates from the form of the wavefunction for identical particles in quantum mechanics. Unlike bosons, electrons are fermions with 1/2 spin and they cannot occupy the same quantum state. This also requires that their wavefunction must be antisymmetric under to exchange operation.

The exchange interaction is generally typically larger than other magnetic energies in most materials of interest, but it also decreases significantly as the distance between magnetic moments increases since the electron's orbits have exponentially less chance to overlap when they are sufficiently far away from each other. Therefore it is usually enough to limit the calculations to the nearest neighbors to get an accurate picture. In its simplest form it can be described by considering exchange energy term between neighboring spins which is called the Heisenberg model. This exchange energy is given by:

$$H_{\text{Exchange}} = J \sum_{(i,j)} \mathbf{S}_i \cdot \mathbf{S}_j \quad (1.4)$$

where \mathbf{S}_i and \mathbf{S}_j represents the spin operators of i^{th} and j^{th} spins, and J is the exchange coupling between spins. For $J > 0$, lowest energy state is achieved when spins are parallel, so the coupling is ferromagnetic. For $J < 0$, spins favor an antiparallel alignment, so the coupling is antiferromagnetic.

For antiferromagnetic materials exchange interaction is usually the strongest of all interactions. The effective field associated with exchange can be in the order of 1000s Tesla. Whereas the magnitude of an external field achievable in a conventional lab is in the order of 10 Tesla for materials that order at or above room temperature. This difference in scale is the main reason why external fields doesn't affect antiferromagnets that much. It is also the reason for faster dynamics as characteristic timescales are inversely proportional to strength of these energies.

MAGNETIC ANISOTROPIES

Magnetic anisotropy is a measure of how directional affects magnetic properties of a material. When the magnetization tends to lie along certain axes (or in certain planes), i.e. there are preferred directions, it is said that the material has magnetic anisotropy. In the Hamiltonian, it is described by the anisotropy term $H_{\text{anisotropy}}$ which is the energy penalty associated with rotating the magnetization vector into unpreferred directions. These preferred directions are called easy-axes and not surprisingly, the unpreferred directions are called the hard-axes. Magnetic anisotropy is defined as the energy it takes to rotate the magnetization from the easy axis to the hard axis. There are multiple sources of magnetic anisotropy. The main contributors usually are magneto-crystalline anisotropy, shape and surface anisotropy, magnetostriction anisotropy etc.

The most common type of magnetic anisotropy is the magneto-crystalline anisotropy which inherits the anisotropies of the underlying crystal structure. Since its origin is the crystal struc-

ture, it also has the same symmetries. This means it should be invariant under inversion of magnetization. And the mathematical function that describes it should be an even function of the angle between magnetization and the magnetic axes.

Depending on the lattice structure (cubic, tetragonal, hexagonal etc.) magnetic anisotropy can have multiple forms. But independent of the crystal structure, usually the first order anisotropy term dominates over higher order terms. And when the material has only an easy-axis, it is said that it has uniaxial anisotropy. In that case the anisotropy term can be written as:

$$H_{\text{anisotropy}} = -K_u(\hat{\mathbf{e}} \cdot \mathbf{m})^2 \quad (1.5)$$

where K_u is the anisotropy constant, \mathbf{m} is the magnetization and $\hat{\mathbf{e}}$ is the crystallographic direction. Given that $K_u > 0$, the anisotropy energy minimizes when magnetization \mathbf{m} is collinear to $\hat{\mathbf{e}}$ which is why it is the easy axis.

Sometimes instead of a preferred one, a crystallographic direction is specifically not preferred, meaning there exists an energy penalty. This is called the hard-axis anisotropy and it is in the form:

$$H_{\text{anisotropy}} = K_u(\hat{\mathbf{e}} \cdot \mathbf{m})^2 \quad (1.6)$$

where again K_u is the anisotropy constant, \mathbf{m} is the magnetization and $\hat{\mathbf{e}}$ is the crystallographic direction. In this case because there is no minus sign, the anisotropy energy minimizes when magnetization \mathbf{m} is perpendicular to $\hat{\mathbf{e}}$ which is the hard axis (again $K_u > 0$). Since this hard axis also defines an easy-plane, sometimes this anisotropy can be referred as easy-plane anisotropy too.

DZYALOSHINSKII-MORIYA INTERACTION

Another type of interaction that is present in magnetic materials is called Dzyaloshinskii Moriya interaction (DMI). It was independently discovered by Dzyaloshinskii and Moriya in the 1960s. It is a type of anti-symmetric exchange interaction and it can be derived by perturbative analysis of the spin-orbit coupling. Quantitatively, the term associated with DMI in the magnetic Hamiltonian is given by the following:

$$H_{DMI} = -D \sum_{(i,j)} \mathbf{S}_i \times \mathbf{S}_j \quad (1.7)$$

where \mathbf{S}_i and \mathbf{S}_j represents the spin operators of i^{th} and j^{th} spins, and D is the DMI vector characterizing the interaction between spins. As the cross-product suggests DMI favors perpendicular coupling between interacting spins. But due to the competition of other interactions, such as exchange, the angle between neighboring spins will not be 90° but some smaller angle, set by the relative amplitudes DMI and exchange.

Unlike exchange interaction, DMI is described by a vector, therefore it has a magnitude and a direction. The magnitude represents the strength of the interaction whereas the direction sets its chirality. Spins will gradually rotate clockwise or anticlockwise (left-handed or right-handed) depending on this chirality. Because of this, DMI is an absolutely crucial term for explaining chiral interactions and chiral spin textures such as skyrmions. It can also be a source of weak ferromagnetic behavior in an antiferromagnet, since it favors canting of magnetic moments instead of antiparallel coupling.

Mathematically speaking DMI originates because of lacking or breaking of certain inversion symmetries [5]. This symmetry breaking can either come from the crystal lattice itself or from interface of two adjacent layers of materials with different crystal structures which breaks the inversion symmetry by definition. Figure 1.4 shows a schematic of crystal and interfacial DMI. Specifically in antiferromagnetic α -Fe₂O₃, DMI is present and is responsible for slight canting of

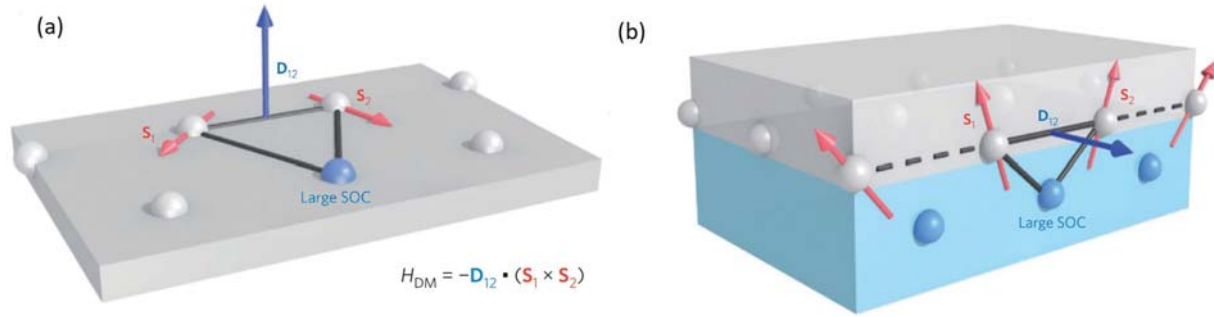


Figure 1.4: (a) Dzyaloshinskii–Moriya interaction generated by antisymmetric exchange of two atomic spins and an atom with a strong spin-orbit coupling. (b) Interfacial DMI generated at the interface of a magnetic and metallic layer. Figures are adapted from [6].

the moments. Therefore α -Fe₂O₃ has a small net magnetic moment even in antiferromagnetic phase. This net moment makes it easier for external fields to couple, essentially acting like a handle for rotating the magnetization and as a consequence the Néel vector as well.

We have looked at four different types of energy contributions to spin Hamiltonian: Zeeman, exchange, anisotropy and DMI. When modeling a specific magnetic material's response, it might be necessary to add more or remove some of these contributions depending on the specific problem we are trying to solve and its underlying assumptions.

All of these energy contributions can also be expressed in terms of effective magnetic fields. And summation of all these fields will determine the equilibrium configuration and domain distribution in the magnetic material, as the interactions compete among themselves. For example, exchange interactions can favor parallel or antiparallel spin alignment, magnetic anisotropy may prefer to lie along particular crystallographic axes or plane and DMI can favor canting of spins.

1.3.2 NÉEL VECTOR

When the sublattice moments of an antiferromagnet \mathbf{m}_A and \mathbf{m}_B are equal in magnitude but opposite in direction the net magnetization is zero, $\mathbf{m}_{\text{net}} = \mathbf{m}_A + \mathbf{m}_B = 0$. So unlike for ferromagnetic materials, magnetization is not a useful parameter to describe the state of antiferromagnets.

Material	Néel Temperature
NiO	525 K
α -Fe ₂ O ₃	950 K
FeF ₂	78 K
MnF ₂	68 K
CoO	290 K
CuMnAs	450 K

Table 1.1: Néel temperatures of some antiferromagnets.

That is why antiferromagnetism is usually described by the order parameter called the Néel vector \mathbf{n} . In collinear antiferromagnets, \mathbf{n} is defined as the difference between sublattice moments \mathbf{m}_A and \mathbf{m}_B :

$$\mathbf{n} = \frac{(\mathbf{m}_A - \mathbf{m}_B)}{2} \quad (1.8)$$

Above a critical temperature called the Néel temperature, the thermal energy is strong enough to overcome exchange interaction and destroy the antiparallel alignment. That is when the antiferromagnet becomes a paramagnet.

1.3.3 MAGNETIC SUSCEPTIBILITY

Magnetic susceptibility is measure of a material's magnetization response to an external magnetic field. The magnetization is usually proportional to the field and it is given by the following relation:

$$\chi = \frac{M}{H} \quad (1.9)$$

where \mathbf{M} is the magnetization and \mathbf{H} is the external field.

For *paramagnetic* materials, Curie law states that, at high temperatures and low magnetic fields, susceptibility is inversely proportional to temperature:

$$\chi = \frac{C}{T} \quad (1.10)$$

where C is the Curie constant.

In *ferromagnetic* materials, according to molecular field theory developed by Weiss, in addition to externally applied magnetic field there is a molecular field which is proportional to magnetization through the Weiss constant λ . And the susceptibility is given by the Curie-Weiss law:

$$\chi = \frac{C}{T - T_c} \quad (1.11)$$

where C again is the material's Curie constant and T_c is the critical temperature, i.e. the Curie temperature for ferromagnets. The important point is at the critical temperature, the ferromagnetic susceptibility diverges.

For *antiferromagnetic* materials, above the Néel temperature $T > T_N$, it is experimentally observed that the susceptibility obeys the following relation:

$$\chi = \frac{2C}{T + \theta} \quad (1.12)$$

Below the Néel temperature $T < T_N$, there are two solutions depending on the direction of measurement, χ_{\parallel} and χ_{\perp} . In a mean field approximation it can be calculated that:

$$\chi_{\perp} = \text{Constant} , \chi_{\parallel}(0) = 0 \quad (1.13)$$

Meaning that χ_{\perp} is independent of temperature and χ_{\parallel} has to reach zero at $T = 0K$. Also magnetic susceptibility of an antiferromagnetic material shows a maximum at the Néel temperature. And below the Néel temperature, depending on the measurement direction, there are two solutions. Fig 1.5 summarizes how antiferromagnetic susceptibility (c) compares to paramagnetic

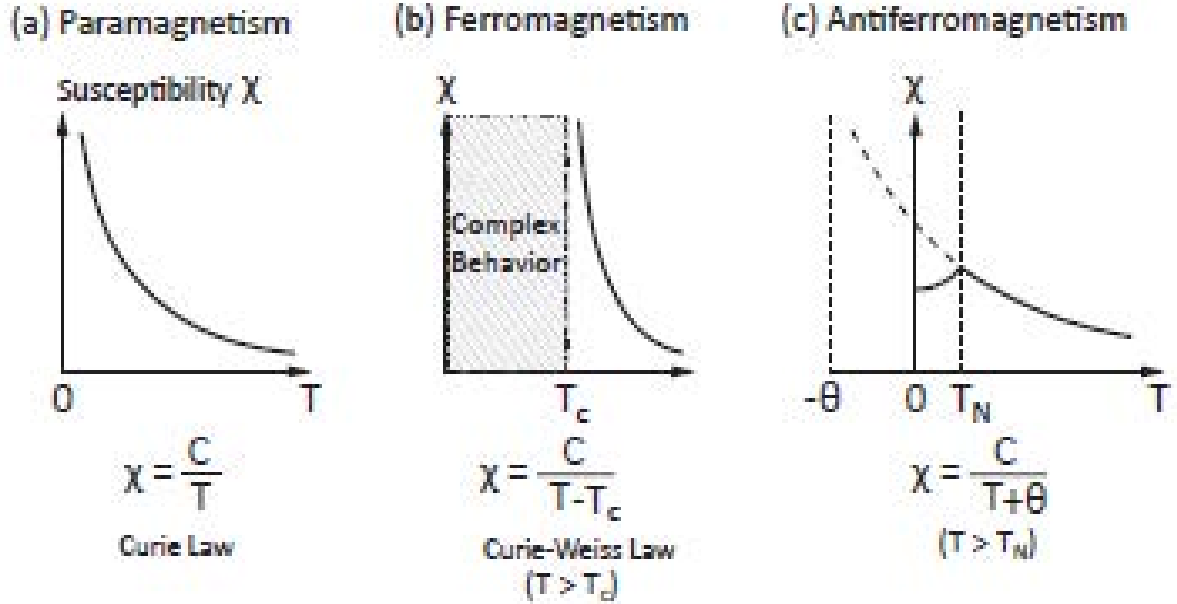


Figure 1.5: Comparison of magnetic susceptibilities of (a) paramagnets, (b) ferromagnets and (c) antiferromagnets. For antiferromagnets, below the Néel temperature, T_N , there are two different magnetic susceptibilities: χ_{\parallel} and χ_{\perp} . These are susceptibilities parallel and perpendicular to easy axes respectively. The figure is adapted from [7].

(a) and ferromagnetic susceptibility.

Overall antiferromagnets have zero net magnetic moment and they have very strong internal exchange fields. The effective field associated with the exchange interaction between the sublattice moments is typically in the order of 1000 Tesla for antiferromagnets that order at room temperature and above, which is at least 2 orders of magnitude larger than the magnetic fields achievable in the lab. The combination of these two properties makes antiferromagnets impervious to external magnetic fields. In fact, values of their magnetic susceptibility are orders of magnitude smaller than ferromagnets. This is the main reason why it seemed like antiferromagnets do not seem to have any applications initially, because of how unresponsive they are to external effects.

1.4 DETECTING ANTIFERROMAGNETS

The traditional methods of deducing the state of magnetic materials are always not very effective on antiferromagnets because of their vanishing moments. Even if it is a challenging task, new experimental methods are getting developed every year to detect antiferromagnetic Néel vector in different materials.

Some of these methods include: thermal imaging leveraging the spin Seebeck effect and anomalous Nernst effect [8, 9], imaging uncompensated surface moments using nitrogen–vacancy defects in diamonds [10], second harmonic generation imaging [11], imaging using the optical bi-refrindex effect [12] and using the exchange bias effect in heterostructures [13, 14].

But in the context of this dissertation we will mainly focus on two methods. First one is electrical detection of Néel order via spin Hall magneto-resistance, a relatively easy but an indirect method. And the second one is using x-rays and linear dichroism effect, direct but a more challenging method to implement. In the next section, I will introduce and discuss both of the methods that we used to detect Néel order, as well as concepts that are required to understand those methods.

1.4.1 SPIN HALL EFFECT AND INVERSE SPIN HALL EFFECT

When charge carriers move through a conductor, it defines a charge current. Generally, this charge current consists of equal number of electrons with spins up and down. But it is possible to break this balance and create a net angular momentum flow. When this happens it defines a spin current in the direction of flow of angular momentum. Interestingly a net charge current is not necessary to create a spin current. Two opposing but equal in magnitude spin up and spin down currents can produce a spin current with net zero charge flow. This is a specifically interesting case as pure spin currents do not suffer from dissipation in the form of Joule heating.

The generation, manipulation, and detection of spin currents is one of the key aspects of the

field of spintronics as they are commonly used to effect magnetic layers in the form of spin-orbit and spin-transfer torques. And spin Hall Effect (SHE) and inverse spin Hall Effect (ISHE) are two of the most common used effects for the generation and detection purposes, especially for insulating magnetic layers.

In ordinary the Hall effect, charge carriers with opposite signs deviate in different directions under the effect of external magnetic field due to the Lorentz force. In spin Hall effect, there is no need for an external field. If the metal has a strong spin-orbit coupling, opposite spins deviate such that there will be spin accumulation on lateral surfaces. The total spin current is given by the following equation:

$$\mathbf{j}_s = \theta_{SH}(\boldsymbol{\sigma} \times \mathbf{j}_c) \quad (1.14)$$

where j_c is the charge current, σ is the spin polarization direction and θ_{SH} is the spin Hall angle which is a measure of conversion ratio between spin and charge currents. Although there are wide range of reported values depending on the measurement technique, for most metals the spin Hall angle θ_{SH} hovers around couple of percent. Most importantly for platinum it is around 0.02 [15] and Pt is widely used metals for spin injection/detection purposes. And notably W is the another metal which is used because of its negative and large spin Hall angle around -0.3 [16]. Note that it is also not unphysical to have spin Hall angle larger than 1, as it doesn't break any conservation law (e.g. charge or angular momentum).

The spin Hall effect is mostly used as a spin injection and detection technique in heterostructures, where an adjacent metallic layer with a large spin-Hall angle can create an spin accumulation at the interface of insulating magnetic layer. It was first theoretically described by Dyakonov and Perel in 1971 [17], named the spin Hall effect by Hirsch *et al.* in 1999 [18] and experimentally observed by Kato *et al.* in 2004 [19]. Microscopically, the spin Hall effect can originate from multiple sources. Generally they are separated in two categories: intrinsic and extrinsic. If the

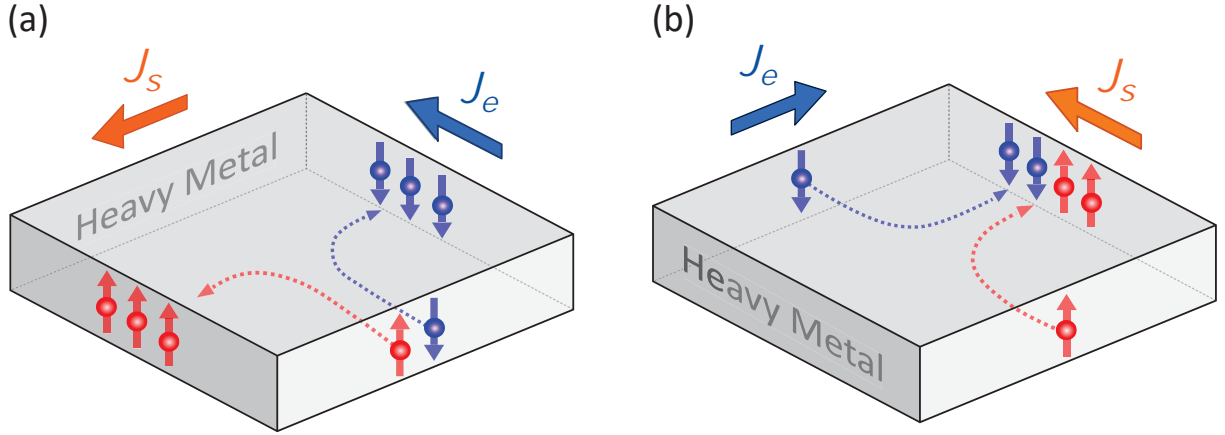


Figure 1.6: Schematic representation of different types of (a) spin Hall effect and (b) inverse spin Hall effect. Through these mechanisms spin currents and electrical currents inside a metal wire, can be converted to one another.

origin is the band structure of the metal, it is referred as an intrinsic effect. And if the origin is related to scattering of electrons due to impurities it is referred as an extrinsic effect.

Intrinsically, the spin Hall effect originates from the coupling of the charge and spin currents due to spin-orbit coupling. Spin-orbit coupling (SOC), is a relativistic interaction between electron's intrinsic spin \mathbf{s} and its orbital angular momentum \mathbf{l} . This coupling can modulate the band structure of the metal and in turn flowing electrons can pick a transverse velocity. The spin Hall conductivity is proportional to expected value of this coupling at the Fermi surface and given by the following relation [15]:

$$\sigma_{xy}^{s_z} \approx \frac{e}{4a} \frac{\langle \mathbf{l} \cdot \mathbf{s} \rangle_{FS}}{\hbar^2}, \quad (1.15)$$

where e is the unit charge and a is the lattice constant.

Extrinsic effects are where electrons undergo spin dependent scattering in a way that spin-up and spin-down electrons pick up opposite transverse velocities. Spin skew scattering and side-jump scattering are two of these effects. Although both are associated with electron scattering from impurities they are slightly different mechanisms. In spin-skew scattering, momentum of

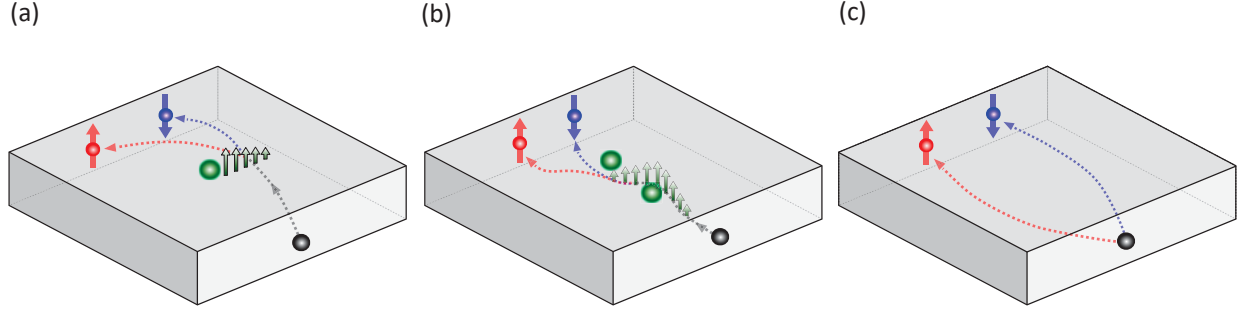


Figure 1.7: Illustrations of mechanisms that give rise to the spin Hall Effect. Red and blue electrons are spin-up and spin down electrons. Green spheres are the scattering locations. And the green arrows represent the magnetic fields. (a) Extrinsic spin skew scattering, (b) extrinsic side-jump scattering, (c) intrinsic SHE coming from the band structure of the metal. Figure is adapted from [15].

the electron after scattering becomes spin-dependent. Depending on the direction of the spin, this field gradient results in a net force toward or away from the scattering center. In side-jump scattering describes a spin-dependent displacement during each scattering jump occurs due to the spin dependent different acceleration and deceleration during the scattering, which results in an effective transverse displacement of the electron upon repeated scattering.

The reciprocal effect of the spin Hall effect is called the inverse spin Hall effect where a net spin current creates a transverse charge current. The total charge current is given by the following relation:

$$\mathbf{j}_c = D_{ISHE}(\boldsymbol{\sigma} \times \mathbf{j}_s) \quad (1.16)$$

where D_{ISHE} is the inverse spin Hall coefficient.

1.4.2 SPIN HALL MAGNETORESISTANCE

The resistivity of heterostructures consisting of insulating magnetic and metallic non-magnetic layers depends on the angle between electric current direction and magnetization. This phenomenon is first seen in metallic ferromagnets and known as anisotropic magnetoresistance (AMR). But the symmetries of the magnetoresistance signal seen in the heterostructures is differ-

ent than what found in bulk ferromagnets. Specifically, instead of depending the angle between the magnetization and the current $\sim (\mathbf{m} \cdot \mathbf{j})$, it depends on the the angle between magnetization and the direction perpendicular to the current $\sim [\mathbf{m} \cdot (\mathbf{j} \times \hat{z})]$, indicating spin accumulation at the interface as a possible origin because it is always perpendicular to the current direction.

Spin Hall Magnetoresistance (SMR) first observed in heterostructures consisting of ferrimagnetic insulator $\text{Y}_2\text{Fe}_5\text{O}_{12}$ (YIG) and heavy metal Pt [20]. It was theoretically explained as a non-equilibrium proximity effect caused by the spin accumulation at the interface. Because it is symmetric under magnetization reversal, it is expected to be seen in antiferromagnetic layers as well. In fact, later it was first observed in several AFM/HM bilayers one of the first being NiO [21]. And since then it turned out to be a very valuable technique for providing information on the orientation of the Néel vector as it is relatively easy to measure in the lab.

The longitudinal resistance of the metallic layer in an AFM/HM heterostructure, is given by the following equation:

$$R_{\text{long}} = R_0 + \frac{\Delta R}{2}(1 + \cos 2\phi), \quad (1.17)$$

where ϕ is the angle between magnetization and current direction, and ΔR is the magnitude of the spin Hall magnetoresistance.

The SMR can be understood in terms of conversion of charge currents to spin currents and vice versa at the interface, because of the spin Hall effect (SHE) and inverse spin Hall effect (ISHE) happening at the metallic layer. Consider an insulating magnetic layer / heavy metal bilayer heterostructure (Fig. 1.8), where electric current J_c is passing through the heavy metal. Due to the SHE, there will be a spin current J_s perpendicular to the interface with a spin polarization σ . Some portion of this spin current will be absorbed as spin torques J_s^{ST} and some portion will be reflected at the interface as J_s^{back} . The relative ratio of the reflected and absorbed portions will depend on the magnetization or the adjacent layer - \mathbf{m} for ferromagnets and \mathbf{n} for antiferromagnets. Finally

the reflected spin current J_s^{back} will be converted again back to a charge current via the ISHE, which will contribute the longitudinal resistance, the resistance in the direction of the charge current flow.

Figure 1.8, shows the large and small resistance states for ferromagnetic and antiferromagnetic case. In both cases the maximum resistance is associated with minimum spin back flow and minimum resistance is associated with maximum spin back flow. The main difference is caused by the 90 °difference between couplings of Néel vector \mathbf{n} and magnetization \mathbf{m} to the external magnetic field.

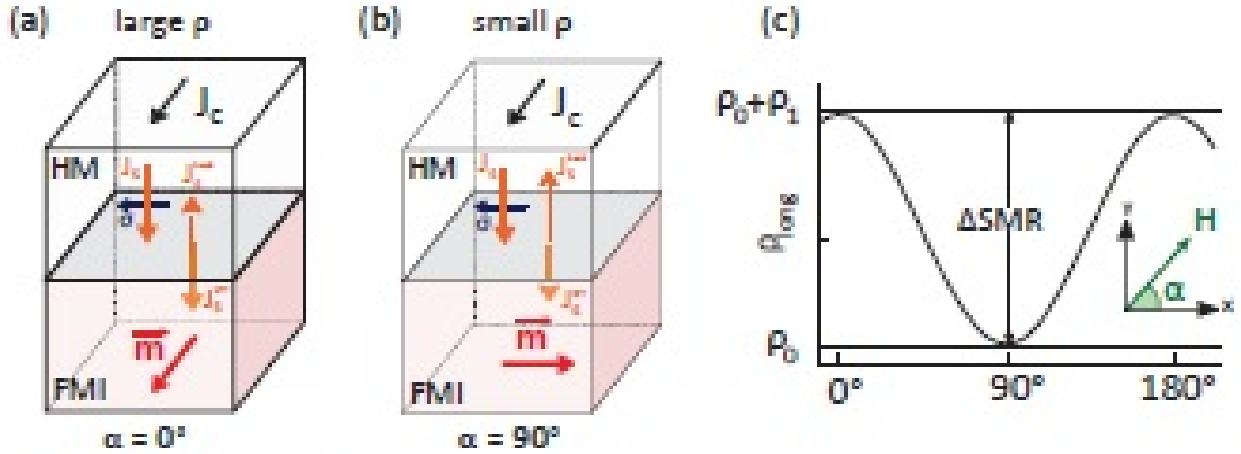
1.4.3 HARMONIC MEASUREMENTS

Harmonics are defined as frequencies that are integer multiples of the fundamental source frequency. In the context of electronics, it corresponds to sending a current with frequency ω and measuring the responses at ω , 2ω , 3ω etc.. These are known as the first, second, third harmonic and so on. Harmonic measurements is a technique to measure these higher order responses and when it is used in combination of a known effect like SMR, they can probe important characteristics of a system. In the context of this thesis, I will focus on harmonic Hall measurements on AFM/HM heterostructures. And harmonic measurements are especially useful, because they can quantify the of spin torques present in these heterostructures.

Consider an AC current density in the metallic layer with frequency ω : $I_c(t) = I_0 \cos \omega t$. This current will create an oscillating spin accumulation at the interface, which in turn apply a spin-orbit-torque on the Néel vector. Therefore the Hall resistance $R_H(t)$ of the metallic layer will also be a function of time, as it will be affected by spin-Hall magnetoresistance.

The Hall voltage of the metallic layer is given by Ohm's law $V_H(t) = R_H(t)I_c(t)$ and this voltage can be expanded into second order:

FMI/HM Bilayer



AFI/HM Bilayer

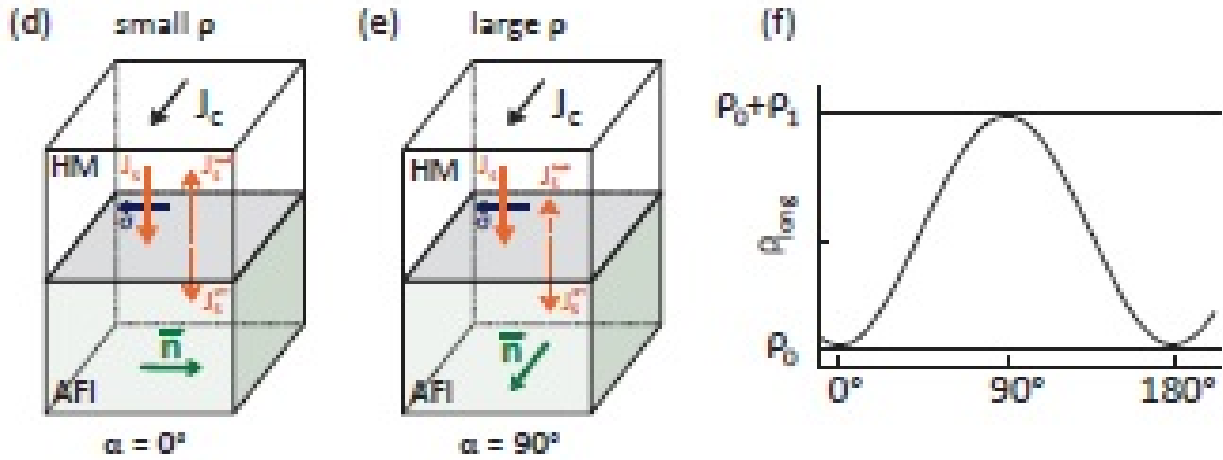


Figure 1.8: Comparison of ferromagnetic (top row) and antiferromagnetic (bottom row) spin Hall magnetoresistance (SMR). The magnitude of SMR is based on conversion of charge currents J_c and spin currents J_s . In both ferromagnetic insulator (FMI) and antiferromagnetic insulator (AFI) cases, the resistance of the heterostructure is large when the spin current back flow is small J_s^{back} (a,e). And the resistance is small when J_s^{back} is large (b,d). The main difference is caused by difference in coupling of FMI and AFI to the external field. FMI couples in a parallel fashion whereas AFI couples perpendicularly. This causes a 90° shift on angular dependence of SMR between FMI and AFI. Figure is adapted from [22].

$$\begin{aligned}
V_H(t) &= R_H(0)I_0 \cos \omega t + \frac{1}{2} \frac{\partial R_H(0)}{\partial I_0} I_0^2 (1 + \cos 2\omega t) \\
&= V_0 + V_{1\omega} \cos \omega t + V_{2\omega} \cos 2\omega t
\end{aligned} \tag{1.18}$$

where V_0 is the DC voltage, $V_{1\omega}$ and $V_{2\omega}$ are the first and second harmonic voltage responses. They can be directly be measured by a lock-in amplifier.

1.4.4 X-RAY MAGNETIC DICHOISM

When electromagnetic radiation in the form of X-rays hits a material, electrons inside that material will be excited to higher energy states, leaving core holes behind. Another electron from higher energy will fill the core hole, while releasing energy. This energy can be released in the form of an emitted photon but also can be transferred to a secondary electron, causing it to be emitted. This process is known as Auger-Meitner effect [23, 24]. These electrons then can be collected to form an image of the surface of that material. In general, emission of electrons induced by electromagnetic radiation is known as photoelectric effect. And the microscopy technique that uses this effect are known as photo-emission electron microscopy (PEEM).

The contrast of a PEEM image can originate from different sources depending on the sample characteristics, the wavelength and polarization of the light. Topology, surface chemistry, charge anisotropy or magnetic order can be among these sources. Naturally, in the context of this dissertation we will be focusing on the magnetic origins.

When the magnetic order is the origin of contrast, the type of polarization of light becomes important. Depending on the polarization being circular (left or right) or linear (horizontal or vertical), x-rays become sensitive to different types of magnetic order. Specifically, circular polarization is sensitive to ferromagnetism, where as linear polarization is sensitive to antiferromagnetism.

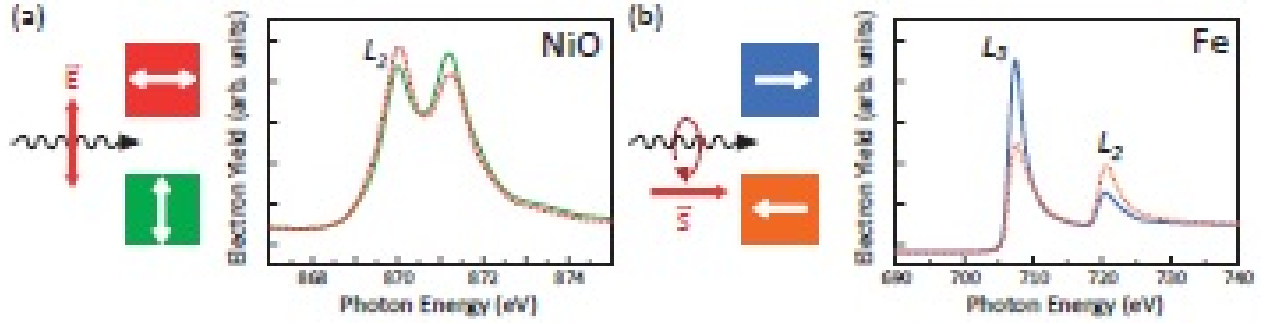


Figure 1.9: (a) Demonstration of XMLD effect on NiO absorption spectrum. Linearly polarized light yields different amounts of photoelectrons at Ni L_2 edge energies, depending on the underlying domain structure. (b) Demonstration of XMCD effect on Fe absorption spectrum. Circularly polarized light yields different amounts of photoelectrons at Fe L_2 and L_3 edge energies, depending on the underlying domain structure. The figure is adapted from [25].

X-ray magnetic circular dichroism (XMCD) effect, first observed by Schütz *et al.* [26] in 1987, is difference of absorption of left and right circularly polarized x-rays at specific energies — corresponding to transition of electrons between orbitals. This observed difference of absorption is proportional to the difference of the spin densities which means that XMCD can probe the difference between spin-up and spin-down empty states inside the material. For a ferromagnetic material, there is a large difference between the occupation of the spin-up and spin-down states. Therefore XMCD is an excellent probe of ferromagnetism in thin films.

Similarly, X-ray magnetic linear dichroism, is the difference of absorption of linearly polarized x-rays depending on the polarization direction. In general, linear dichroism effect measures the small charge anisotropies in the crystal. In an antiferromagnetic material, the alignment of the local spins along the magnetization axis breaks the symmetry of the crystal through spin-orbit coupling. As a result, the charge distribution becomes slightly anisotropic in the direction of Néel vector. And this charge anisotropy leads to an asymmetry of the x-ray absorption signal, where maximum XMLD difference is obtained when x-ray polarization is parallel versus perpendicular to the Néel vector. XMLD is a very useful probe of antiferromagnetism in thin films, as they cannot be studied by many other techniques because of their compensated magnetic moments

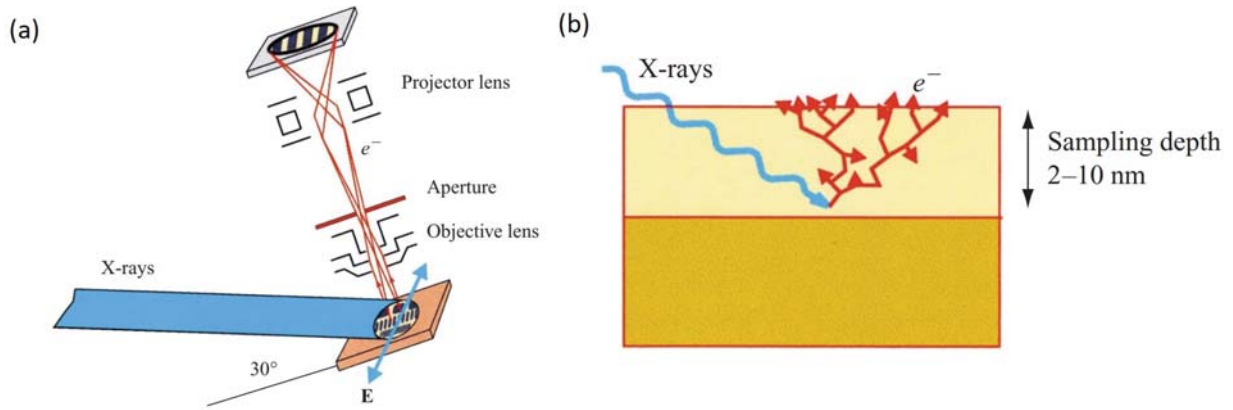


Figure 1.10: (a) Schematic of the experimental geometry of photoemission electron microscopy. (b) Illustration of generation and scattering of secondary electron which mostly probe the top 2-10 nanometers of the sample surface. The figure is adapted from [25].

and because larger samples are generally needed for neutron scattering experiments.

The most important caveat is, since XMLD measures charge anisotropies in the crystal, there can be non-magnetic contributions to linear dichroism. Magnetostriction, substrate effects, and the lattice structure itself can be the source of contributions. Therefore it is crucial to image an antiferromagnetic material below and above its Néel temperature T_N before concluding the origin of linear dichroism is magnetic. If it is coming from antiferromagnetic order, it should disappear above the Néel temperature when the antiferromagnet becomes a paramagnet.

The power of PEEM comes from its chemical specificity combined with high spatial resolution. The energy of X-rays can be tuned to the desired element's absorption peak, imaging the contrast coming only from one type of magnetic moment with around 50 nm spatial resolution. Then a different energy can be chosen, to image another element's moment from another layer in the same sample. But it is important to keep in mind that PEEM is a surface sensitive technique. Most of the contrast generated is coming from the top 5 nanometers of the sample. Although soft X-rays can penetrate deeper into the material, most emitted electron originate from top most layers, therefore it is essential to use a capping layer no thicker than 1 or 2 nanometers.

1.5 CONTROLLING ANTIFERROMAGNETS

Similar to detecting it, controlling the antiferromagnetic order is also challenging. Of course this makes sense considering their small magnetic susceptibility. Nevertheless there are methods to manipulate them and in the next section I will discuss some these, particularly the ones most relevant to the studies in the next chapters.

1.5.1 EXTERNAL FIELD

Even though their susceptibility is small, that doesn't mean that it is impossible to influence antiferromagnets with magnetic fields. In fact, antiferromagnets can be rotated in a quasistatic manner when the field is strong enough. Sometimes these fields can be really high, some times they can be modest. For uniaxial antiferromagnets, it is useful to look at what happens when an external magnetic field is applied along or perpendicular to easy axis separately.

When the field is perpendicular to the easy axis, the magnetic moments on the two sublattices cant towards the field direction and a net magnetization M gradually builds up proportional to the field. The net magnetization reaches an equilibrium when the Zeeman energy that is gained from developing a net moment approximately equals the exchange energy lost from slight deviation from antiparallel alignment.

When the field is parallel to the easy axis, the sublattice magnetization remains parallel easy axis state until the external magnetic field completely compensates the anisotropy energy. At the compensation point the sublattice magnetization is then free to rotate in directions perpendicular to the easy axis without any energy penalty. This is known as the spin flop transition and is approximately occurs at the following applied magnetic field:

$$\mu_0 H_{sf} \approx \sqrt{2H_{ani}H_{ex}}, \quad (1.19)$$

where H_{ani} and H_{ex} are effective fields associated with easy axis anisotropy and exchange interaction.

If the magnetic anisotropy is very strong, high enough external fields can destroy the antiparallel alignment without flopping the Néel vector and make the sublattice moments parallel to each other along the easy axis. This is known as the spin-flip transition and it usually occurs in very high fields. It is not relevant for the studies in this dissertation.

In antiferromagnets with an easy-plane anisotropy, like α -Fe₂O₃, rotating the Néel vector within the easy plane is relatively straightforward with an external magnetic field. A field that is applied in the easy plane will couple to the Néel vector perpendicularly, as the sublattice moments cant and develop a net moment. The existence of DMI helps this even further as DMI also favors of canting of sublattice moments. For α -Fe₂O₃ a modest field of 1 Tesla is enough to saturate the magnetization and rotate the Néel vector adiabatically within the easy plane.

1.5.2 SPIN-ORBIT TORQUES

Spin-orbit torques are transfer of angular momentum between spin angular momentum of charge carriers and spin angular momentum of the localized electrons associated with spin-orbit coupling in a conductor. There are two mechanisms that are known to produce these torques: inverse spin galvanic and spin Hall effect rising from heavy metals in heterostructures. Inverse spin galvanic effect can originate from bulk or interfacial effects in systems lacking inversion symmetry, whereas the spin Hall effect originates in heavy metals with large spin-orbit coupling. Regardless of the origin, inverse spin galvanic or spin-Hall effects, spin-orbit torques have the form:

$$\boldsymbol{\tau} = \tau_{\parallel} \mathbf{m} \times ((\hat{\mathbf{e}} \times \mathbf{j}_c) \times \mathbf{m}) + \tau_{\perp} \mathbf{m} \times (\hat{\mathbf{e}} \times \mathbf{j}_c), \quad (1.20)$$

where $\hat{\mathbf{e}}$ is a unit vector direction determined by symmetries of the system under investigation.

When the origin of the torques are spin Hall effects, $\hat{e} \times \mathbf{j}_c$ can be replaced with spin accumulation σ .

The torque is decomposed into two perpendicular components according to their relative orientation with respect to \mathbf{m} and σ : τ_{\parallel} and τ_{\perp} . Similar to the naming of spin-transfer torques [27], they are also referred as damping-like torques τ_{DL} and field-like torques τ_{FL} respectively, because of their symmetries similar to torques originating from an effective field and Gilbert damping.

In the context of antiferromagnets, damping-like torques have a unique property. Unlike external fields, they act on each sublattice in a way that their combined effects is not cancelled out. This can be better understood, in terms of effective fields $H_{\text{eff}} = \mathbf{m} \times \boldsymbol{\sigma}$, which are different for each sublattice moment. Experimentally, emerging from bulk inversion asymmetry, inverse spin galvanic effect in CuMnAs, has been proposed as a mechanism to reorient the Néel vector. Similarly spin-orbit torques have been proposed as switching mechanism in PtMn/Pt metallic heterostructures [28] and α -Fe₂O₃/Pt [29] insulating AFM/HM heterostructures. In both cases, antiferromagnetic Néel vector reorients itself perpendicular to the charge current flow. Therefore two perpendicular current paths are needed to switch the AFM from one state to another. And the switching is independent of current polarity as expected from the symmetry of uniaxial antiferromagnets.

1.5.3 MAGNETO-ELASTIC EFFECTS

Magneto-elastic effects describe coupling of material's magnetic properties and its mechanical deformation (i.e strain). The best known of these effects is Joule magnetostriction, where a magnetic material changes its dimension in the direction of an applied magnetic field. The inverse of Joule magnetostriction is known as the Villari effect where an applied stress causes change of magnetization [30]. These stresses can introduce additional anisotropies to the spin Hamiltonian, characterized by the material dependent magnetostrictive coefficient λ .

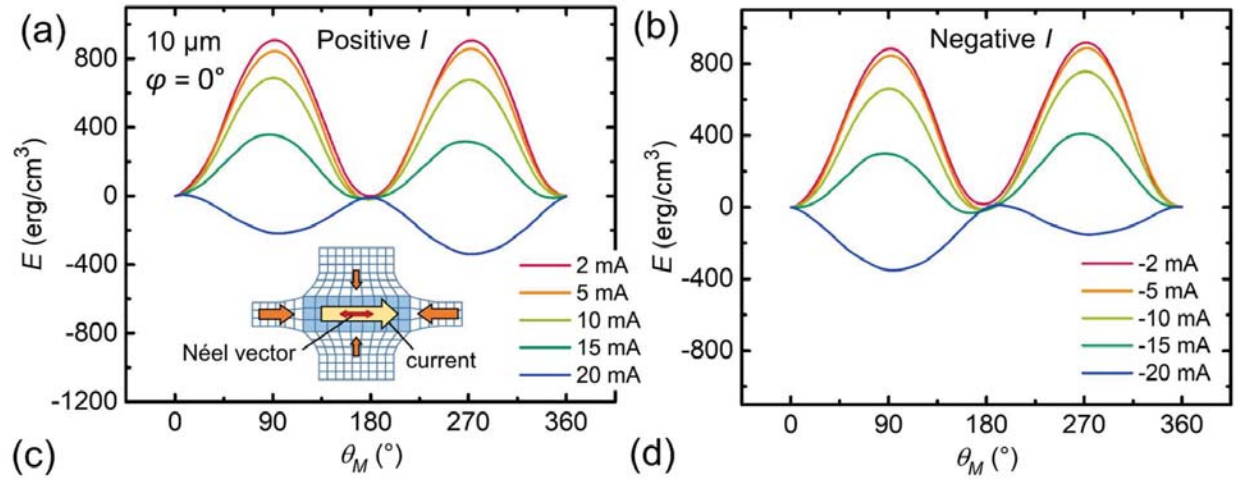


Figure 1.11: Magneto-elastic energy in $\alpha\text{-Fe}_2\text{O}_3/\text{Pt}$ Hall bars with $10 \mu\text{m}$ channel width as a function of angle of external magnetic field at different magnitudes of (a) positive and (b) negative currents. Inset in (a) shows magnetostriction effect induced by compressive stresses associated with Joule heating in a Hall-bar. Figure is taken from [31].

In the context of antiferromagnetic spintronics, applied stress can come from Joule heating associated with high density current pulses in switching experiments. Generally, current channels used in these experiment are in micron scale in length and width, and nanometer scale in thickness. Therefore, the temperature gradient across the sample caused by Joule heating can be significant and can induce compressive or tensile stress along the current channel. And in materials with high magnetostrictive coefficients it can contribute to switching of magnetization.

In fact, it has been proposed as a dominant or additional mechanism of switching in many experiments as it has the same symmetries of spin-orbit torques.

1.6 DYNAMICS OF ANTIFERROMAGNETS

Dynamics of bipartite collinear antiferromagnets are phenomenologically best described by considering two ferromagnetic spins coupled to each other by the exchange interaction. Therefore it makes sense to start by working out the equations of motion for a single ferromagnetic

moment and then later expand it to antiferromagnetic system.

When a magnetic moment is exposed to an external magnetic field, a torque will be present. This torque τ was given by the following equation:

$$\tau = \mathbf{m} \times \mu_0 \mathbf{H}_{\text{eff}} \quad (1.21)$$

where \mathbf{m} is the magnetic moment, μ_0 is the magnetic permeability of free space and \mathbf{H}_{eff} is the effective field that encapsulates all the combination of external and internal fields:

$$\mathbf{H}_{\text{eff}} = \mathbf{H}_{\text{external}} + \mathbf{H}_{\text{exchange}} + \mathbf{H}_{\text{ani}} + \mathbf{H}_{\text{DMI}} + \dots, \quad (1.22)$$

where $\mathbf{H}_{\text{external}}$ is the applied magnetic field, $\mathbf{H}_{\text{exchange}}$ is the exchange field,

The associated angular momentum with this moment is given by the gyromagnetic ratio (γ) relation:

$$\mathbf{m} = \gamma \mathbf{L}, \quad (1.23)$$

where $\gamma = g\mu_B/\hbar$, g is the Landé g -factor, μ_B is the Bohr magnetron and \hbar is the reduced Plank constant. Newton's second law says the torque on a system equals to change in its angular momentum:

$$\tau = \frac{d\mathbf{L}}{dt} = \mathbf{m} \times \mu_0 \mathbf{H}_{\text{eff}}, \quad (1.24)$$

And if we use the gyromagnetic ratio relation to substitute angular momentum \mathbf{L} , equation 1.24 can be rewritten as:

$$\frac{d\mathbf{m}}{dt} = \gamma \mu_0 (\mathbf{m} \times \mathbf{H}_{\text{eff}}), \quad (1.25)$$

This equation is known as Landau-Lifshitz equation and describes the uniform precession

of a magnetic moment around the applied field with the Larmor frequency $\omega = \gamma\mu_0 H$. This is analogous of precession of a spinning top inside a uniform gravitational field without any frictional loss.

1.6.1 LANDAU-LIFSHITZ-GILBERT EQUATION

In reality, every physical system loses energy over time due to dissipational forces. To capture this Landau and Lifshitz proposed a damping term proportional to $\mathbf{m} \times (\mathbf{m} \times \mathbf{H}_{\text{eff}})$, which is always perpendicular to the orbit, so that precession slowly dies out. Later, Gilbert modified the damping term into $\alpha \mathbf{m} \times \frac{d\mathbf{m}}{dt}$ and the resulting equation is now known as Landau-Lifshitz-Gilbert (LLG) equation:

$$\frac{d\mathbf{m}}{dt} = \gamma\mu_0(\mathbf{m} \times \mathbf{H}_{\text{eff}}) + \alpha(\mathbf{m} \times \frac{d\mathbf{m}}{dt}), \quad (1.26)$$

where α is the dimensionless Gilbert damping parameter. It is a phenomenological constant that encompasses multiple methods of dissipation of angular momentum from spin precession to the lattice. The methods include dissipation via spin-orbit coupling, scattering processes and non-local spin relaxation processes.

An interesting aspect of the Gilbert damping term is that it is proportional to the change of magnetization $\frac{d\mathbf{m}}{dt}$, meaning an increase in the rotation rate of magnetization increases the damping of the system.

1.6.2 SPIN TORQUES

In 1996, Slonczewski and Berger independently realized that the effects of Gilbert damping can be countered by spin-transfer torques [32, 33] and lead to magnetization switching or stable oscillations in spin valves. They expanded LLG the model to account for the spin-transfer torque term. This equation is now known as Landau-Liftshitz-Gilbert-Slonczewski (LLGS) equation:

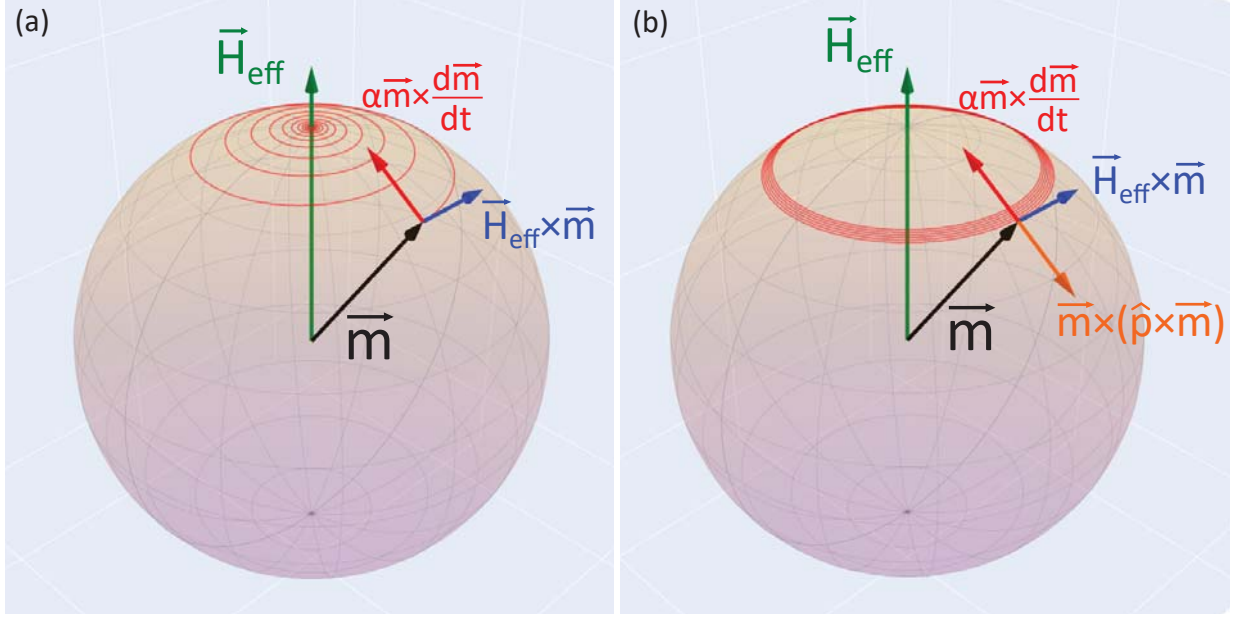


Figure 1.12: (a) Precession of magnetization around an effective magnetic field H_{eff} , according to the LLG equation. Blue arrow represents the torque associated with H_{eff} which drives the precession. Red arrow represents the Gilbert damping torque, which makes the magnetization settle decay into equilibrium. (b) Spin torque, τ_{ST} , in the form of anti-damping, $\vec{m} \times (\hat{p} \times \vec{m})$, counteracts the effect of damping and keeps the precession going.

$$\frac{d\vec{m}}{dt} = \gamma \vec{H}_{\text{eff}} \times \vec{m} + \alpha \vec{m} \times \frac{d\vec{m}}{dt} + \tau_{ST}, \quad (1.27)$$

where H_{eff} is the effective magnetic field, γ is the gyromagnetic ratio, α is the Gilbert damping constant and τ_{ST} is the spin torque. Again this torque can be decomposed into field-like and damping-like components:

$$\vec{\tau} = \tau_{\text{DL}} \vec{m} \times (\hat{p} \times \vec{m}) + \tau_{\text{FL}} \vec{m} \times \hat{p} \quad (1.28)$$

where \hat{p} is the polarization vector usually set by the symmetry of the system, τ_{DL} and τ_{FL} are field-like and damping-like torques respectively. It is again beneficial to decompose the torques like this because damping-like torques τ_{DL} and field-like torques τ_{FL} affect the magnetization in

fundamentally different ways. Damping-like torques change the energy of the system and can switch the magnetization, whereas field-like torques act like an effective field and only change the precession frequency.

For the antiferromagnetic case equation 1.27 become two coupled equation one for each sub-lattice:

$$\begin{aligned}\frac{d\mathbf{m}_1}{dt} &= \gamma \mathbf{H}_1^{\text{eff}} \times \mathbf{m}_1 + \alpha \mathbf{m}_1 \times \frac{d\mathbf{m}_1}{dt} + \tau_1^{FL} + \tau_1^{DL} \\ \frac{d\mathbf{m}_2}{dt} &= \gamma \mathbf{H}_2^{\text{eff}} \times \mathbf{m}_2 + \alpha \mathbf{m}_2 \times \frac{d\mathbf{m}_2}{dt} + \tau_2^{FL} + \tau_2^{DL}\end{aligned}\tag{1.29}$$

where the coupling is associated the exchange interaction is included in the effective field term, $\mathbf{H}_{1,2}^{\text{eff}}$.

1.7 STATE OF THE ART AND OVERVIEW OF DISSERTATION

In this section, first I will talk about the recent developments in the field of antiferromagnetic spintronics by highlighting some key theoretical and experimental research papers, then I will give an overview of my dissertation within the context of these research paper.

1.7.1 ANTIFERROMAGNETIC OSCILLATOR

For a magnetic system to sustain steady-state oscillations, it needs to have a feedback mechanism, so that driving force and the feedback can balance each other at a unique state. For Spin Hall nano-oscillators (SHNO) made from ferromagnetic materials Gilbert damping and spin-torques can balance each other at a unique precession angle, allowing sustained oscillations with the frequencies in the megahertz to gigahertz regime.

In their 2016 article in Physical Review Letters [34], Cheng *et al.* proposed an antiferro-

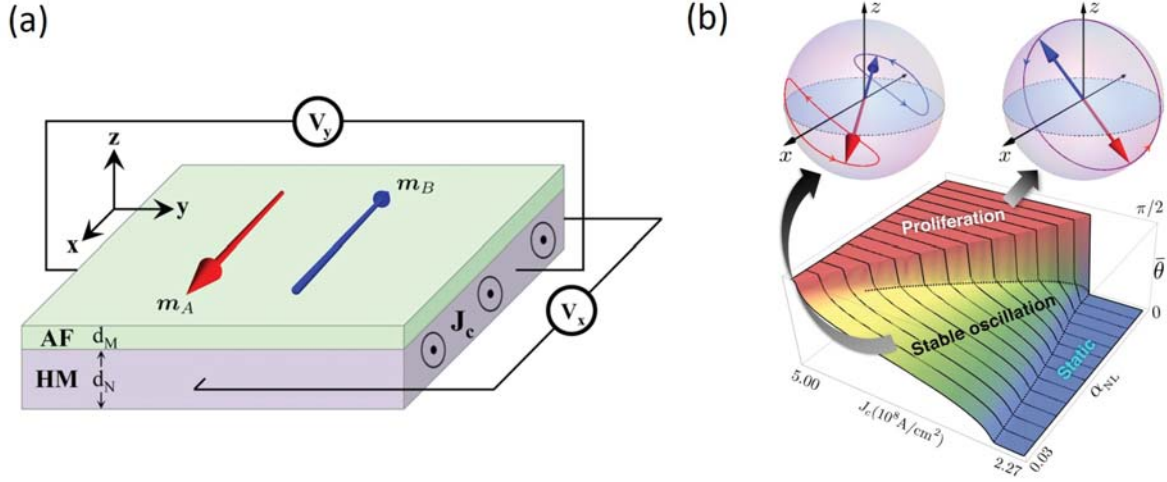


Figure 1.13: (a) An insulating AFM/HM heterostructure. Current density J_c creates a spin accumulation at the interface, which in turn drives the AFM. The detection is done by two voltmeters detecting the resistance changes via spin-Hall magnetoresistance. (b) Phase diagram of a SHNO based on NiO/Pt bilayer structure, showing stable oscillations and proliferation phases. Figures are taken from [34]

magnetic oscillator operating in the terahertz regime, using the feedback originating from the interplay of the spin Hall effect and the inverse spin Hall effect. They numerically explored the nonlinear Néel order dynamics in NiO/Pt bilayers and showed this feedback effect is essential to maintain uniform auto-oscillations.

Specifically, they showed that with increasing current density J and consequently the spin Hall torque, the frequency of the optical mode and the acoustic mode converges. At the a critical current J_c , when two modes become degenerate, terahertz excitations can be triggered and sustained. Furthermore, they showed that it is possible to get an AC output from this auto-oscillation and continuously tune its amplitude with the applied DC current. This theoretical work shows sufficiently large currents can trigger and sustain auto-oscillation of Néel vector with terahertz frequencies. And it is a major milestone in the route towards terahertz antiferromagnetic spin-torque oscillators.

1.7.2 SUBTERAHERTZ SPIN PUMPING FROM ANTIFERROMAGNET

Generation of pure spin currents are essential for creating antiferromagnetic spin-based devices. One proposed way of doing this is called spin pumping. Spin pumping — which is also the reciprocal phenomena of spin-transfer torque— is emission of a spin current into a metallic layer by driving magnetization of an adjacent layer. Because of the challenging nature of working with antiferromagnets, the direct observation of these effects remained elusive for a long time.

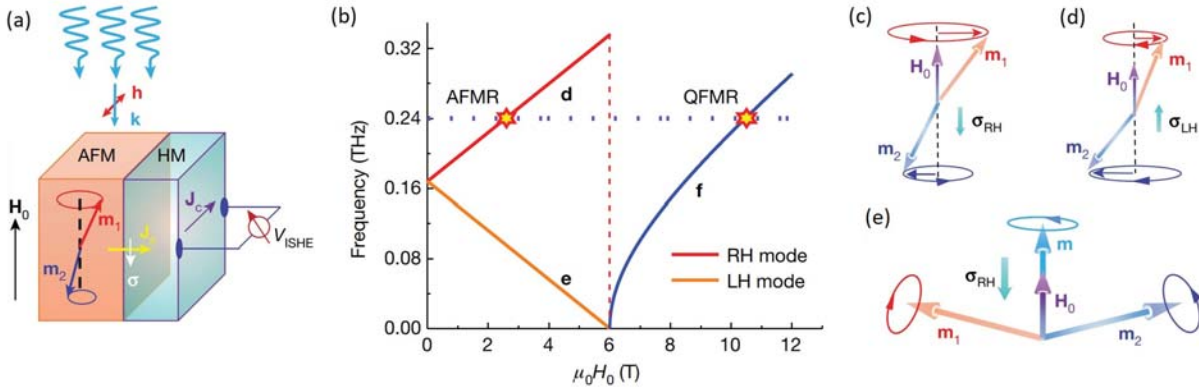


Figure 1.14: Illustration of spin-pumping from antiferromagnet Cr_2O_3 and spin current injection to heavy metal Pt. (b) Magnetic-resonance frequency as a function of the applied magnetic field along c axis of Cr_2O_3 . Eigenmodes of right-handed (c) and left-handed (d) antiferromagnetic resonance (AFMR). (f) Eigenmode of quasiferromagnetic resonance (QFMR) after spin-flop field. Figure is taken from [35].

In their 2020 Nature article [35], Li *et al.* demonstrated spin pumping in heterostructures of a uniaxial antiferromagnetic Cr_2O_3 crystal and a heavy metal Pt. They generated the spin currents by driving the AFM spin precession into resonance using linearly polarized sub terahertz radiation and detected the spin currents from adjacent heavy metal layers (Pt and Ta). They confirmed the nature of the signal by using two metals with opposite spin Hall angle and by switching the magnon chirality with applied field direction.

Similarly, in their 2021 Science article [36], Vaidya *et al.* showed first spin pumping signal originating from insulating antiferromagnet MnF_2 / heavy metal Pt bilayer structure. They excited and modulated the spin pumping by circularly polarized subterahertz irradiation, then measured

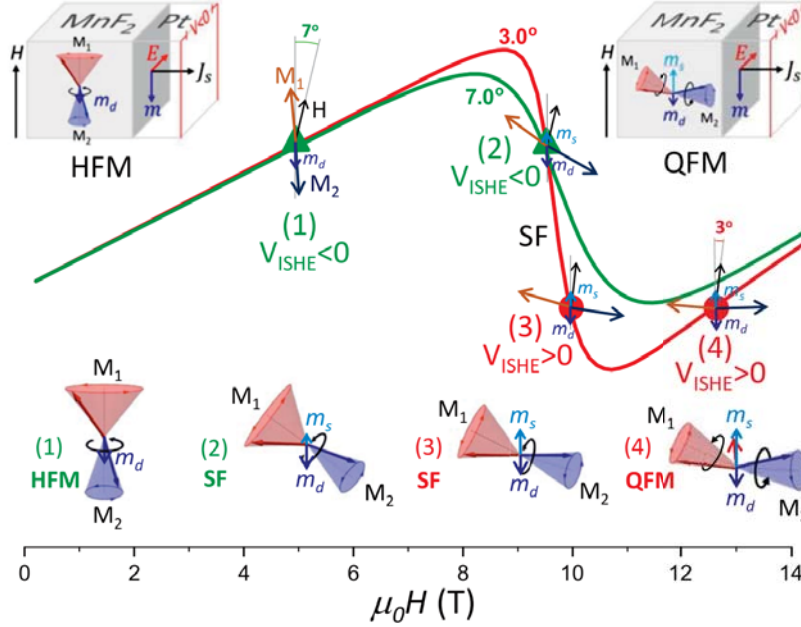


Figure 1.15: Evolution of spin dynamics of MnF_2 across the spin-flop transition. Illustration of sublattice magnetizations M_1 and M_2 at 4 different resonance points as a function of applied magnetic field. Figure is taken from [36].

ISHE voltage arising from spin-charge conversion in the platinum layer. They observed sign of the ISHE voltage depending on the handedness of the circularly polarized irradiation, confirming the spin-current origin of the ISHE signal.

Both of these studies are very important experimental milestones for next generation spintronics applications where antiferromagnets are used as active elements.

1.7.3 ELECTRICAL SWITCHING OF AN ANTIFERROMAGNET

Electrical control of antiferromagnets is an important milestone for realization of practical devices. It has been achieved in multiple systems such as CuMnAs [37, 38], Mn_2Au [39], Fe_2O_3 [29] and NiO [40]. But for most these experiments the mechanisms of switching is under debate. And for some of them, even the evidences for switching are not completely clear. The reasons for this ambiguity are related to methods of writing and reading the antiferromagnetic order, which

I will address shortly.

In their 2016 Science article Wadley *et al.* showed evidence of electrical switching between two stable configurations in antiferromagnetic CuMnAs thin films. They switched the Néel vector via torques generated by inverse spin galvanic effect and electrically detected the resistance changes by anisotropic magnetoresistance. The electrical readout of the switching showed saw-tooth behavior, meaning subsequent pulses from the same leads kept changing the resistance.

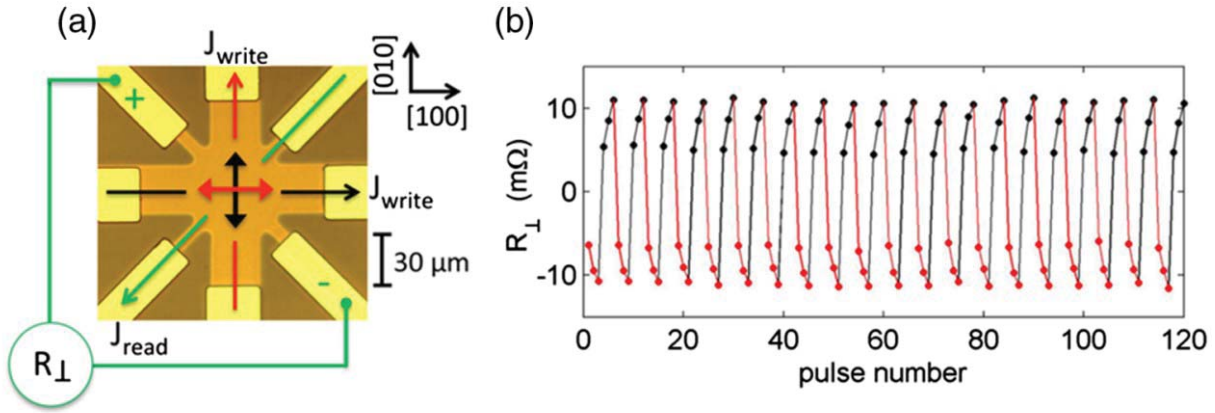


Figure 1.16: (a) Optical microscopy image of the 8-legged device and schematic of the measurement geometry. (b) Change in the transverse resistance after applying writing pulses. Figure is adapted from [37].

Similarly, in their 2020 letter Cheng *et al.* demonstrated electrical switching of tristate Néel order in bilayers heterostructures. They used high density current pulses to induce switching and detected the changes by spin-Hall magnetoresistance. Importantly they showed as-grown layers exhibit saw-tooth switching, but after annealing with a high current pulse, saw-tooth behavior vanished and only the nondecaying, steplike switching remained. They also showed saw-tooth switching is associated with artifact of Pt such as electromigration whereas the spin-orbit torque switching is steplike.

In the switching experiments, usually very high current density electrical pulses are used to generate torques from spin-Hall or inverse spin galvanic effects. But these pulses also create large thermal gradients and compressive stresses via Joule heating, which influence the magne-

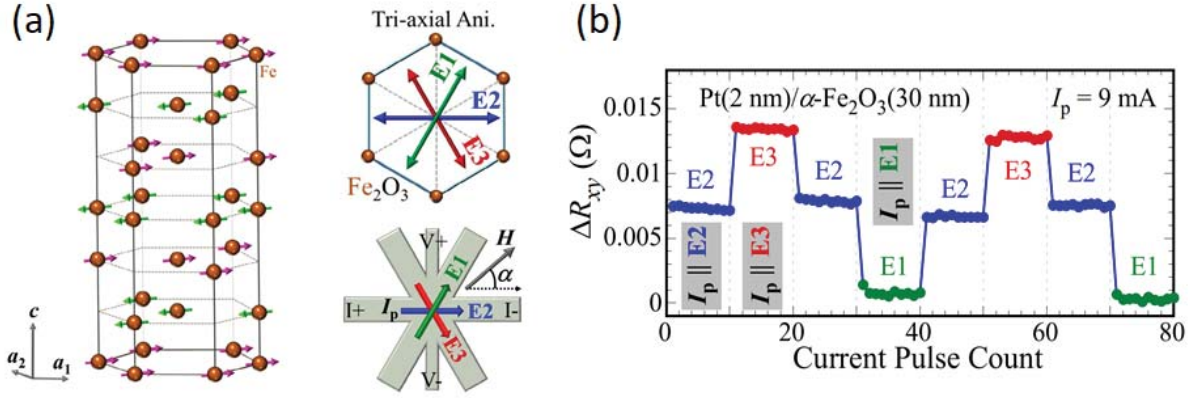


Figure 1.17: (a) Crystal structure, tri-axial anisotropy and schematic of the eight-leg Hall cross of Fe_2O_3 / Pt bilayer. Figure is adapted from [29].

tization dynamics through magneto-elastic effects. Additionally the contribution of torques and magneto-elastic effects are not easily separable because they share the same type of symmetries. Therefore, it is not always clear whether the spin torques are the dominant contributor to the switching or not. To read the state of Néel vector electrically usually some form of anisotropic magnetoresistance is used both in metallic and insulating antiferromagnets. The issue with relying only the resistance data is that there are many mechanisms with non-magnetic origin can produce the similar "switching" evidence.

In fact, in their 2019 article in Physical Review Letters Chiang *et al.* [41], showed the absence of evidence for magnetic switching in these electrical detection experiments. In a series of controlled experiments, they have recreated the sawtooth like switching in Pt Hall crosses with and without a magnetic layer. They also studied the effect of the substrate by growing Pt on different on glass, silicon and MgO. At the end, they showed that resistance data is not a conclusive evidence of spin-orbit torque switching of AFM, and high current densities can induce changes to the resistance due to intense heating and electromigration.

Similarly in their 2020 article in Applied Physics Letters Churikova *et al.* [42], showed non magnetic origins of the saw-tooth like switching associated with electromigration heating effects

in Pt layer. First they reproduce sawtooth-like switching experiments both in NiO/Pt and Pt layers, proving once again electrical data cannot be the single proof of magnetic switching. Then they imaged the Hall-cross structure after the experiments using scanning electron microscopy and documented the damage caused by high density current pulses, especially at the corners where current densities tend to be the highest.

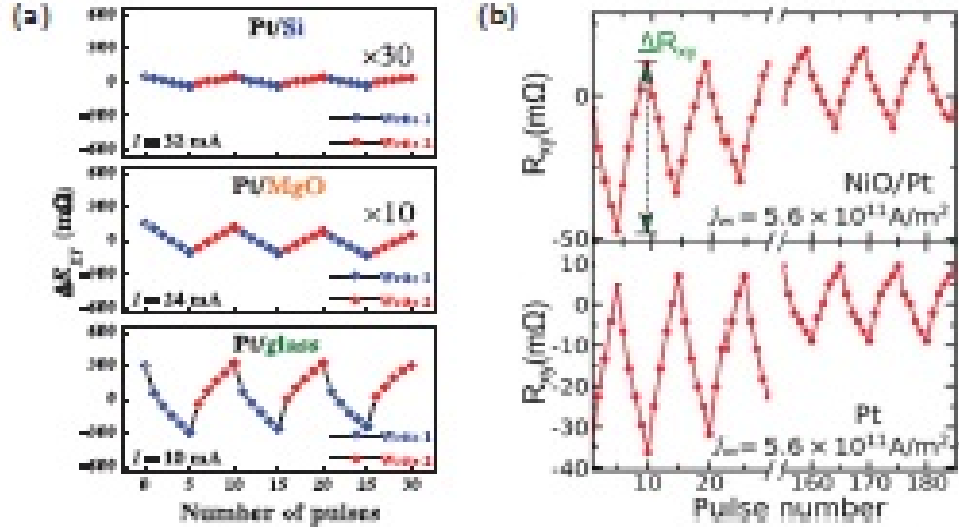


Figure 1.18: (a) Electrical "switching" signal in transverse resistance of Pt grown on Si, MgO and glass substrates, without any antiferromagnetic layer. (b) Comparison of transverse resistances in NiO/Pt and only Pt. All samples show saw-tooth behavior which is associated with electromigration in Pt, rather than antiferromagnetic switching. Figures are adapted from [41, 42].

Both of these studies show the importance of direct evidence of actual antiferromagnetic reorientations, as opposed to relying only on electrical data, as it is indirect measurement and there can be many origins of the observed signal. Therefore using direct techniques such as X-ray microscopy becomes very important as it can unambiguously show magnetic changes and provide local information.

1.7.4 OVERVIEW OF THE DISSERTATION

With the ultimate goal of creating the practical devices from antiferromagnetic materials, the field of antiferromagnetic spintronics have a couple of clear milestones to achieve along the way. Among these are (i) creating and sustaining oscillations of the antiferromagnetic order, and (ii) reliably controlling the state Néel vector. To achieve either of them, a robust way to influence antiferromagnetic order is needed. Spin-orbit torques are one of the most promising ways to achieve this, as they are electrical in nature and they have been studied for their applications in ferromagnetic systems. With these goals in mind, we conducted two studies: imaging of current-induced switching of antiferromagnets and then we used harmonic Hall measurements to quantify the spin-orbit torques in the same system.

Chapter 2 summarizes imaging studies of antiferromagnets NiO and α -Fe₂O₃ using X-ray photoemission electron microscopy. Imaging studies are especially crucial because it is direct measurement of magnetic configuration and thus doesn't come with any ambiguity unlike electrical measurements. We first look at the equilibrium configuration of antiferromagnetic domains and then image their response to current pulses. Indeed, we observe current pulses lead to reversible and repeatable switching, with the current direction determining the final state, confirming the results coming from electrical Hall signal. Furthermore, our detailed analysis of images taken with different x-ray polarizations reveals the AFM Néel order has an out-of-plane component in equilibrium that is significant and not detectable with electrical data. But we also see changes outside of the current path suggesting that changes to AFM order can be induced by purely thermal effects.

Chapter 3 focuses on characterizing the spin-orbit torques (SOT) associated with AFM/heavy metal (HM) interfaces. We show full angular dependence of the harmonic Hall resistances in α -Fe₂O₃ films, with an interface to Pt. Then we develop a model to the harmonic Hall signals and extract the amplitudes of field-like and damping-like SOT by fitting experimental data to

the model. Out-of-plane field scans are shown to be essential to determining the damping-like component of the torques. Interestingly, our results demonstrate that the field-like torques are significantly larger than the damping-like torques, which we correlate with the presence of a large imaginary component of the interface spin-mixing conductance. our results demonstrate that the field-like torques are significantly larger than the damping-like torques, which we correlate with the presence of a large imaginary component of the interface spin-mixing conductance.

Finally, in chapter 3, after summarizing the conclusions drawn from the experiment. I will talk about possible next steps, some open questions and perspectives on the state of the field.

2 | IMAGING ANTIFERROMAGNETIC ORDER USING X-RAYS

2.1 INTRODUCTION

The electrical control of antiferromagnetic (AFM) order is a topic of great current interest that has been enabled by recent advances in spintronics, specifically the ability to produce spin currents and spin torques based on spin-orbit interactions [15, 43–45]. Current-induced switching has been reported in AFM thin films using electronic transport signatures such as anisotropic magnetoresistance to infer domain reorientation [8, 29, 37, 39, 46–51]. However, recent studies of NiO show that such inferences can be inaccurate because electromigration can lead to the same transport response as that attributed to switching of AFM domains [41, 42]. Microscopy techniques have been used to study the switching of domains in metallic AFMs [52, 53], but there are few reports of such studies on insulating AFMs. It is thus critical to have more direct information on the AFM domain response to electrical pulses to advance the understanding of their spin dynamics.

In this chapter, I will focus on imaging studies of antiferromagnetic order of two materials, α -Fe₂O₃ and NiO, which are both insulating antiferromagnets. One of the best techniques to image antiferromagnetic domains is using X-ray Magnetic linear dichroism in photo-emission microscopy (XMLD-PEEM), which is only available in synchrotron facilities. In each subsection,

I will introduce the samples and details of the experimental setup, then I will discuss the results of the microscopy experiments. In α -Fe₂O₃ samples, I will discuss both equilibrium configuration of AFM domains and their response to electrical pulses, whereas for NiO samples, only equilibrium configuration of AFM domains will be discussed.

2.2 IMAGING EXPERIMENTS ON α -Fe₂O₃

This section focuses direct observation of switching of the Néel vector of antiferromagnetic (AFM) domains in response to electrical pulses in micron-scale Pt/ α -Fe₂O₃ Hall bars using photoemission electron microscopy. We showed that current pulses lead to reversible and repeatable switching, with the current direction determining the final state, consistent with Hall effect experiments that probe only the spatially averaged response. Current pulses also produce irreversible changes in domain structure, inside and outside the current path. In both cases only a fraction of the domains switch in response to pulses. Further analysis of images taken with different x-ray polarizations shows that the AFM Néel order has an out-of-plane component in equilibrium that is important to consider in analyzing the switching data. These results show that—in addition to effects associated with spin-orbit torques from the Pt layer, which can produce reversible switching—changes in AFM order can be induced by purely thermal effects.

2.2.1 SAMPLE CHARACTERISTICS

All experiments were performed on 30 nm thick epitaxial α -Fe₂O₃ grown on single crystalline c-axis oriented Al₂O₃ substrates at 500°C using off-axis sputtering [29]. The films were capped in-situ with a 2 nm Pt layer deposited at room temperature. For the Hall-cross structures, e-beam lithography and reactive ion etching were used to pattern the Pt layer into 6-legged structures with 1 μ m wide Pt leads. The Hall-cross structure was oriented such that the Pt leads coincide with the three easy in-plane axes ([1000],[0100],[0010]) of c-axis oriented α -Fe₂O₃ [29].

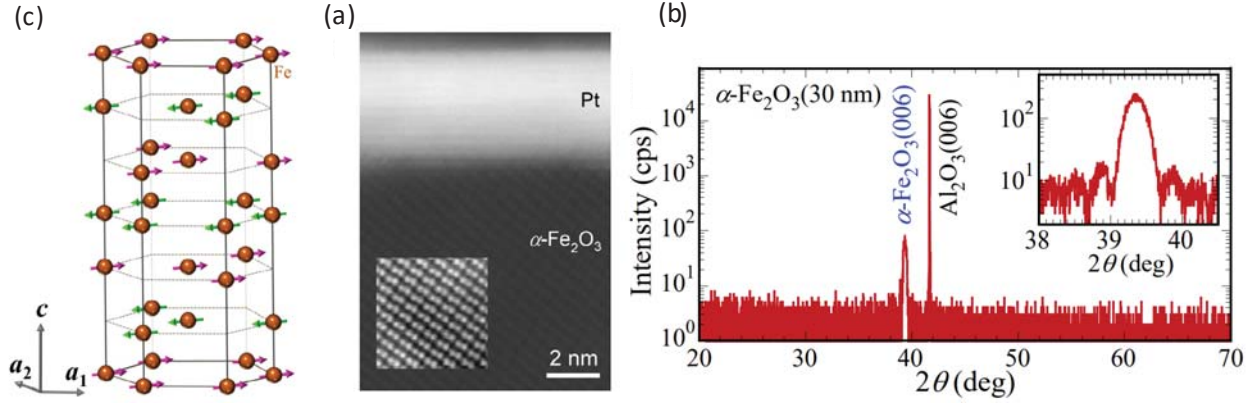


Figure 2.1: (a) Hexagonal crystal structure of antiferromagnetic $\alpha\text{-Fe}_2\text{O}_3$. Fe moments are ferromagnetically coupled within c-planes, and antiferromagnetically coupled across c-planes. (b) STEM image of the cross section of $\alpha\text{-Fe}_2\text{O}_3$ (30 nm)/Pt (2) bilayer. The inset shows the atoms with higher adjusted brightness. (c) X-ray diffraction of epitaxially grown $\alpha\text{-Fe}_2\text{O}_3$ on Al_2O_3 . $2\theta / \omega$ scan shows $\alpha\text{-Fe}_2\text{O}_3$ (006) peak indicating high crystalline quality. Figure is adapted from [29].

Hexagonal crystal structure of $\alpha\text{-Fe}_2\text{O}_3$ with ferromagnetically coupled Fe moments in the c-plane and antiferromagnetically coupled across adjacent c-planes is shown in Fig. 2.1. In bulk iron oxide, there is a magnetic transition at 260 K also known as the Morin temperature, $T_m = 260\text{K}$ [54]. Above T_m , the spins orient in (111) planes directed towards the three nearest neighbors. In this state, the spins are also canted slightly out of the plane, giving rise to small net moment along the [111] axis. Below T_m , the magnetic arrangement has Fe spins directed along the [111] axis and still antiferromagnetically coupled along this axis with zero excess moment. In thin films the Morin transition is suppressed [55] and mechanism for the suppression is also under debate. For our samples, there has been no evidence of reduced net magnetic moment at as low as 200 K [29], indicating suppression of Morin transition.

2.2.2 EXPERIMENTAL SETUP

Our experiments were designed to detect the AFM domain structure and changes to this structure in response to current pulses. They were carried out at the PEEM3 beamline 11.0.1.1 of the Advanced Light Source at Lawrence Berkeley National Laboratory (LBNL) in the geometry shown

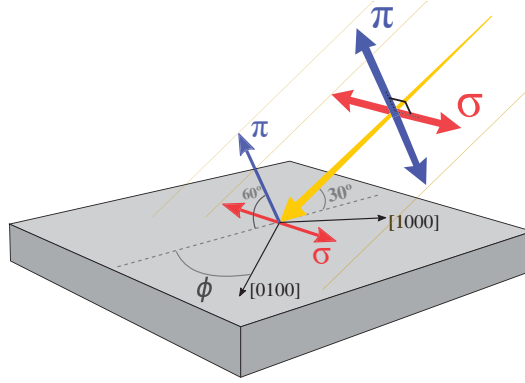


Figure 2.2: σ and π polarizations of x-rays and their projections on the sample at ALS PEEM3 Beamline 11.0.0.1. In rotation experiments, the sample was rotated by the small azimuthal angle ϕ , projections along π and σ polarizations can be varied.

in Fig. 2.2(a) [56]. X-rays were incident at a 30° angle to the film surface and polarized either in the plane of incidence, labeled π polarization (blue arrow), or perpendicular to this plane, σ polarization (red arrow). In this configuration, σ polarization is completely in the film plane, whereas π polarization is at an angle of 60° to the film plane. Moreover, the energy of the incoming photons are adjustable in the an energy range of 160 eV - 1800 eV, which covers wide range of element L edge core level transition energies. During the experiment they are chosen to be resonant with the Fe L_{2a} and L_{2b} edges making their absorption dependent on the magnetic order.

For pulsing experiments, the sample needs to have at least 4 electrical connections for two different pulse configurations, which can be provided by electrical sample holder (Fig 2.3b). First the sample needs to be bonded to ceramic leadless chip carriers (Fig 2.3a) that can provide 4 signal and 2 ground connections. 2 of these connections are RF up to 100 MHz in frequency and can supply voltage and amperage up to 400 Volts and 2 Amps. The other two are 2 DC connections which can go up to 100 Volts and 5 Amps. In our experiments we only use DC pulses and the amount of current needed is usually fraction of the voltage/amperage upper limit. During the exposure to x-rays sample surface must be floating at high voltage above 10 keV, therefore ground connections are not useful for our case.

There is also rotation holder Fig 2.3c that rotates the sample in a fast and continuous way.

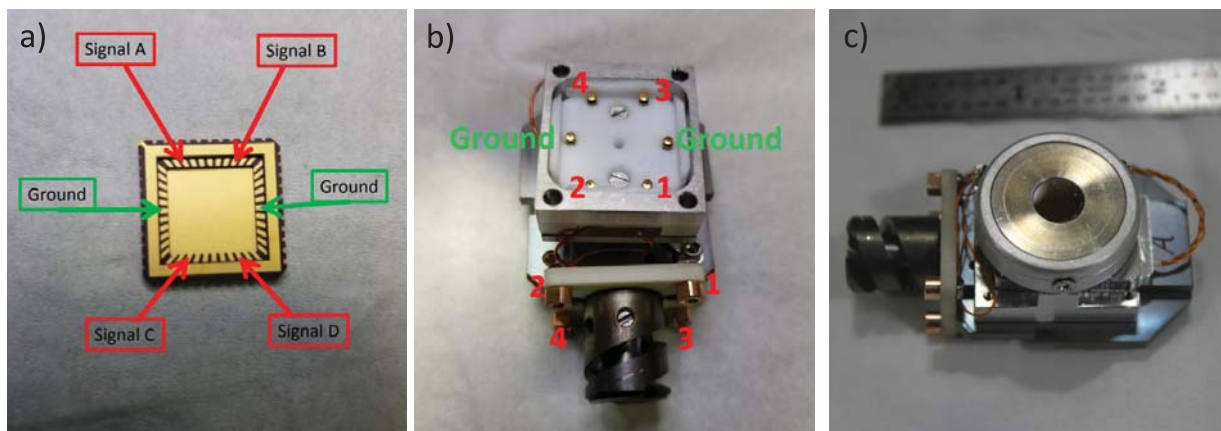


Figure 2.3: (a) Commercially available leadless chip carrier that holds the sample. There are total of 6 possible connection where 2 of them are connected to the ground. (b) Custom PEEM sample holder for electrical measurements at ALS Beamline 11.0.1.1.

This allows the user to change in-plane projection of the x-ray polarization onto the sample. This technique can be used to gain more information on the 3D orientation of the Néel vector, which will be discussed later in the chapter.

2.2.3 ELECTRICAL MEASUREMENT CONFIGURATION

Before taking the samples to synchrotron to do XMLD PEEM experiments, we characterized the samples electrically in the lab. Current pulses were applied across different leads for switching and the transverse voltage was measured for detection.

For sensing, A 100 μA DC current is applied along one of the easy axes and the Hall voltage is measured from the combination of remaining 2 axes. Figure 2.4(a) shows the electrical circuit used for measuring the Hall voltage of a sample. Combining the four leads with resistors allows us to measure the transverse voltage minimizing the longitudinal voltage. Figure 2.4(b) shows the resulting data, as also shown in Fig 2.9. Note that in this configuration only one current pulse generator is connected to the sample.

For switching experiments we used two pulse generators at the same time, creating two pulse configurations named pulse A and pulse B. As an example, the data shown in Fig. 2.4(b) is for

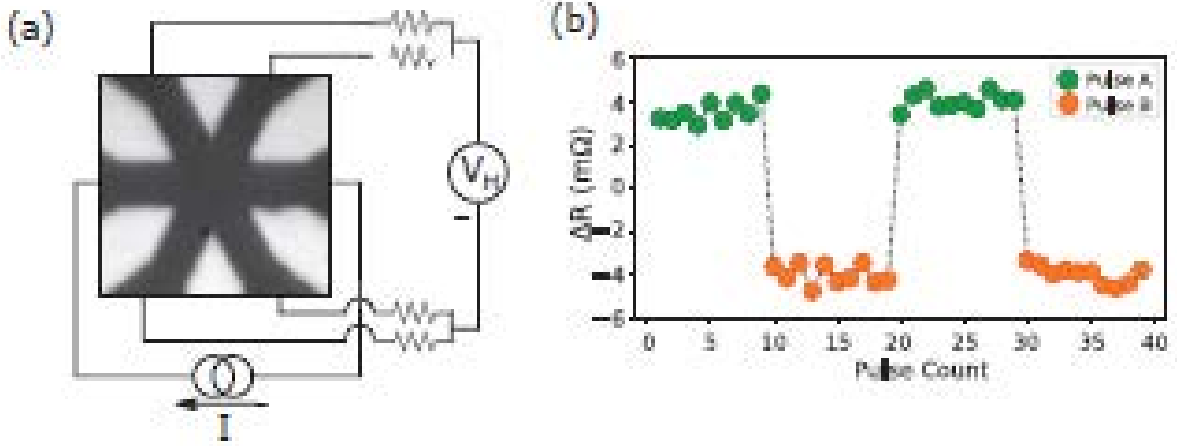


Figure 2.4: (a) Circuit diagram for measuring the Hall voltage of 6-legged Hall-cross. (b) Transverse resistance measurements in response to 4 mA, 10 ms pulses A and B along two of leads coinciding with easy-axes. The two-point resistance of the sample measured is approximately 5 kΩ. The resistors are chosen so that they compensate for the small differences in resistance coming from different leads.

4 mA amplitude 10 ms duration pulses. After each pulse a small sensing current $100 \mu\text{A}$ ($\ll 4$ mA) was used to measure the transverse voltage. The data points are color coded according to the pulse type. As reported previously, there is a step change in voltage when going from A to B type pulses as well as going from B to A type pulses [29]. Further, subsequent pulses of the same type do not change the transverse voltage, meaning we don't see sawtooth-like switching.

We also created a phase diagram of switching resistances (ΔR) as a function of pulse amplitude and pulse width. For each pulse amplitude and pulse width a switching experiment like one in Fig. 2.5(a) is conducted. In one switching experiment a total of 40 pulses is sent, alternating the pulse configuration between A and B, every 10 pulse. Then the difference between average resistance level for pulse A and pulse B is recorded as the switching amplitude ΔR . In total, we explored 88 switching configurations from $2.5 \times 10^7 \text{ A/cm}^2$ to $6 \times 10^7 \text{ A/cm}^2$ to (5 mA up to 12 mA in the $10 \mu\text{m}$ linewidth Hall cross) in pulse amplitude and from $10 \mu\text{s}$ up to 1 s in pulse width. Figure 2.5(b) summarizes our findings. No switching events with pulse widths of $10 \mu\text{s}$, $50 \mu\text{s}$ and $100 \mu\text{s}$ occurred. Similarly there is no switching events with $2.5 \times 10^7 \text{ A/cm}^2$ pulse amplitude. In general switching amplitude (ΔR) increases with increasing pulse width and

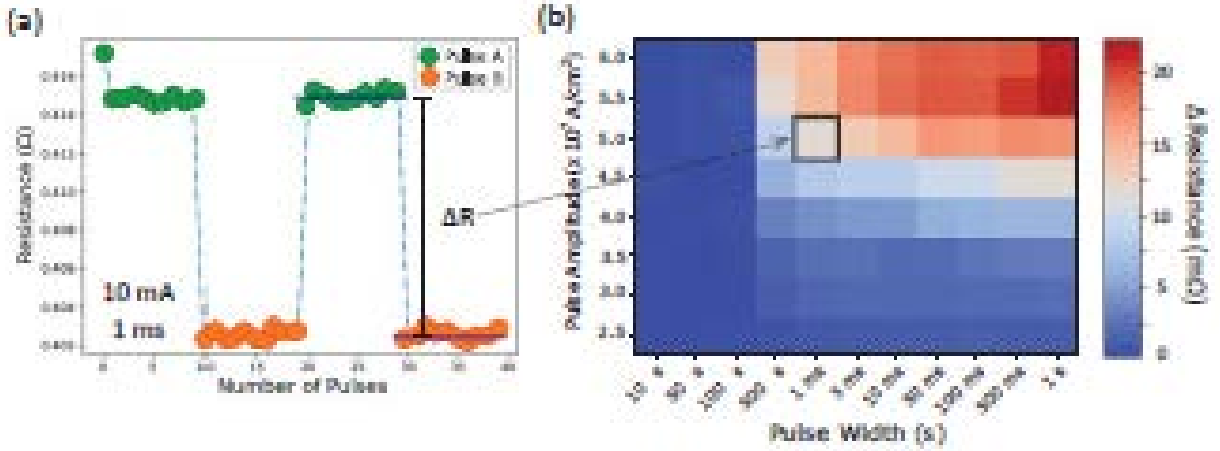


Figure 2.5: Switching amplitude as a function of pulse width and pulse amplitude (a) Heat-map. (b) 3-D Phase diagram. Both of the plot show the same data, just different representation.

pulse amplitude. Existence of minimum threshold currents is expected for both spin-orbit switching and Joule-heating-induced magneto-elastic effects. But the fact that switching amplitude ΔR keeps increasing with increasing pulse width suggests that thermal effects are contributing to switching, as thermal energy is proportional to the pulse duration.

2.2.4 IMAGING ANTIFERROMAGNETIC DOMAINS

In this study our goal is to correlate the already demonstrated electrical switching with actual changes in the antiferromagnetic domain structure. Therefore our first step was to image equilibrium domain structure in the Hall-cross structures in the same devices that we see the electrical signs of switching. Figure 2.6(a) shows the optical microscopy image of the original 8-legged Hall-cross, identical to the one that is used in [29]. Figure 2.6(b) shows the XMLD-PEEM image of the same device taken at PEEM3 microscope at Advanced Light Source. PEEM image naturally has a much smaller field of view and the one of bottom left bare α -Fe₂O₃ regions is visible. The domain structure is clearly visible both in bare α -Fe₂O₃ regions (light section) and through the Pt (dark sections). These images are calculated by taking the asymmetry of images taken at L_{2a} and L_{2b} energies, then normalized with L₂ pre-edge energy. I will discuss calculation of XMLD

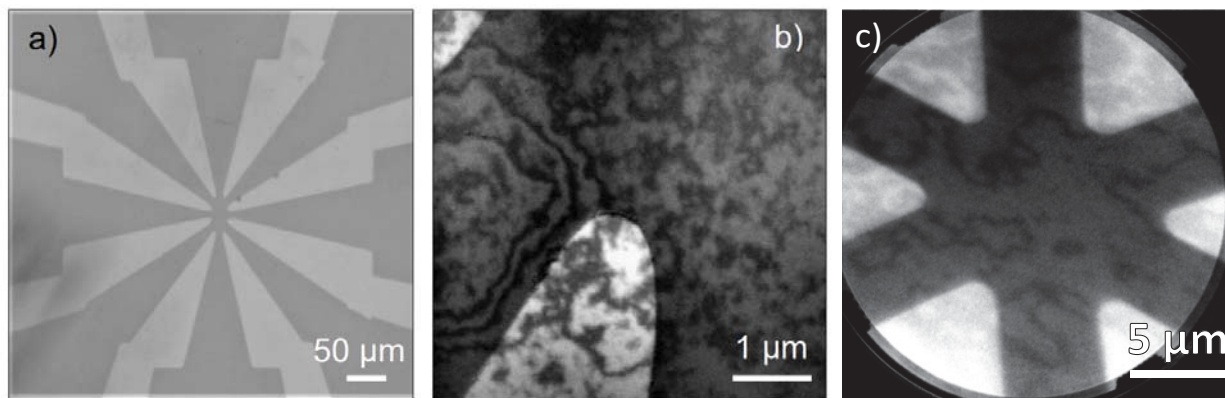


Figure 2.6: Figure 2. (a) Optical microscopy image of the original 8-legged Hall-cross. Field of view is 0.5 mm (b) XMLD-PEEM image of antiferromagnetic domains in the same sample. (c) XMLD-PEEM image of antiferromagnetic domains in the 6-legged Hall-cross. Dark regions are Pt and bright regions are bare α - Fe_2O_3 . In both samples, domains are visible in bare regions and through the 2 nm platinum layer. Images are calculated by taking asymmetry at L_{2a} and L_{2b} edges and normalized to L_2 pre-edge. Field of view is 5 μm .

images in detail in section 2.2.6.

During one of our first imaging experiments, we also sent some electrical pulses to test the Hall-cross structure and the experimental setup. One thing that is really challenging about working with nano-fabricated devices with electrical connections in PEEM is the fact that the sample surface has insulating areas - bare α - Fe_2O_3 . When these surfaces are exposed to x-rays, photoelectrons accumulate at these sections. This causes charging issues and from time to time, unwanted electrical discharges can occur from the microscope objective lens to the sample surface. Given the fact that our devices have micrometer wide and nanometer thick leads, these discharges causes large amount of currents to pass through the device and damage the sample by destroying the leads.

One of these electrical charges happened during our tries of sending electrical pulses and destroyed the leads of the sample. But in general destroyed leads do not interfere with taking PEEM images. So we have imaged before and after electrical pulse/discharge events and observed the induced changes. Figure 2.7 summarizes the findings. Figure 2.7(a) shows before and after images where domains in the form of dark spots are visible. When comparing images side by

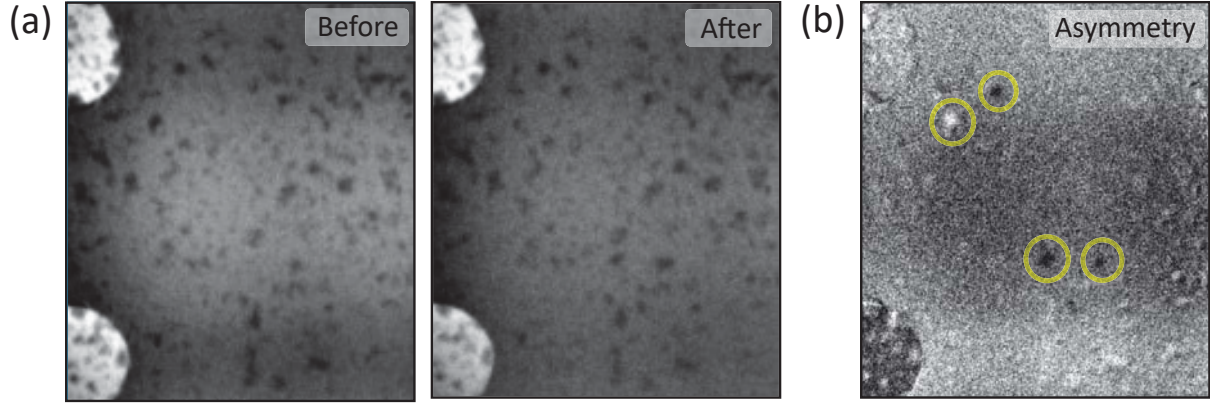


Figure 2.7: XMLD-PEEM Images of the region of interest before (a) the pulse. Both images are calculated by taking asymmetry of L_{2a} and L_{2b} edges, then normalizing with L_2 pre-edge. (b) Asymmetry of before and after images. Antiferromagnetic domain structure shows small changes after the current pulse, which can be seen as black and white spots in the image. Largest changes are circled in yellow. Field of view is $10\ \mu\text{m}$.

side it is not easy to notice the small differences between them. Therefore in Fig. 2.7(b) shows the asymmetry $((I_{\text{Before}} - I_{\text{After}})/(I_{\text{Before}} + I_{\text{After}}))$ of before and after images. Changes in domains now appear as black and white spots. The largest differences in AFM domains are highlighted with yellow circles. All three images are approximately $10\ \mu\text{m}$ in field of view.

In summary, in our initial try, we have imaged equilibrium configurations antiferromagnetic domains with nominal size of $1\ \mu\text{m}$ in $\alpha\text{-Fe}_2\text{O}_3$ using XMLD - PEEM. We have observed changes in AFM domains induced by an electrical discharge. Since we want to minimize the chance of another electric discharge occurring, we decided to decrease the surface area of bare insulating $\alpha\text{-Fe}_2\text{O}_3$ as we updated the design of the Hall cross. The update Hall-cross has a reduced area and $1\ \mu\text{m}$ channel width. This came with the extra benefit of reducing to active area in the middle of the Hall cross to the average size of a domain which is $\approx 1\ \mu\text{m}$. In the next section we will look at current induced changes in $1\ \mu\text{m}$ wide lead Hall crosses.

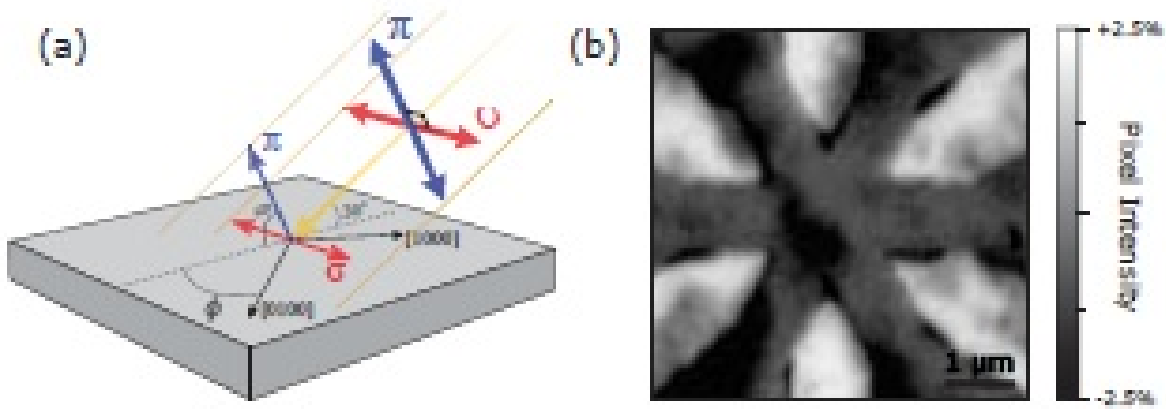


Figure 2.8: (a) Schematic of the experimental setup showing the two incident X-ray polarizations, σ and π , and their projections on the sample. The sample was rotated by a small azimuthal angle, ϕ , so that the $[1000]$ and $[0100]$ crystal axes have different projections along π and σ polarizations. (b) XMLD-PEEM image of the 6-legged Hall cross with AFM domains visible both on bare Fe_2O_3 regions (lighter regions) and under the 2 nm thick Pt layer (darker regions). The scale bar indicates the percentage contrast, relative to the background.

2.2.5 IMAGING CURRENT INDUCED CHANGES

In this section, we use x-ray microscopy to directly observe AFM domain structure in Pt/ α - Fe_2O_3 Hall bars and their response to electrical pulses. Spatially and element resolved x-ray magnetic linear dichroism (XMLD) photoemission electron microscopy (PEEM) reveals reorientation of Néel vector, where the current flow direction repeatably sets and resets the domain orientation. However, domains outside the current path generally switch irreversibly. In both cases, only a small region near and in the Hall cross switches. Further, our analysis of images taken with different x-ray polarizations reveals an out-of-plane component to the Néel vector in equilibrium, that is, before current pulses are applied to the sample. These results are consistent with switching of the Néel vector between states with in and out of the plane spin components.

The XMLD response allows characterization of the AFM order both in with σ polarization and out of the film plane, with π polarization x-rays (Fig. 2.8(a)). The XMLD contrast is typically a few percent, which is easily detectable with PEEM. Figure 2.8(b) shows an example XMLD-PEEM image of the sample. The darker regions are covered with the thin Pt layer and the brighter

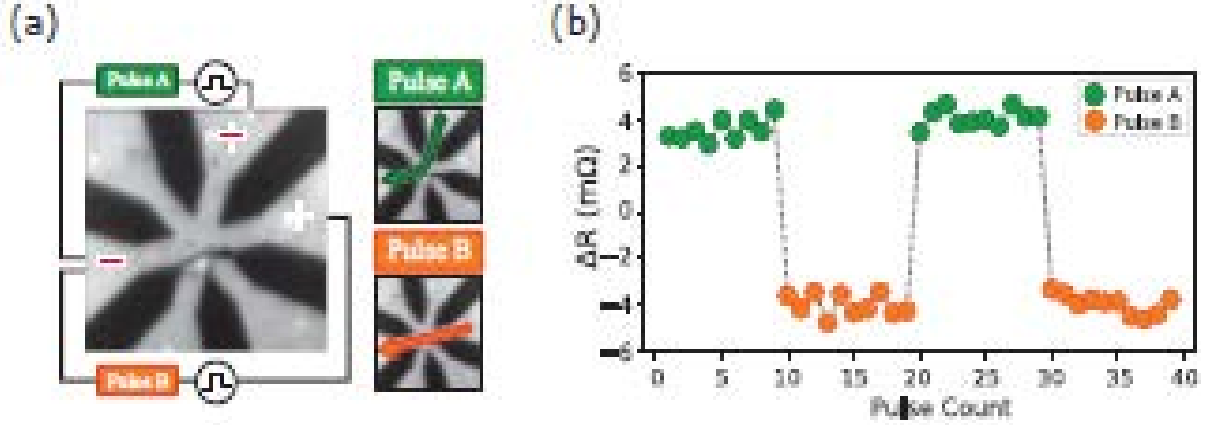


Figure 2.9: (a) Left: PEEM image with a schematic of the circuit. Bright regions correspond to Pt covered areas and dark regions to bare Fe_2O_3 . Pulses were applied from “+” to the ground, “-”, for both pulse generators. Right: Pulse A and Pulse B panels show the current path for each pulse. The dark line at the bottom of the central part of the Hall cross is a cut disconnecting the two bottom leads from the current path. (b) Transverse resistance measurements in response to 4 mA, 10 ms pulses A and B on a sister sample with the bottom leads connected.

regions are where the Pt is etched, exposing the $\alpha\text{-Fe}_2\text{O}_3$ surface. AFM domains are observed in both regions. Their boundaries are gray to black contrast changes in the Pt covered regions and the white to gray transitions in the $\alpha\text{-Fe}_2\text{O}_3$ exposed regions. The lateral scale of the domains is $\sim 1 \mu\text{m}$ and domains extend between the two regions.

To characterize the orientation of the Néel vector, XMLD images were acquired as a function of the sample orientation, ϕ in Fig. 2.8(a). XMLD contrast depends on the magnitude of the projection of the x-ray polarization \hat{p} on the Néel vector \hat{n} , $(\hat{p} \cdot \hat{n})^2$. Therefore, for in-plane oriented spins, XMLD images are invariant under a 180° sample rotation for both σ and π polarizations. Based on the spin structure and studies of $\alpha\text{-Fe}_2\text{O}_3$ thin films, we expected the Néel vector to be oriented along in-plane easy axis directions [29, 49, 54] and thus that both sets of images would be invariant under 180° sample rotation. However, surprisingly, our results show that for π polarization, the image contrast changes significantly on 180° rotation. The σ polarization images return to the same contrast levels on rotation, as expected. This indicates that, in addition to having different in-plane projections, the AFM Néel vector at the sample surface is appreciably

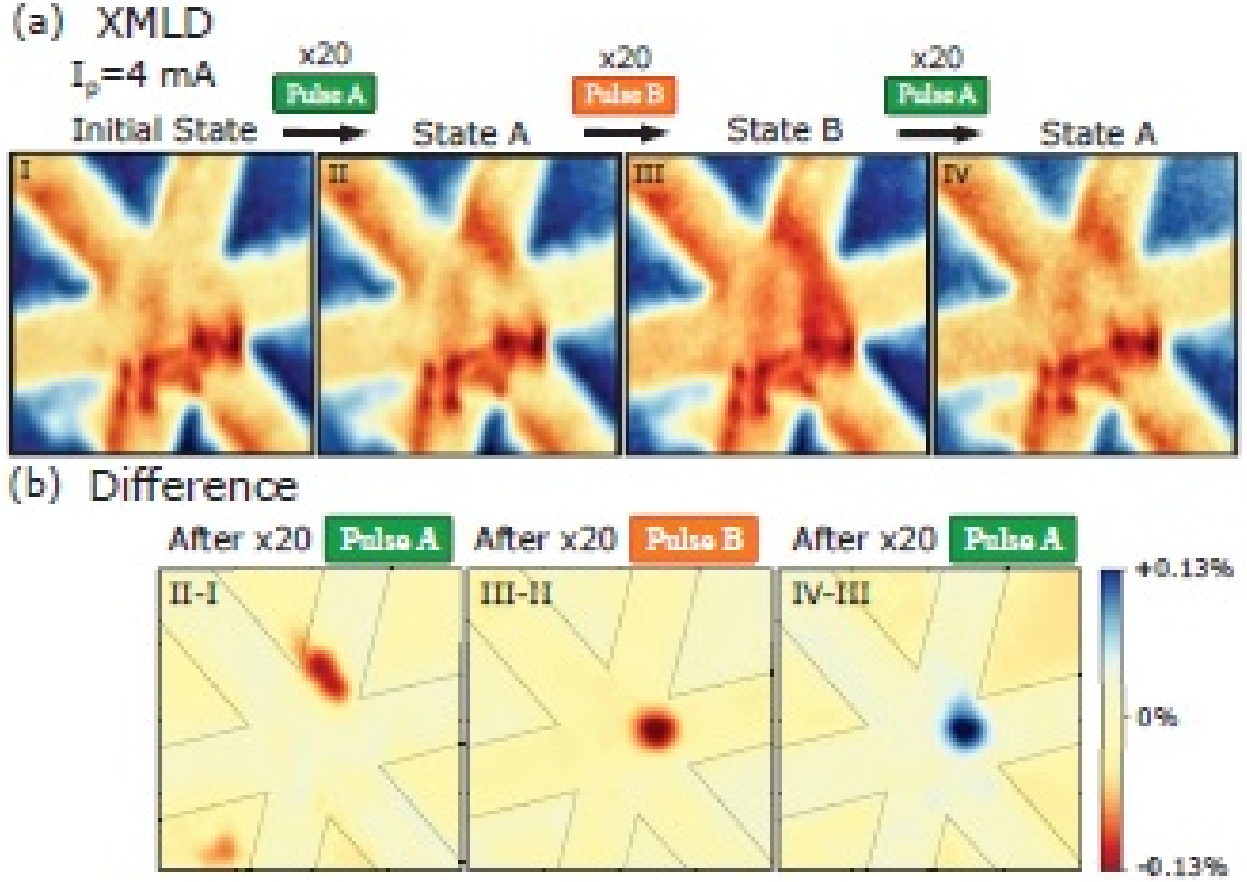


Figure 2.10: AFM domain changes in response to current pulses. (a) XMLD images showing a $4 \times 4 \mu\text{m}^2$ field of view. Image I shows the sample before current is applied; Images II, III and IV are images taken after the application of 20 current pulses of type A, type B and then type A, respectively. The pulse amplitude is 4 mA for all the images in the sequence. (b) Differences of XMLD images in panel (a) to highlight the pulse induced changes to AFM domain structure. The color scale in (b) is expanded to highlight changes.

canted out of the film plane, which may reflect an interface perpendicular magnetic anisotropy. We discuss conclusion further in "Spins canted out-of-plane equilibrium state" section later in this chapter.

The effect of electrical pulses on the AFM domain structure were studied by applying currents to the Hall bar in situ, with the sample in the PEEM microscope. Prior electrical studies have shown that the current flow direction leads to different transverse (Hall) voltages that were associated with changes in the AFM domain structure [29, 49]. Thus we configured the sample to enable current pulses to be applied in two different directions. Figure 2.9(a) shows the sample

layout with connections to two separate pulse generators, labeled A and B. The images on the right of Fig. 2.9(a) show the current directions for A and B pulses.

Figure 2.10(a) shows a sequence of four XMLD images taken before and after applying current pulses. They show the difference in the electron yield for σ and π polarization to maximize the signal originating from AFM order. Blue regions are bare Fe_2O_3 , and red/orange regions correspond to the Pt leads. The field of view is $4 \times 4 \mu\text{m}^2$. Image I shows the initial domain configuration before pulses were applied. Images II, III and IV show the states after sending a sequence of 20 of the same pulse type, first pulse A, then B, and then A again. The labels “State A” and “State B” above the images correspond to the preceding pulse type. Changes in AFM order correspond to color changes between subsequent images. For example, in Image II there is added contrast in the pulse A positive lead after 20 type A pulses and in Image III a domain to the right of the center of the Hall cross has reoriented after 20 type B pulses. While in Image IV, after A pulses, this domain has returned to its initial configuration.

To bring out the changes in AFM domain structure we show difference images in Fig. 2.10(b). In these images blue regions represent positive contrast changes and red regions negative contrast changes. The color map is chosen to highlight the current-induced changes; the black lines indicate the boundaries of the Pt leads. The II-I Image clearly shows the domain that has reoriented in response to the first set of A pulses is in one of the current leads to the Hall cross. Image III-II shows the domain that has switched in the Hall cross area in response to B pulses. After another set of A pulses, the contrast returns to that after the first set of A pulses, “State A,” the state shown in Image II of Fig. 2.10(a).

From these results, we identify two types of domain changes in response to current pulses: 1) reversible changes, regions that go back and forth between State A and State B after the corresponding pulses; and 2) irreversible regions in which the domain configuration does not return to its initial state. The reversible changes occur in regions in which the current density is large and its flow direction changes significantly between that of pulse A and B. In both cases, it is

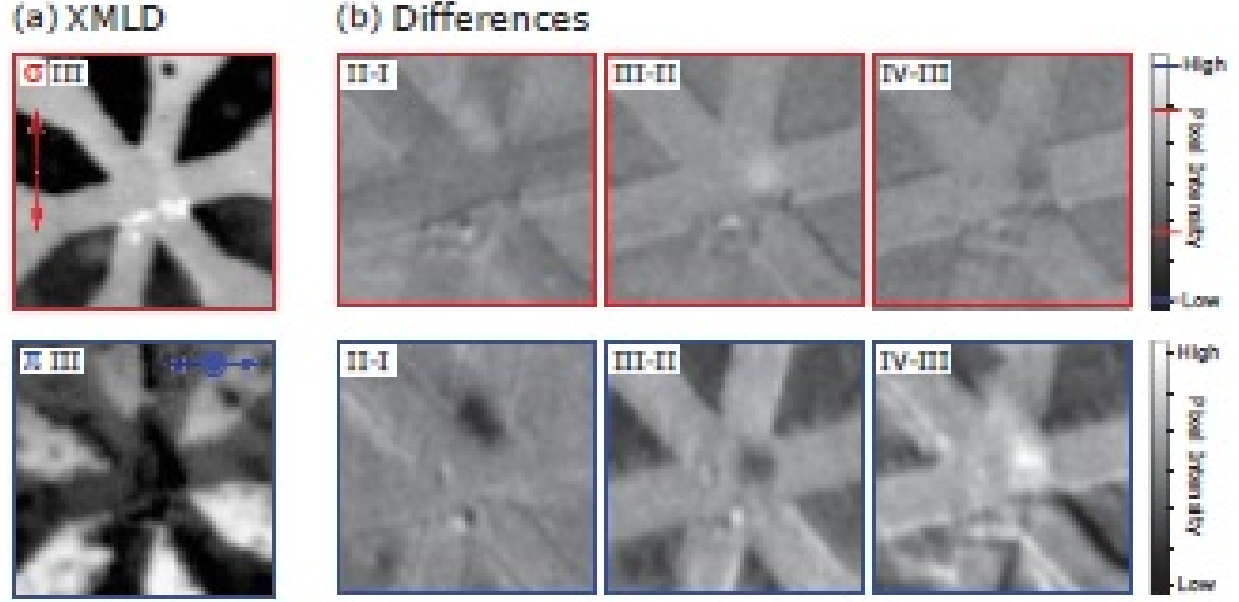


Figure 2.11: (a) σ and π projections of Image III in Fig. 2.10a. Bright regions indicate that the AFM order is aligned perpendicular to the polarization direction whereas dark regions indicate that the AFM order aligns parallel to the polarization direction. (b) σ (top panel) and π (bottom panel) projections of the difference images in Fig. 2.10b. The same scale bar is used on both panels to highlight the larger contrast in the π polarization images. The marks on the σ color scale bar show the maximum and minimum values for σ (red marks) and π (blue marks) polarization difference images.

also clear that the Néel vector of only a fraction of the domains in the current path change their orientation in response to pulses.

To determine the changes in the orientation of the Néel vector induced by current pulses we now analyze data from the σ and π polarization data separately. Figure 2.11(a) shows the σ and π polarization data that are used to form Image III in Fig. 2.10(a). The σ polarization is in the film plane and thus provides sensitivity to changes in the projection of the Néel vector in this plane, while the π polarization has both in and out of the film plane projections. In these images, bright contrast in a region indicates that the AFM order is mostly aligned perpendicular to the polarization direction, whereas dark contrast indicates that the AFM order aligns mostly parallel to the polarization direction. Although the contrast associated with the switched AFM domain is visible in both polarization images, the contrast is much stronger in the π -polarization images.

Moreover, dark contrast of the AFM switched region in the π -polarization image indicates that the projection of the Néel vector on the π polarization has changed significantly in response to the current pulse.

We now separately analyze the polarization dependence of the difference images in Fig. 2.10(b). The results are shown in Fig. 2.11(b). The top row of images (red bordered images) shows the σ differences images that highlight changes to the in-plane AFM order. The lower row of blue bordered images show the π difference images that are sensitive to the projection on the π polarization direction. All six differences images are on the same color scale to be able to compare the changes in contrast. The contrast change in π -polarization images is approximately twice as large as that of the σ -polarization images. This indicates that the projection of the Néel vector on the π polarization changes more than its projection on the σ polarization direction.

We further studied the effect of higher currents. We repeated the same pulse sequences, as in Fig. 2.10, but this time with a 50% higher current pulse amplitude, 6 mA. Figure 2.12(a) shows XMLD images taken before and after applying the current pulses. Starting from State A (Fig. 2.10(a)II) and applying 20 current pulses of B, then A and then B again. Figure 2.12(b) shows the differences between images, again to highlight the change in domain structure associated with the current pulses. Figure 2.12(b) shows the differences between the images, again to highlight the change in domain structure associated with the current pulses.

Besides the fact that the reversible domain reorientation is still observable, the light blue dot in Fig. 2.12(b), at this larger current there are additional changes. In difference panels (III-II) and (IV-III) blue and red regions represent new AFM domains switched by the application of the pulse A and that most of them are irreversible switches. In contrast to Fig. 2.10, where almost all the switched AFM domains were in the current path, Fig. 2.12(b) shows switched regions outside of the current path. In fact, the blue region on panel (III-II) is situated well outside the region that experiences the current.

Previous work on current-induced switching in α -Fe₂O₃ assumes that the Néel vector lies and

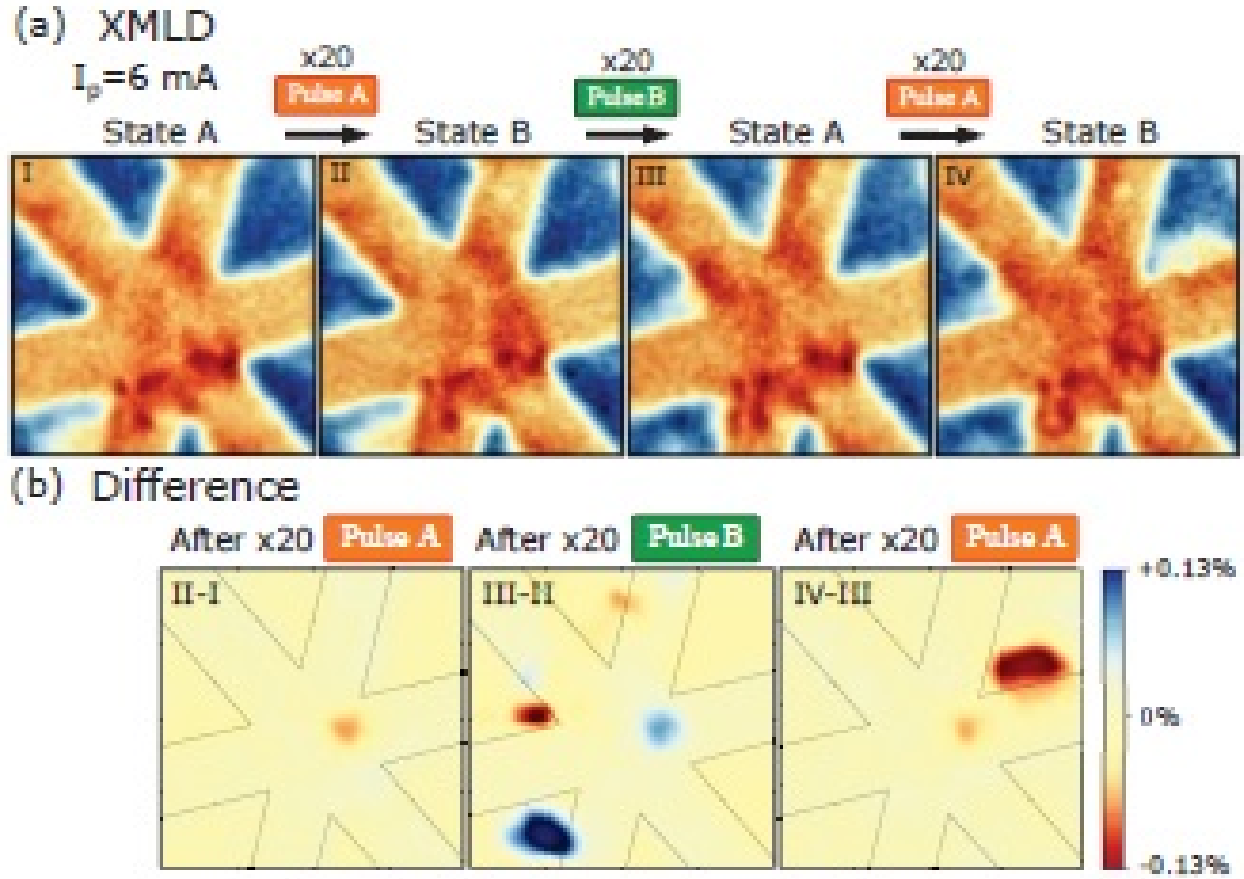


Figure 2.12: AFM domain response to larger amplitude current pulses. (a) Image I shows the initial sample state which is State A. Followed by images II, III and IV taken after $20 \times B$ pulses, $20 \times A$ pulses and $20 \times B$ pulses respectively. In each case the current amplitude was 6 mA. (b) Differences of XMLD images in panel (a) highlight the pulse induced changes, with an expanded color scale, the same as the that of Fig. 2.10(b).

rotates completely in the film [29, 49]. However, our sample characterization and polarization dependent analysis show that this is not the case. The fact that the contrast of the AFM domains changes in the π projection images after a 180° rotation combined with the fact that we are observing more contrast in the π polarization images indicate that Néel vector has an equilibrium out-of-plane component. Our results show that the current-induced switching is between easy axes that are canted out of the film plane as indicated in Fig. 2.13. The canting angle of the Néel vector can be determined by doing the rotation experiment, with more polarizations and more angles. Details of this rotation experiment is discussed in section 2.2.7. The data from this study allows us to put a lower limit of 30° on the canting angle, measured from the sample plane. The mechanism for the canting is currently unclear, though interfacial effects resulting from the Pt layer may play a role.

Now in the light of these observations, we turn to the question of the potential switching mechanisms. Two main mechanisms were used to explain the observed magnetoresistance, spin-orbit-torques (SOT) and thermally induced magnetostriction. For the spin-orbit-torque case, the spin accumulation generated in the Pt acts as an effective magnetic field and exerts a damping-like SOT on the Néel order to align it with the current direction. Whereas for thermally induced magnetostriction, compressive normal stresses induced by Joule heating changes the anisotropy energy through magnetostriction, thus, also favoring alignment of the Néel vector with the applied current. In easy-plane antiferromagnets with large magnetostrictive coefficients such as α - Fe_2O_3 and NiO, this can outweigh damping-like torques [40, 49]. Our finite element simulations show that both the current density levels ($\sim 2 \times 10^8 \text{ A/cm}^2$) and thermally induced compressive normal stresses are above their respective required thresholds ($\sim 50 \text{ MPa}$) to induce switching, which is discussed in more detail in section 2.2.10. This suggests that both mechanisms potentially contribute to the switching. The fact that we can see changes in the Néel vector outside of the current path demonstrates that thermally induced magnetostriction alone is enough to produce switching, since there cannot be any SOT effects where there is no current. However, we

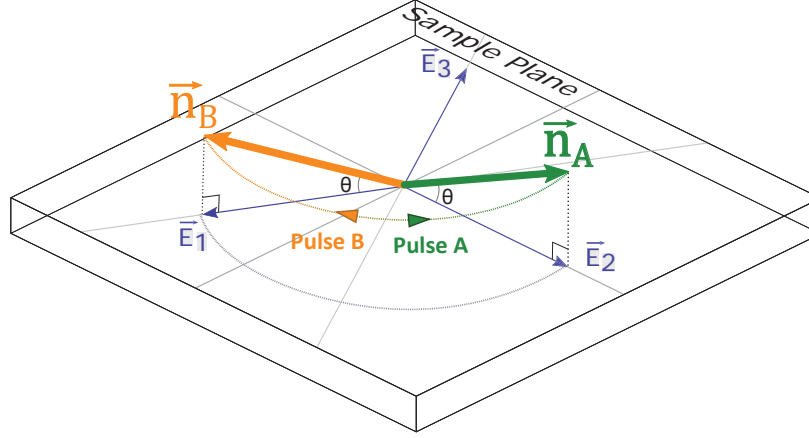


Figure 2.13: Schematic of the switching of the Néel vector between easy axis directions that cant out of the film plane, which is consistent with both the XMLD-PEEM results and the Hall response. \vec{n}_A and \vec{n}_B are the orientations of the Néel vector after Pulse A and Pulse B respectively. The dotted lines with arrows shows the switching direction of the Néel vector in response to the pulses. These arrows associated with Pulse A and Pulse B correspond to blue and red changes, respectively, in the difference images in Fig. 2.10(b) and Fig 2.12(b).

also see all of the reversible domain changes in the current flow path, i.e. where SOT is present.

2.2.6 SPIN CONTRAST FROM XMLD IMAGES

This section discusses the x-ray contrast mechanisms and provide the methods we used to create the XMLD images Figures 2.10 and 2.12. Contrast associated with AFM domains can be obtained from the absorption signals associated with two perpendicular linear polarizations of x-rays resonant with the L_{2a} and L_{2b} Fe edges [57, 58]. The XMLD images in Fig. 2(a) are the result of analyzing a total of six images taken at pre- L_2 , L_{2a} and L_{2b} edges of Fe (718, 721.4 and 723 eV, respectively), with two perpendicular polarizations, σ and π (shown in Fig. 1(a)). These six images are shown in a grid in Fig. 2.14 with their x-ray energy labels.

We start the image processing by normalizing σ - L_{2a} and σ - L_{2b} images to the σ -pre- L_2 image and the π - L_{2a} and π - L_{2b} images to the π -pre- L_2 image to remove any contrast that does not originate from spin structure. Then for each polarization, we take the asymmetry between the L_{2a} and L_{2b} edges and create images showing the magnetic contrast for the two polarization

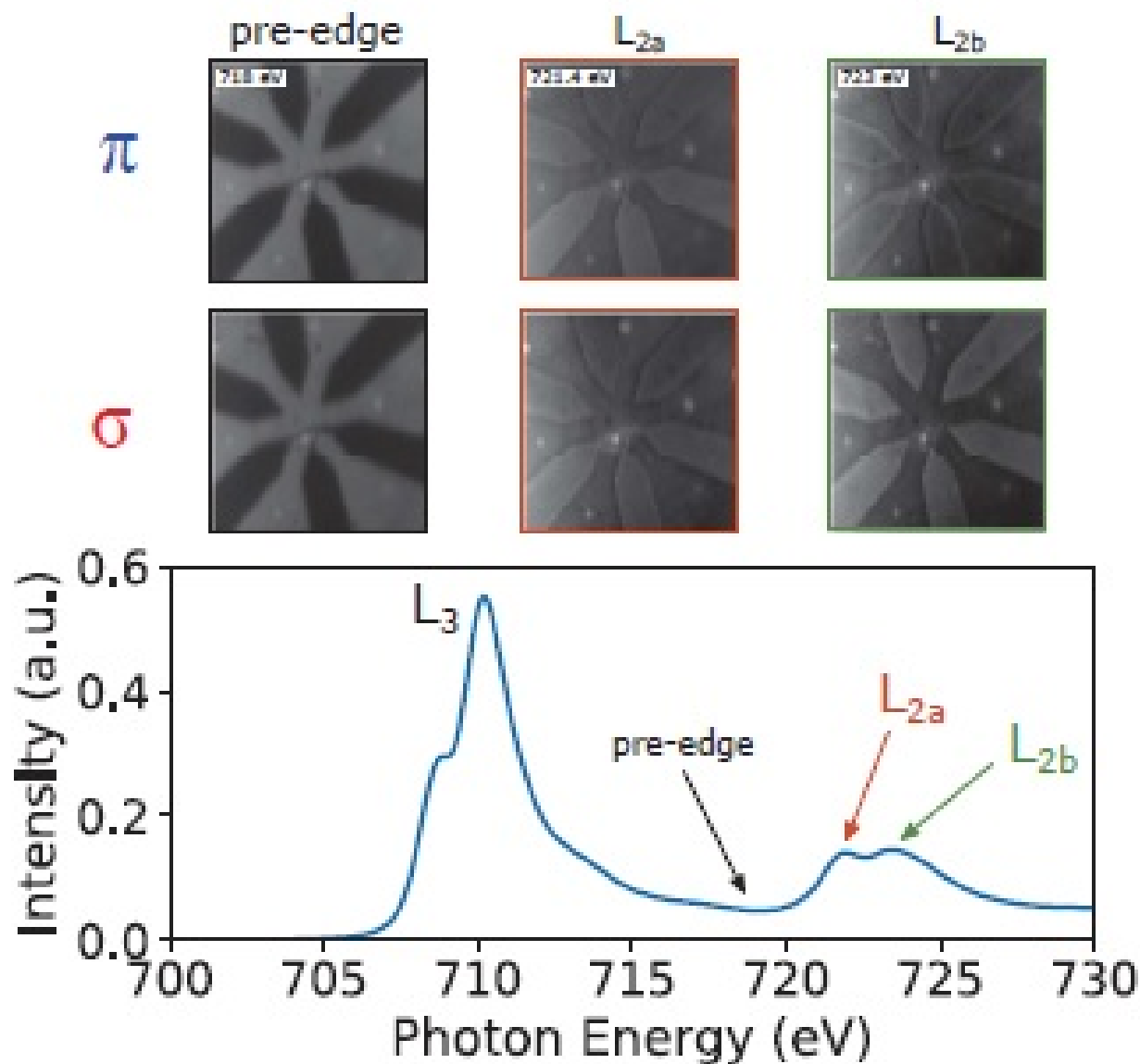


Figure 2.14: Lower panel: Absorption spectra of α -Fe₂O₃ showing the photo-electron intensity versus x-ray energy. Arrows indicate pre-L₂, L_{2a} and L_{2b} Fe edges at 718, 721.4 and 723 eV, respectively. Top panel table shows PEEM images obtained at the different photon energies (columns) and polarizations (rows).

Starting with 6 Images: 3 Energies (Pre- L_2 , L_{2a} , L_{2b}) \times 2 Polarizations (σ and π)

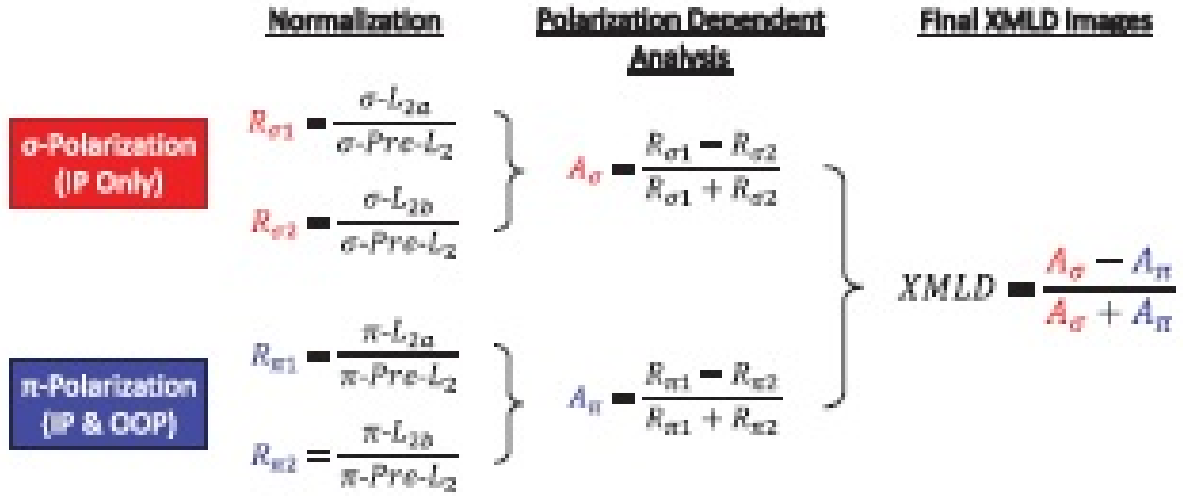


Figure 2.15: A schematic of the steps for creating the final XMLD images from images taken with polarizations σ and π and at energies -pre- L_2 , L_{2a} and L_{2b} .

directions, σ and π as in Fig. 2.2(a). The asymmetry between the two different polarizations images is used to create the XMLD images show in Fig. 2(a). These steps are summarized in Fig. 2.15.

The magnetic origin of XMLD spectra in α -Fe₂O₃ has been established in temperature dependent studies of single crystals. Dzyaloshinskii-Moriya interactions lead to a canting of spins in the (0001) easy plane and a weak in-plane ferromagnetic magnetic moment. The induced moment vanishes below around 260 K, the Morin temperature, T_M , in bulk α -Fe₂O₃ and the easy direction becomes [0001] [54]. By decreasing the temperature below this transition, spins can be rotated to the crystal c-axis and XMLD spectroscopy as a function of temperature have confirmed the magnetic origin of the dichroism features at the Fe $L_{2,3}$ edges [57, 59]. Although for thin films this transition is most likely suppressed [54].

2.2.7 SPINS CANTED OUT-OF-PLANE EQUILIBRIUM STATE

This section provide details on how we come to the conclusion of the Néel vector having an out-of-plane tilt. In order to corroborate the existence of this out-of-plane component of the Néel vector, we imaged an unpatterned Pt/ α -Fe₂O₃ sample at different azimuthal angles: $\phi=0^\circ$, -96° and -191° . As the sample rotates about its normal, the contrast of an AFM domain changes because the XMLD signal is proportional to the cosine squared of the angle between the Néel vector and the polarization vector, i.e. $S_{\text{XMLD}} \sim (\hat{n} \cdot \hat{p})^2 = \cos^2 \alpha$. If the assumption of the Néel vector lying completely in the film plane was true, after a 180° rotation its projection along any x-ray polarization direction would be the same as the initial one. However, for polarizations with an out-of-plane component, the contrast does not came back to the original value after a $\sim 180^\circ$ rotation.

Analyzing the domain in the middle of the red square in Fig. 2.16 for all sample rotation angles and both σ and π x-ray polarizations, reveals this behavior clearly. For polarization π after a 191° rotation, the domain contrast flips, changes from dark to light, whereas the same domain for polarization σ , flips its contrast after a 96° rotation (dark to light) and reverts back its original contrast level after 191° rotation (dark to light to back to dark).

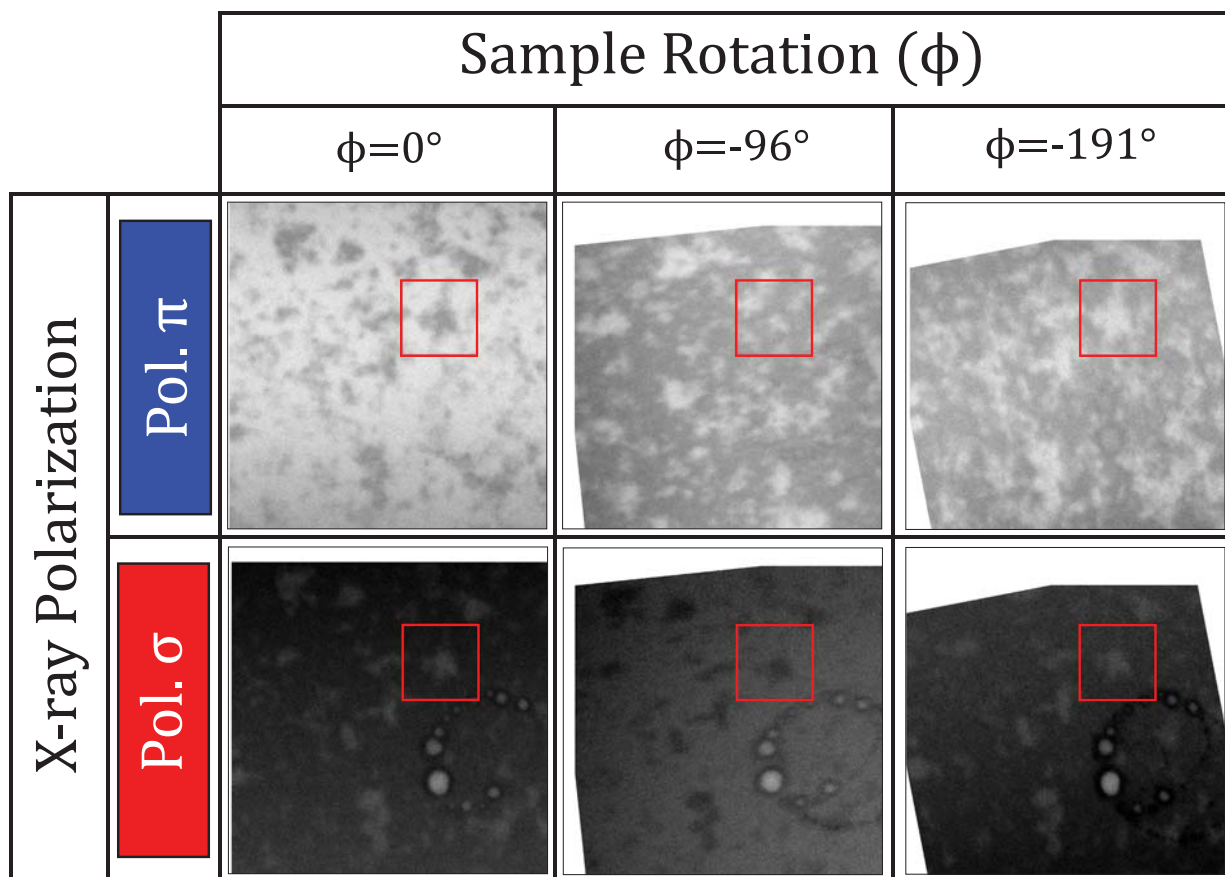
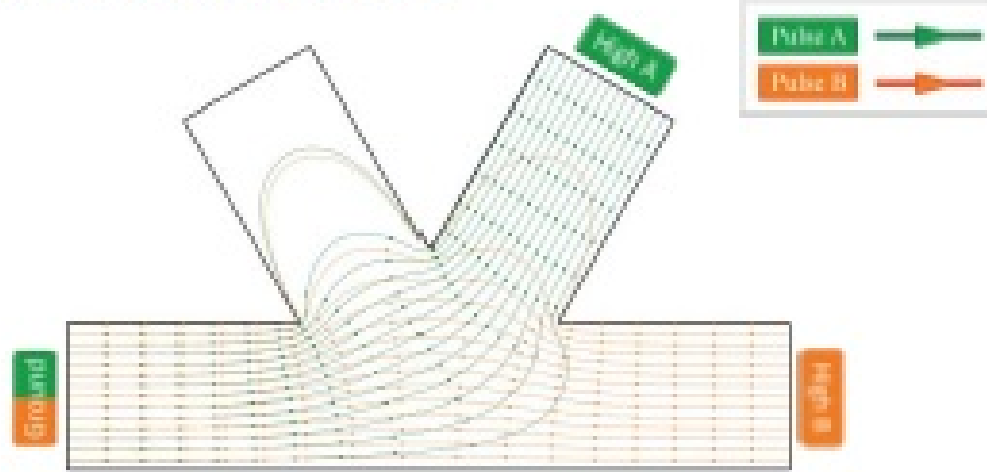


Figure 2.16: Polarization σ and polarization π projections as a function of in-plane sample rotation angle ϕ . The images are taken from an unpatterned Pt(2)/ α -Fe₂O₃(30) sample that was grown under the same conditions as that of the patterned samples studied. All images were aligned with respect to each other and use the same color scale. The red square is there to highlight the same particular sample region in all six images.

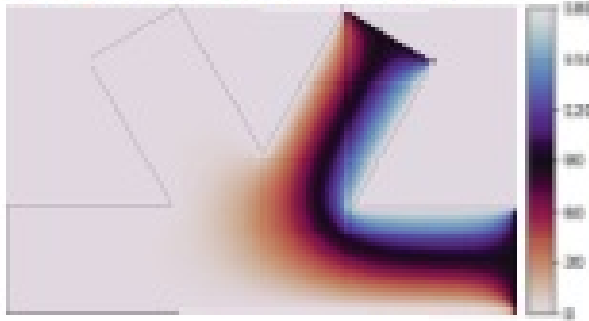
2.2.8 CURRENT DISTRIBUTIONS

We have conducted finite element simulations to characterize the current and temperature distributions in the sample. Figure 2.17(a) shows current distributions for pulse A and B, to highlight the regions in which the current flow direction changes between the two pulses. The bottom two leads are omitted because they were electrically disconnected. Since deterministic switching requires that the current directions be different for consecutive pulses, it is expected that AFM domain changes occur only where streamlines intersect each other at large angles. Considering the 6-fold symmetry of the easy axes, these angles should vary between 60° and 120° . Figure 2.17(b) quantifies the angle difference between two pulse configurations, where most contrast occurs on the right side of the Hall cross. But this figure does not capture the effect of both current amplitudes properly. To emphasize the role of current amplitude as well as the difference in angle, Fig. 2.17(c) shows the norm of the cross product of current densities ($|\vec{J}_A \times \vec{J}_B|$). Since the norm of the cross product is the multiplication of the amplitudes and the sine of the angle in between the current densities, it accurately highlights the regions where we should expect the switching. Both of the AFM domain changes in Fig. 2(b) occur in the high contrast regions of this figure. The current distributions were computed using the AC/DC module of COMSOL Multiphysics software.

a) Current Distributions for Pulse A & B



b) Angle Between Pulse A & B



c) Cross Product of Pulse A & B

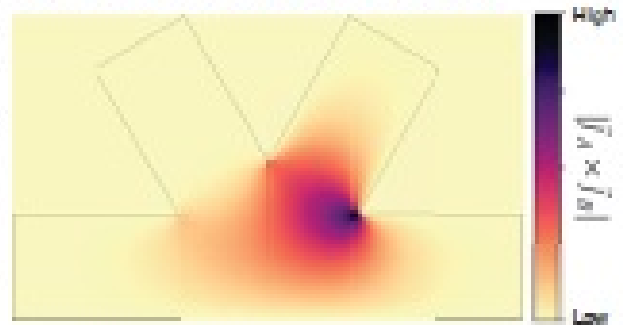


Figure 2.17: (a) Current distributions for pulse A and pulse B configurations. Labels at the edge of leads show where each pulse originates and terminates. The flux of the streamlines is proportional to the magnitude of the current density. (b) Angle between current distributions for pulse A and pulse B at each point of the Hall cross. (c) Norm of cross product of current distributions A and B.

2.2.9 TEMPERATURE PROFILES

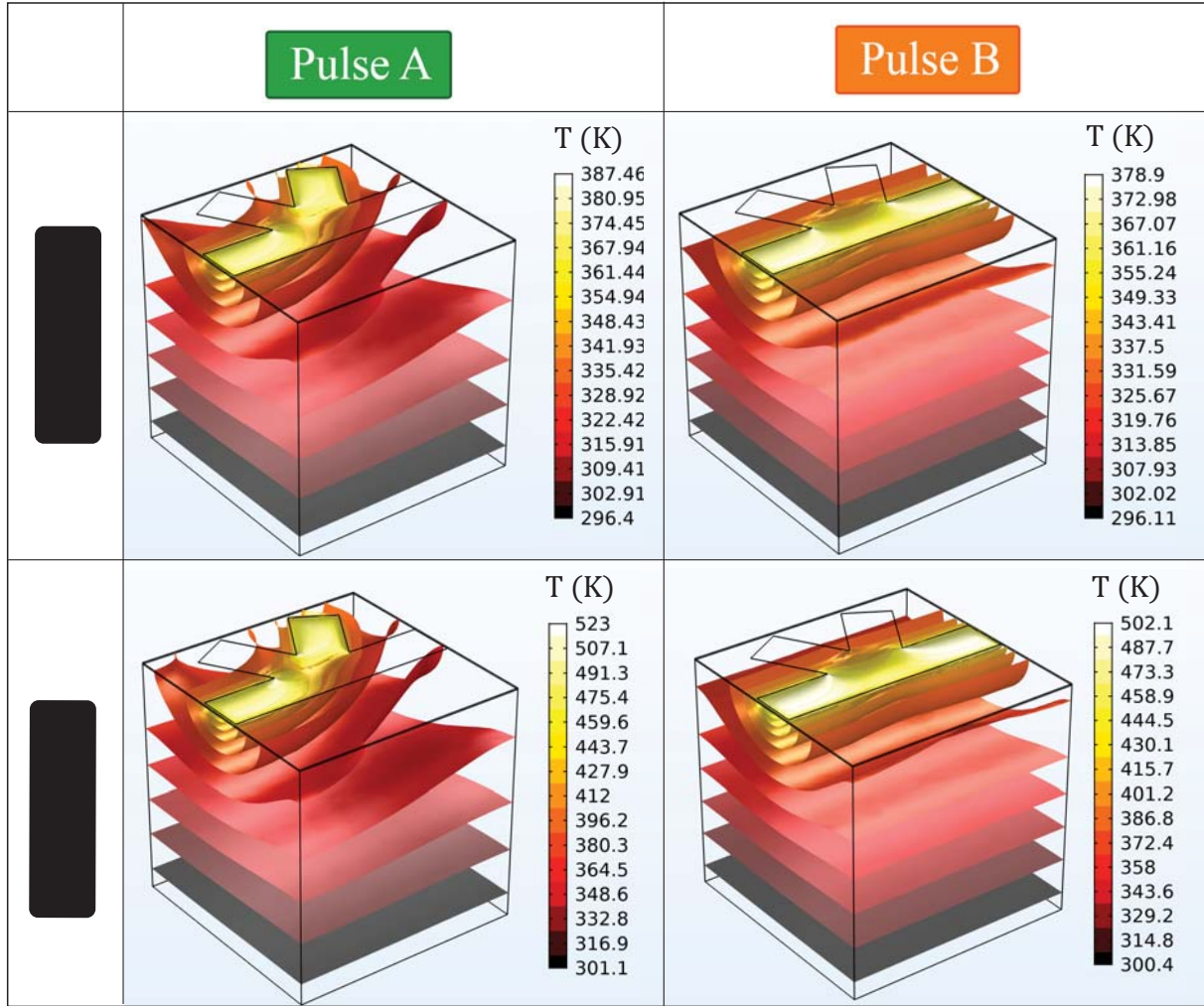


Figure 2.18: Finite element simulations for temperature distribution in both pulse configurations, for both pulse amplitudes. The block size is $5 \times 5 \times 5 \text{ } \mu\text{m}^3$. Two bottom leads of the Hall cross are omitted because they were electrically disconnected.

Figure 2.18 shows the temperature profile in the region of interest in the steady state limit, calculated using the Joule heating module of COMSOL Multiphysics. The stack consists, from top to bottom, of 2 nm of Pt, 30 nm of $\alpha\text{-Fe}_2\text{O}_3$ and $5 \text{ } \mu\text{m}$ of Al_2O_3 . Simulations are done for both A and B pulse configurations and for two pulse amplitudes, 4 mA and 6 mA, corresponding to the pulse amplitudes used our experiments. The corresponding current densities are 2×10^8

A/cm^2 and $3 \times 10^8 \text{ A}/\text{cm}^2$. The platinum resistivity at room temperature was calculated from the experimentally measured resistance of the Hall cross. An ambient temperature of 293 K was used as the boundary condition at the bottom surface of the sapphire block. Heat transfer by convection and radiation is negligible and ignored. We verified the steady-state assumption by simulating the transient response which showed that thermal equilibrium is reached in the order of nanoseconds. The appreciable increase in temperature under the Pt leads and laterally across all of the Fe_2O_3 layer supports the picture that the switching is thermally activated. In other words, that it is easier to reorient the Néel vector in hotter regions.

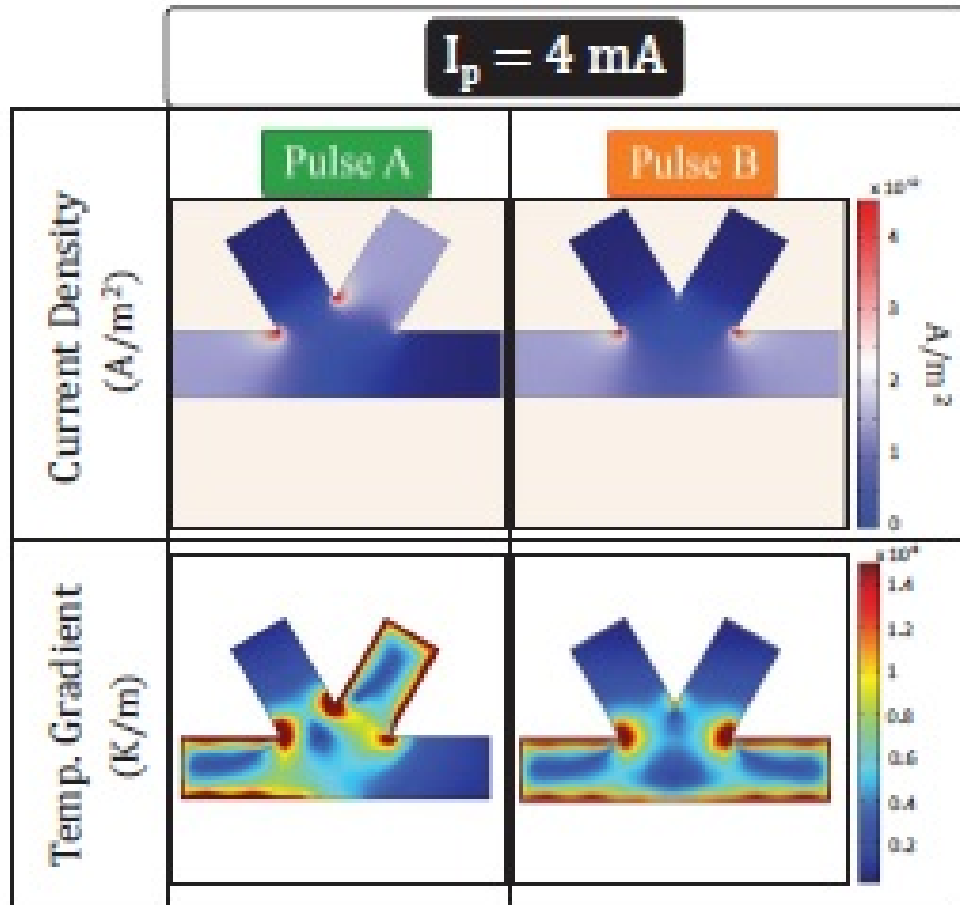


Figure 2.19: (a) Current density amplitude and (b) temperature gradient profiles across the leads, for pulse A and pulse B configurations.

Similarly Figure 2.19 shows the amplitude of current density and resulting temperature gradient for 4 mA pulses in both pulse configurations. As expected current density amplitudes peak around corners and most of the heating occurs around there. Consequently highest amount of temperature gradients are close to the corners too. Temperature gradients are important because they directly affect the stress-strain distributions on the sample, which we will look at in the next section.

2.2.10 STRESS DISTRIBUTIONS

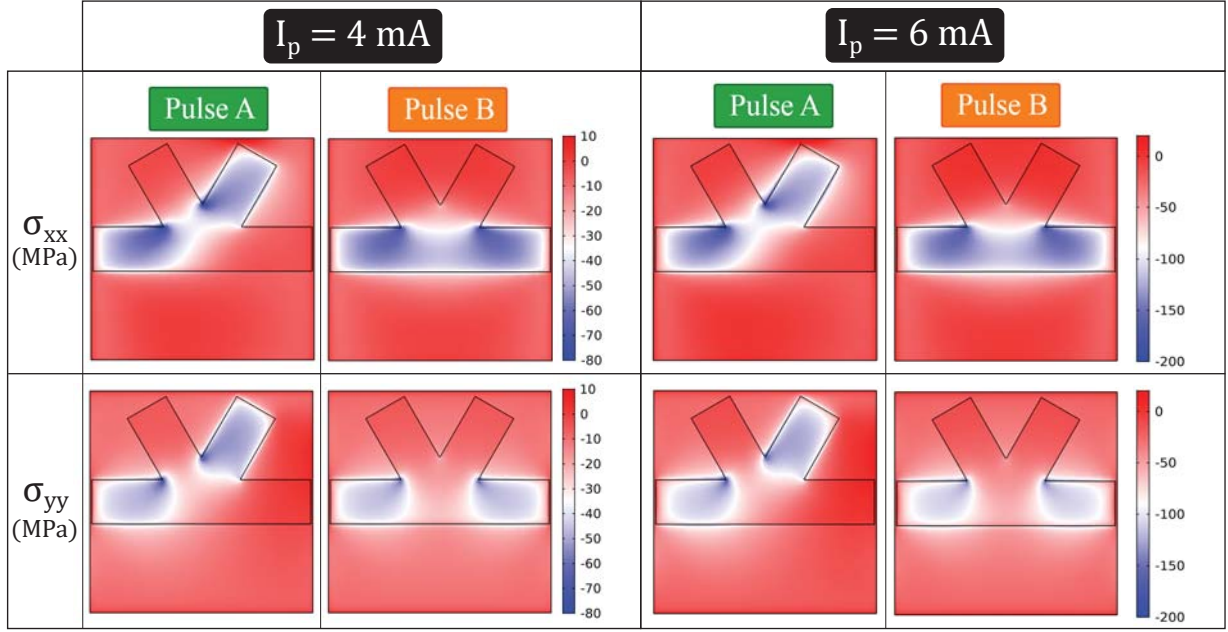


Figure 2.20: Finite element simulations for stress distributions σ_{xx} and σ_{yy} in both pulse configurations, for both pulse amplitudes.

An increase in temperature and temperature gradients naturally leads to development of thermal stresses across the sample, which in turn can change magneto-elastic energies. In Fig. 2.20, we show σ_{xx} and σ_{yy} components of the stress tensor for pulse configurations A and B and for both pulse amplitudes. In all of the configurations active current leads are under compressive stresses. The nominal amplitude of the compressive stresses σ_{xx} and σ_{yy} are approximately 60 MPa for $I_p=4$ mA and 150 MPa for $I_p=6$ mA. In Ref. [49], it was shown that these compressive stresses are more than sufficient to induce magnetic switching. The material properties that were used in the simulations are listed in Table 2.1.

Material	Young's Modulus	Thermal Conductivity	Heat Capacity	Thermal Exp. Coeff.
	GPa	W/(m· K)	J/(kg· K)	K ⁻¹
Al ₂ O ₃	345	34	780	5.6×10^{-5}
α -Fe ₂ O ₃	225	4	650	6.3×10^{-5}
Pt	168	72	133	8.8×10^{-6}

Table 2.1: Material properties used in COMSOL simulations at 293 K.

2.2.11 CONCLUSION

To conclude, we directly and for the first time imaged repeatable current-induced switching of antiferromagnetic moments in α -Fe₂O₃/Pt bilayers with XMLD-PEEM. We observed that only a fraction of the domains reorient, consistent with electrical measurements—which shows that the Hall effect response is less than that expected for complete switching in the Hall cross region. We further identified two types of response that tend to occur in different regions: reversible switches in the Hall cross area and irreversible switches in and outside the Hall cross. While both SOT and thermally induced magnetostriction potentially contribute to switching, our experiments with high current density pulses demonstrate that thermal effects alone can induce changes in the Néel order, by showing there are irreversible changes to the AFM domain structure outside the electrical path. To gain further insights into the switching mechanisms, the impacts of SOT and thermal effects on AFM order needs to be separated, such as by electrically (but not thermally) isolating the metal layers from the α -Fe₂O₃, or using light metals (e.g. Al) instead of Pt, which will be the topics of future studies.

2.3 IMAGING EXPERIMENTS ON NiO

This section will cover some of the imaging experiments that we conducted on antiferromagnetic NiO. After analyzing the results of our experiments on α -Fe₂O₃/Pt and concluding that

magnetoelastic effects are playing an important role in switching, we wanted to study this mechanism further. One natural path to take is inducing Néel vector reorientation purely from magnetoelastic effects, which can be done by depositing NiO on a piezoelectric substrate.

The PMN-PT (also known as lead magnesium niobate - lead titanate) is a piezoelectric crystal that is known for its extremely high piezoelectric coefficient and high electromechanical coupling coefficient [60]. By applying a moderate amount of voltage across this type of substrate, one can get a high amount of mechanical strain. Naturally some of this strain will be applied to the adjacent layers depending on the coupling quality of the interface. But it is not trivial to grow high quality crystalline materials on every substrate, mainly due to lattice mismatch between crystals. So with this goal in mind, we have looked at 4 different stacks of NiO to characterize the effects of the substrate on the antiferromagnetic domains:

- PMN-PT(001)/NiO(21)/Pt(2)
- PMN-PT(111)/NiO(21)/Pt(2)
- MgO(001)/NiO(21)/Pt(2)
- MgO(111)/NiO(21)/Pt(2)

where samples on MgO substrates can be considered control samples of PMN-PT for better comparison of substrate type and orientation. Unfortunately only in one of the substrates XMRD contrast was strong enough to image the antiferromagnetic domains, which was MgO(001). Therefore in the following sections I will focus on our studies of imaging equilibrium domain distribution on MgO(001)/NiO(21)/Pt(2) samples.

2.3.1 SAMPLE CHARACTERISTICS

NiO samples deposited on Mg(001) substrates by reactive magnetron sputtering in Yang Group at the Ohio State University. Substrates were annealed for an hour at 600 °C inside the deposition chamber before deposition and subsequently deposited from NiO target using 100 Watts RF

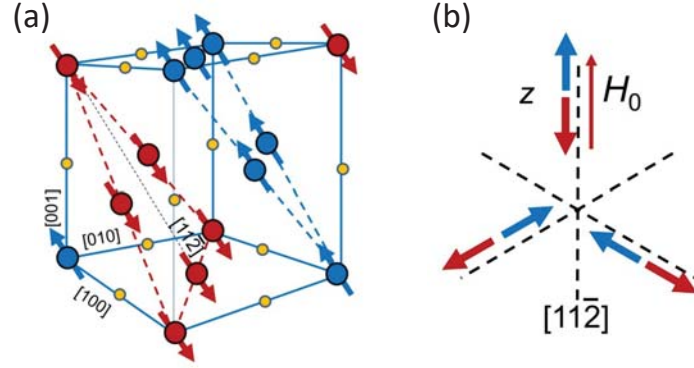


Figure 2.21: (a) FCC crystal structure of NiO. Ni (red and blue) moments are along the confined to the $\{111\}$ easy-planes and along the easy axis $\langle 11\bar{2} \rangle$. Because of the cubic symmetry of the crystal there are four equivalent $\{111\}$ planes and 3 equivalent $\langle 11\bar{2} \rangle$ directions. (b) 3 equivalent $\langle 11\bar{2} \rangle$ directions within the easy plane. Figure is taken from [61]

power in presence of 3 mTorr gas pressure (consisting of 90% Argon and 10% Oxygen). After that platinum layer is deposited at 150 °C without breaking the vacuum.

NiO is a collinear antiferromagnet with a Néel temperature of $T_N = 523$ K. It has an easy plane of $\{111\}$ and within that easy plane it has an easy axis in the $\langle 11\bar{2} \rangle$ direction. Below its Néel temperature it forms antiferromagnetic domains with 12 different possible crystallographic orientations in bulk single crystals. There are four equivalent $\{111\}$ direction inside the cubic lattice, and domains that are oriented in these direction are called T-domains. And within each of these planes there are 3 identical $\langle 11\bar{2} \rangle$ directions which are called S-domains, resulting in the total 12 possible domain orientations.

2.3.2 EXPERIMENTAL SETUP

These experiments was done in beamline 24 (BL24) CIRCE in ALBA synchrotron which is a synchrotron light facility located in, Barcelona. BL24 is very similar to ALS PEEM3 beamline, and also provides soft X-rays in the 100–2000 eV energy range. It has high photon energy resolution and intensity, and full polarization control. More details on the beamline capabilities can be found in this reference [62].

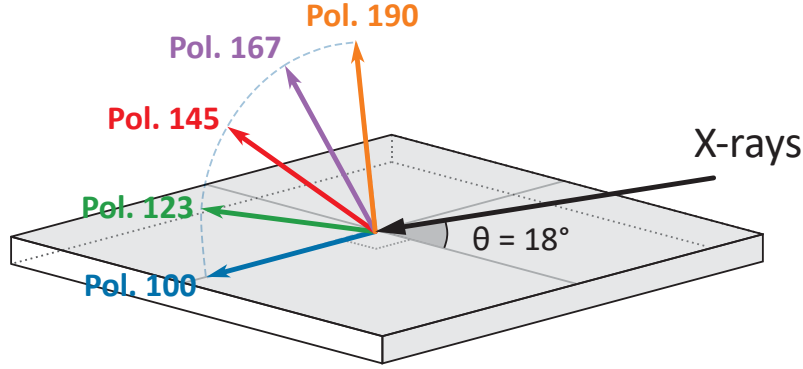


Figure 2.22: Illustration of geometry of incident X-rays and polarizations. Black arrow represents the Poynting vector of incoming x-rays with a grazing angle of 18° . The gray square represents the sample surface. Polarizations 100, 123, 145, 167 and 190 are represented by arrows with different colors as indicated. All polarization lie in a plan that is perpendicular to the plane normal to the Poynting vector.

For correct analysis of the images, the most important aspect of the experimental setup is the angle of incidence of x-rays and the orientation of the polarization. Figure 2.22 shows the angle of incidence of x-rays in grazing configuration which is 18° measured from the sample plane. The arrows in different colors shows the direction of the electric field polarization of the incoming x-rays. Polarizations are continuously adjustable from completely in plane polarization 100 (blue) to polarization 190 (orange) maximally out-of-plane. All five polarization that are used in the experiment lie in the plane that is perpendicular to the Poynting vector of the incoming light. They are evenly distributed and the angle between them is 22.5° , hence their names Pol. 100, Pol. 123, Pol. 145, Pol. 167 and Pol. 190.

2.3.3 IMAGING ANTIFERROMAGNETIC DOMAINS

We have imaged NiO samples with 5 polarizations (from Pol. 100 to Pol. 190) and 3 different in-plane rotation angles $\phi = 0^\circ, 45^\circ, 90^\circ$. Figure 2.23 shows a total of 15 XMLD-PEEM images of the antiferromagnetic domain configurations as a function of polarization (columns) and a sample rotation angle (rows). Each image is approximately $7 \mu\text{m}$ in field of view, and roughly shows the same area on the sample surface, which is indicated by the surface defect close to the middle of

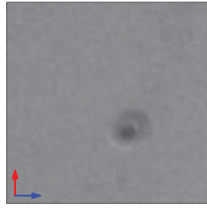
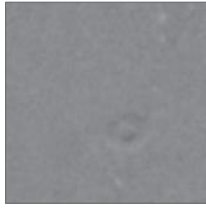
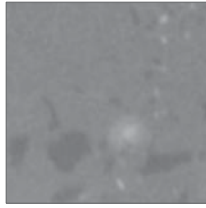
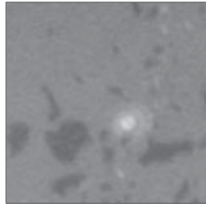
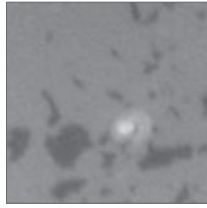
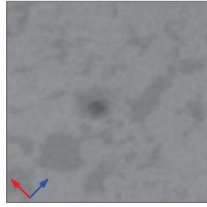
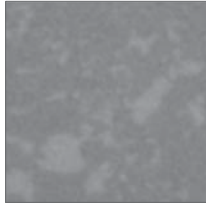
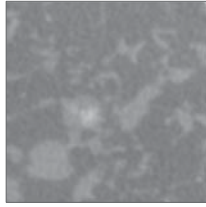
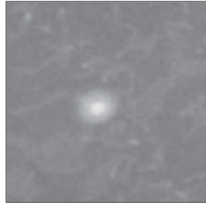
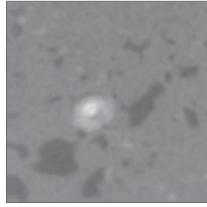
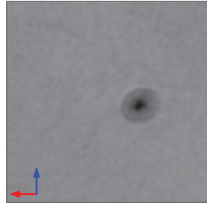
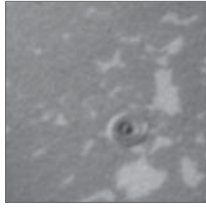
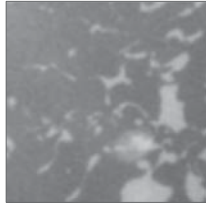
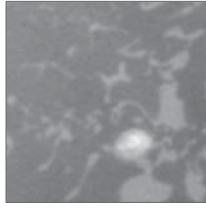
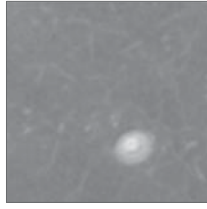
		X-Ray Polarization				
		Pol. 100	Pol. 123	Pol. 145	Pol. 167	Pol. 190
Sample Rotation	$\varphi = 0^\circ$					
	$\varphi = 45^\circ$					
	$\varphi = 90^\circ$					

Figure 2.23: XMLD-PEEM image of NiO sample as a function of sample rotation and x-ray polarization. All images show roughly the same area indicated by the defect on the sample. Blue and red arrows indicate the relative orientation of sample. Field of view is $7 \mu\text{m}$.

each image. Note that even though the area shown is roughly the same, because of the rotation there are slight differences in the exact area, especially between different sample rotation angles. The relative orientation of the images are indicated at the first image of every row by a red and blue arrows.

The first thing to notice when one looks all images that contrast of antiferromagnetic domains change both with sample rotation and x-ray polarization. Across the images, some domains look lighter (or darker) compared to their surroundings and in some images domains are not even visible. XMLD contrast is proportional to the square of the cosine of the angle between Néel vector and the polarization $S_{\text{XMLD}} \sim (\hat{n} \cdot \hat{p})^2$. Since we know the exact angle of polarizations and relative XMLD intensity across images, it is possible to extract orientation of the Néel vector.

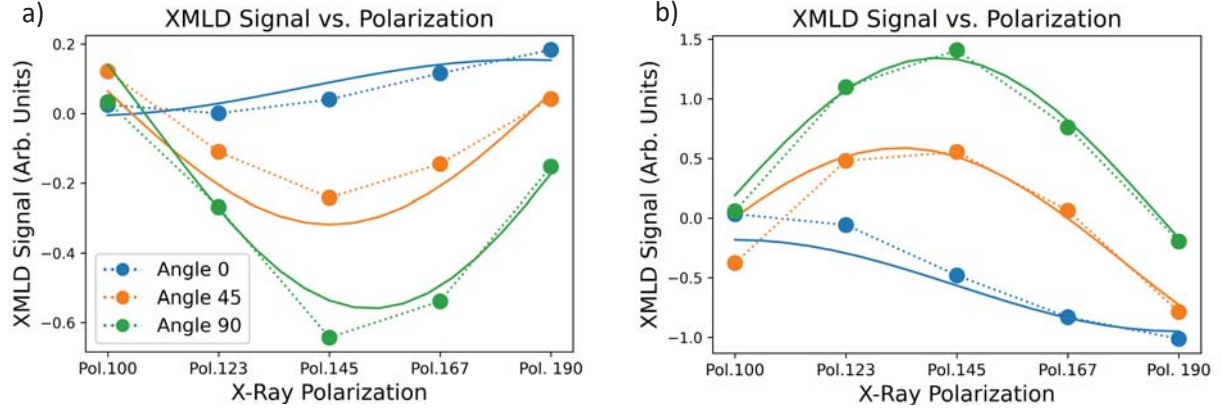


Figure 2.24: Relative XMLD contrast in arbitrary units as a function of x-ray polarization for (a) majority domains and (b) minority domains. The dots are the data points and the lines are the fits with crystal field.

Figure 2.24 shows the relative XMLD contrast for minority (a) and majority (b) domains as a function of x-ray polarization. The dots are the data points and the line represents the fit. However, the simple assumption of XMLD being only proportional to the dot product of Néel vector and polarization was not enough to fit the data. In order to accurately explain XMLD contrast for both type of domains across all images, we needed to add a crystal-field term to the fit function:

$$S_{XMLD} = I_0 + I_1 \cos^2 \alpha + I_2 \cos^2 \gamma \quad (2.1)$$

where I_0 is the base intensity, I_1 is the intensity coming from the magnetic contrast, and α is the angle between Néel vector \hat{n} and x-ray polarization \hat{p} . And the last term is the so-called crystal field component where I_2 is its intensity and γ is the angle between the polarization and [001] direction which is the crystal field. This crystal-field component along [001] can be explained by the strain induced by the epitaxial growth of NiO on MgO(001). The small lattice mismatch generates a distortion in the NiO thin film and causes a compressive strain along the [001] axis resulting in an out-of-plane crystal field which contributes to the XMLD signal. Naturally this contribution is independent of the Néel order inside the domains, as it is not in magnetic origin.

After the inclusion of the crystal field, we extracted the orientation of the the Néel vector which turned out to be 75° out of the plane measured from the sample plane. We only observed two types of domains (majority and minority), and although their out-of-plane component are the same, their in-plane component is exactly anti-parallel to each other. These findings are consistent with the independent study of Schmitt *et al.* on antiferromagnetic domains in NiO [63], where they found Ni moments on $[\pm 5 \pm 5 19]$ directions, different than bulk $[11\bar{2}]$.

2.3.4 CONCLUSION

In conclusion, we imaged antiferromagnetic domains configuration in NiO grown on 4 different substrates, MgO and piezoelectric PMN-PT. Only in MgO(001) substrate the antiferromagnetic domain contrast was large enough to conduct a systematic study. We measured the domain contrast as a function of x-ray polarization and in-plane sample rotation angle. We found that there is a crystal field component to the XMLD and a large out-of-plane component to the Néel vector.

3 | QUANTIFYING SPIN ORBIT TORQUES

USING HARMONIC MEASUREMENTS

3.1 INTRODUCTION

Detecting and manipulating antiferromagnetic order electrically is an important milestone for realizing devices based on AFMs [8, 29, 34, 37, 64–68]. It is known that spin-orbit torques (SOT) are one of the most effective ways to manipulate magnetic order in both ferromagnets (FM) and ferrimagnets [39, 46, 48, 69–74]. Therefore the effect of spin currents on the magnetic order of antiferromagnets (AFMs) is of fundamental interest and can enable new applications. However, their effectiveness is less well explored and quantified particularly for insulating AFMs. Therefore, characterizing the SOT is crucial for understanding and predicting AFM dynamics. A powerful technique to characterize SOT is harmonic Hall measurements [75, 76]. Although this technique has been used extensively in FM/heavy metal (HM) bilayers, harmonic Hall study of SOT in AFMs remains elusive.

We use harmonic Hall measurements to characterize the SOT in α -Fe₂O₃/Pt bilayers. SOT are a result of the spin-Hall effect (SHE) in Pt [18, 77], in which a charge current leads to a spin accumulation at the α -Fe₂O₃ interface. SOT can modify the orientation of the AFM Néel vector and this change can be detected electrically because of spin Hall magnetoresistance (SMR) [20, 21], which is discussed in sections 1.4.1, 1.4.2, 1.5.2. SMR arises from of combination of SHE,

interface scattering, and the inverse SHE [78]. Most importantly for our study, SMR manifests as an anisotropy in the resistivity of the Pt and a Hall signal analogous to the planar Hall in ferromagnets [79]. We first characterize the SMR by 1st harmonic response and then SOT from the 2nd harmonic response.

Then we develop a model of the response that accounts for the magnetic properties of α -Fe₂O₃ including its magnetic anisotropy, exchange and Dzyaloshinskii-Moriya interactions (DMI), and compare the model with the experimental results. By fitting the data from six measurements together (the 1st and 2nd harmonic response with the field rotated in three orthogonal planes), we extract the amplitudes of the damping-like and field-like torques. Out-of-plane field scans are shown to be essential to determining the damping-like component of the torques. Surprisingly and contrary to the case of ferromagnets/heavy metal heterostructures, we find field-like torques to be significantly larger than damping-like torques, which we correlate with the presence of a large imaginary component of the interface spin-mixing conductance. This study demonstrates a direct way of characterizing SOT in AFM/HM heterostructures.

3.2 SAMPLE CHARACTERISTICS AND EXPERIMENTAL SETUP

Figure 3.1(a) shows a schematic of the experimental setup. We perform Hall measurements at 300 K on 30 nm thick epitaxial c-axis oriented α -Fe₂O₃ on Al₂O₃ (0001) substrates capped in-situ with 5 nm thick Pt [29, 76]. The Pt layer is patterned into a $5 \times 15 \mu\text{m}^2$ Hall-cross structure and the Hall voltage is detected with a lock-in amplifier with a 953 Hz AC current of $4 \times 10^9 \text{ A/m}^2$ and $6 \times 10^{10} \text{ A/m}^2$ used for 1st and 2nd harmonic measurements, respectively.

Figure 3.1(b) shows the geometry used in our model. The antiferromagnet's hard axis and DMI vector are represented by the same vector D . The AFM sublattice moment directions are indicated by unit vectors \mathbf{m}_1 and \mathbf{m}_2 . The Néel vector $\mathbf{n} = (\mathbf{m}_1 - \mathbf{m}_2)/2$ lies in the easy plane, which is perpendicular to D , indicated by the red plane. H is the applied magnetic field and

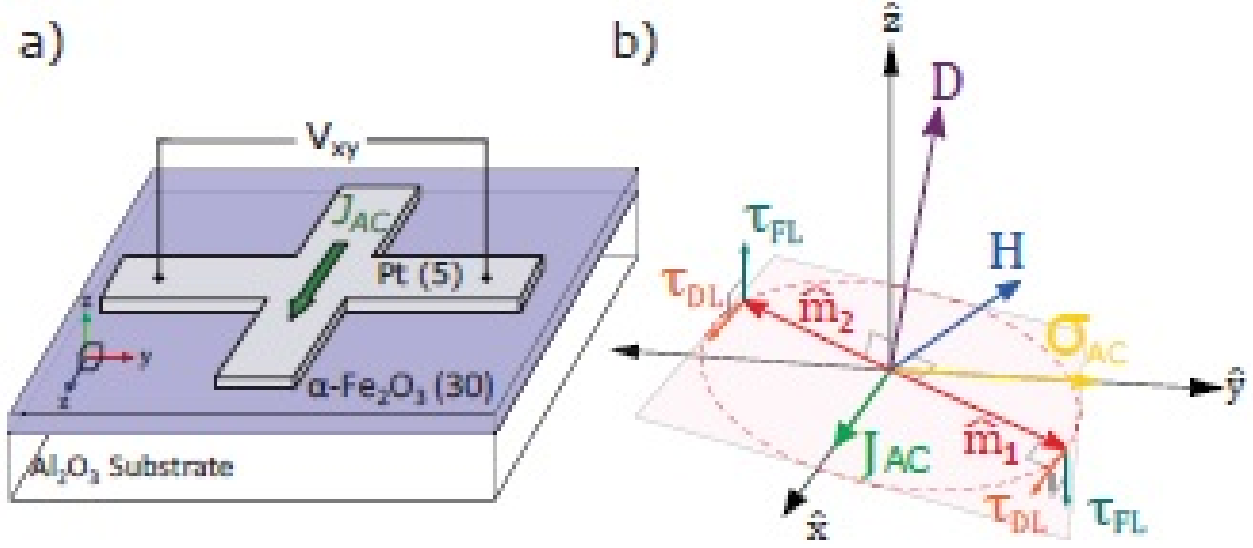


Figure 3.1: a) Transverse measurement configuration showing the Pt Hall cross with 5 μm channel width. An AC current J_{AC} is applied in the \hat{x} -direction, and the transverse voltage V_{xy} is measured with a lock-in amplifier. b) Modeling geometry. D represents both the DMI vector and the hard axis direction that defines the easy plane. \hat{m}_1 and \hat{m}_2 are the sublattice moments and H is the external magnetic field. The spin accumulation σ_{AC} is in the \hat{y} -direction. The resulting spin-orbit torques on the sublattice moments are decomposed into field-like (τ_{FL}) and damping-like components (τ_{DL}).

σ_{AC} is the spin accumulation at the interface caused by J_{AC} via the SHE. The resulting SOT on the sublattice moments are decomposed into field-like (τ_{FL}) and damping-like components (τ_{DL}). Notice we do not constrain D to be parallel to the \hat{z} -axis, as canting of the easy plane in AFMs, due to the strain effects from the substrate has been reported in previous reports [63, 68], as it was discussed in the previous chapter too. As shown at the top of Fig. 3.2, H is rotated in one of the three planes: XY, XZ or YZ, where the current J_{AC} is in the \hat{x} direction.

In an easy plane AFM such as $\alpha\text{-Fe}_2\text{O}_3$, scanning the field in all three principal planes is crucial to find the amplitudes of both components of SOT. This is due to the fact that any component of the SOT (FL or AD) can have its main contribution in any of the three scans, depending on the orientation of the easy plane, see Fig. 3.1(b). In the model geometry, the antiferromagnetic easy plane is slightly tilted but still very close to the film plane XY. In this configuration the field-like torques are major contributor to XY scan response, whereas damping-like torques dominate

the YZ scan response. The differences in the effects of field-like and damping-like torques are discussed in more detail in sections 3.3 and 3.9.

3.3 MODELING THE HARMONIC RESPONSE

Figure 3.2 shows the full angular dependence of Hall signals (blue points), for all three field scans, at $\mu_0 H = 3$ T together with the model fit (red lines). In the in-plane XY scan, both 1st and 2nd harmonic Hall signals follow smooth trigonometric functions. This is expected because spin-Hall magnetoresistance (SMR) and field-like torques are the main contributors in 1st and 2nd XY scan harmonic signals, respectively. On the other hand, for out-of-plane field rotation experiments—XZ and YZ field scans—the angular dependencies do not follow a simple trigonometric function. A comprehensive model is needed in order to explain all six scans, as we discuss below.

In the sample geometry indicated in Fig. 3.1(b), an AC current density $J_{AC}(t) = J_0 \cos \omega t$ generates an oscillating spin accumulation $\sigma_{AC}(t)$ in the \hat{y} direction, which produces SOT on α -Fe₂O₃. The measured Hall voltage V_{xy} arises from the SMR: $V_{xy}(t) = A_x J_0 R_{xy}[\mathbf{n}(J_{AC}, \mathbf{H})] \cos \omega t$, where A_x is area through which the current flows and has the form $R_{xy} \sim n_x n_y$ [22, 78, 80, 81]¹. Since the current-induced torques only result in a slight deviation of \mathbf{n} from its equilibrium orientation, we can expand the SMR as:

$$R_{xy}[\mathbf{n}(J_{AC}, \mathbf{H})] = R_{xy}[\mathbf{n}(0, \mathbf{H})] + J_0 \left(\frac{\partial R_{xy}}{\partial \mathbf{n}} \right) \frac{\partial \mathbf{n}}{\partial J_{AC}} \Big|_{(0, \mathbf{H})} \cos \omega t + h.o., \quad (3.1)$$

where the first term $R_{xy}[\mathbf{n}(0, \mathbf{H})]$ is the SMR, which leads to the first harmonic signal $V_{xy}^{1\omega}(t) = A_x J_0 R_{xy}[\mathbf{n}(0, \mathbf{H})] \cos \omega t$. The second term, which is itself proportional to J_0 , gives rise to the second harmonic response $V_{xy}^{2\omega}(t)$. Therefore, to find the harmonic responses, we need to calculate

¹The contribution to R_{xy} of the form $m_x m_y$ is negligible.

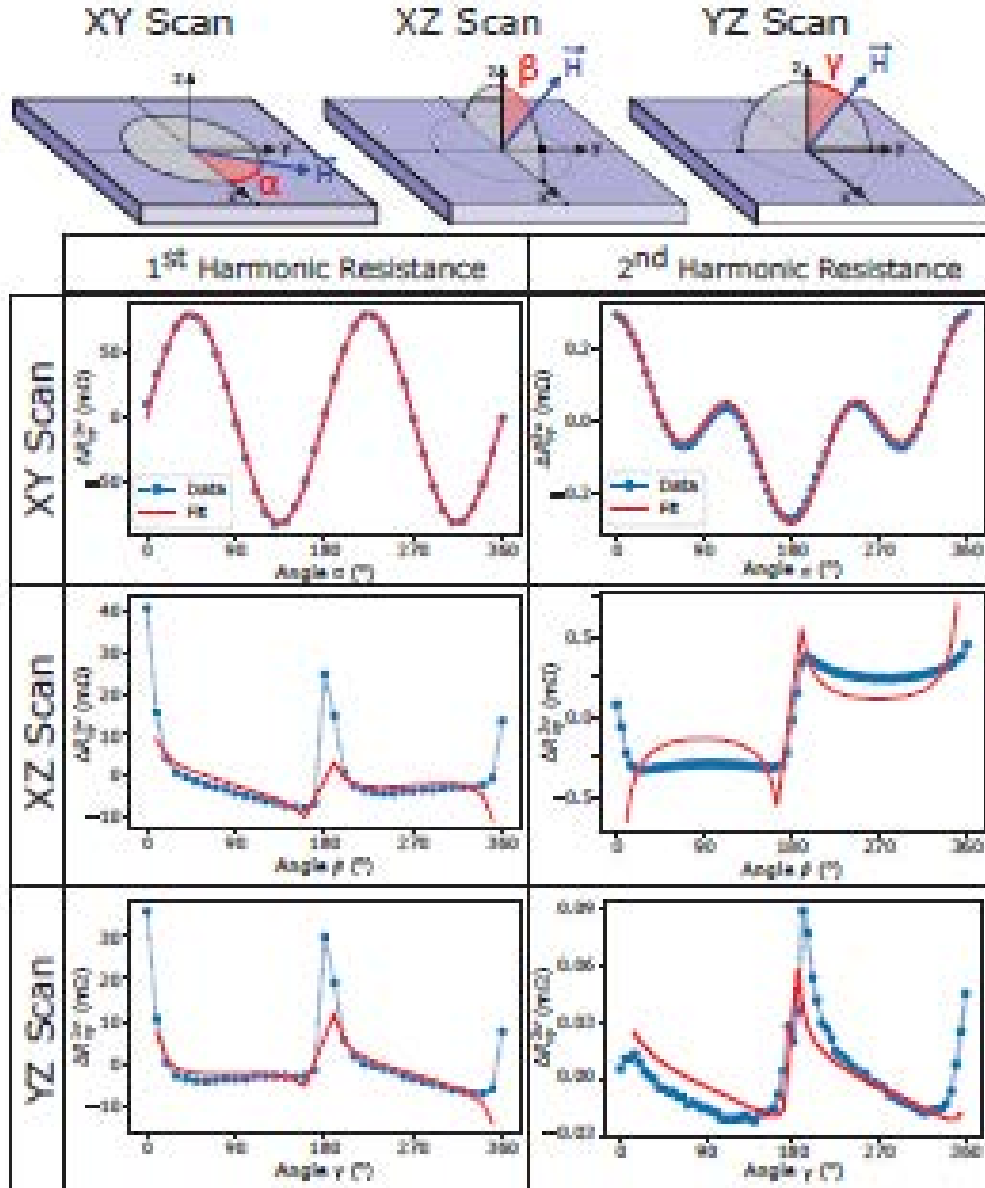


Figure 3.2: Angular dependence of 1st and 2nd harmonic (columns) resistance signals in XY, XZ and YZ scans (rows) at $\mu_0 H = 3$ T. The current amplitudes are 100 μA and 1.5 mA in the 1st and 2nd harmonic measurements, respectively. The blue dots are the data points whereas, the red line is the fit resulting from the model. The geometry of magnetic field scans in the 3 principal planes (XY, XZ and YZ scans) and the definition of the angles α , β and γ are shown at the top. The magnitude of longitudinal SMR is approximately 0.02% and it is consistent with studies on similar AFM/HM systems [21, 31]

$\mathbf{n}(\mathbf{0}, \mathbf{H})$. $\partial \mathbf{n} / \partial J_{AC}$ is determined by the dynamics of the Néel vector and hence by the dynamics of sublattice magnetic moments, \mathbf{m}_1 and \mathbf{m}_2 .

In the macrospin approximation, the free energy density (in field dimensions of Tesla) can be expressed as:

$$\begin{aligned} \frac{\epsilon}{\hbar\gamma} = & H_{\text{ex}} \mathbf{m}_1 \cdot \mathbf{m}_2 + H_K [(\mathbf{e}_h \cdot \mathbf{m}_1)^2 + (\mathbf{e}_h \cdot \mathbf{m}_2)^2] \\ & - H_D \mathbf{e}_D \cdot (\mathbf{m}_1 \times \mathbf{m}_2) - \mathbf{H} \cdot (\mathbf{m}_1 + \mathbf{m}_2), \end{aligned} \quad (3.2)$$

where γ is the gyromagnetic ratio. \mathbf{e}_h and \mathbf{e}_D are unit vectors in the directions of the hard axis anisotropy and DMI respectively. H_{ex} , H_K and H_D are the effective fields associated with the exchange interaction, the hard axis anisotropy and the DMI, respectively. Here we have ignored the in-plane easy axis anisotropy because it is much weaker than H_K and H_D [81]. This simplification, however, becomes invalid when the in-plane projection of \mathbf{H} is insufficient to maintain a single domain state [76] (e.g., when \mathbf{H} is nearly perpendicular to the easy plane). The dynamics of the sublattice magnetic moments are described by the coupled Landau-Lifshitz-Gilbert-Slonczewski equations

$$\begin{aligned} \frac{d\mathbf{m}_{1,2}}{dt} = & \gamma \mathbf{H}_{1,2}^{\text{eff}} \times \mathbf{m}_{1,2} + \alpha_0 \mathbf{m}_{1,2} \times \frac{d\mathbf{m}_{1,2}}{dt} \\ & + \gamma [H_{\text{Oe}}(J_{AC}) + H_{\text{FL}}(J_{AC})] \boldsymbol{\sigma}_{AC} \times \mathbf{m}_{1,2} \\ & + \gamma H_{\text{DL}}(J_{AC}) \mathbf{m}_{1,2} \times [\mathbf{m}_{1,2} \times \boldsymbol{\sigma}_{AC}], \end{aligned} \quad (3.3)$$

where $\mathbf{H}_{1,2}^{\text{eff}} = -\delta\epsilon/(\hbar\gamma\delta\mathbf{m}_{1,2})$ is the effective field acting on $\mathbf{m}_{1,2}$, α_0 is the Gilbert damping constant, $H_{\text{Oe}}(J_{AC}) = \frac{1}{2}\mu_0 A_x J_{AC} t_{\text{Pt}}$ is the Oersted field and t_{Pt} the thickness of the Pt film. $\boldsymbol{\sigma}_{AC}$ is the direction of spin accumulation (here along \hat{y}), and $H_{\text{FL}}(J_{AC})$ and $H_{\text{DL}}(J_{AC})$ are the strengths of the field-like and damping-like torques, respectively.

All the three fields generated by the current are linearly proportional to J_{AC} . In particular, H_{Oe} and H_{FL} satisfy the same symmetry, but we show that Oersted field contribution is much smaller than field-like SOT, using finite-element simulations (see section 3.7). Because the intrinsic frequency of the spin dynamics in α -Fe₂O₃ is many orders of magnitude larger than ω [82], we can treat $\mathbf{m}_{1,2}$ as quasi-static vectors that adiabatically adjust to the AC current, remaining in the instantaneous ground state in the presence of current-induced torques. Under the adiabatic approximation, Eq. (3) can be solved analytically [83], and, if $|\mathbf{m}| = |\mathbf{m}_1 + \mathbf{m}_2| \ll 1$, can be expressed by the Néel vector \mathbf{n} as function of J_{AC} and \mathbf{H} . Finally, by inserting $\mathbf{n}(J_{AC}, \mathbf{H})$ into Eq. (1), we obtain the general solution for the SMR and thus $V_{xy}^{1\omega}$ and $V_{xy}^{2\omega}$. This general solution, however, cannot be recast into a concise form unless we assume that $\mathbf{e}_h \parallel \hat{z}$ and $\mathbf{e}_D \parallel \hat{z}$ i.e. the easy plane coincides with the film plane without tilting. The special solution for vanishing tilt is:

$$R_{xy}^{1\omega} = -\frac{1}{2}R_0 \sin 2\phi_H, \quad (3.4)$$

$$R_{xy}^{2\omega} = R_0 \left[-\frac{\cos 2\phi_H \cos \phi_H}{H \sin \theta_H} (H_{Oe} + H_{FL}) + \frac{2H_{ex}H \cos \theta_H \cos 2\phi_H \sin \phi_H H_{DL}}{2(H_D^2 + 2H_{ex}H_K)H \sin \theta_H + H_D(H^2 + 4H_{ex}H_K + H_D^2)} \right], \quad (3.5)$$

where $\theta_H \in [0, \pi]$ and $\phi_H \in [0, 2\pi]$ are the polar and azimuthal angles of \mathbf{H} , and R_0 is a current-independent constant. In Figure 3.2, we identify these angles as $\theta_H = \pi/2$ and $\phi_H = \alpha$ for the XY scan, $\theta_H = \beta$ (or $2\pi - \beta$) and $\phi_H = 0$ (or $-\pi$) for the XZ scan, and $\theta_H = \gamma$ (or $2\pi - \gamma$) and $\phi_H = \pi/2$ (or $-\pi/2$) for the YZ scan, respectively. To better fit the data in Fig. 3.2, however, we further allow a small tilting of the hard axis but still assume that $\mathbf{e}_D \parallel \mathbf{e}_h$, which yields a complicated expression not shown here. We observe a good agreement with the experiment at a tilt angle of 3° with respect to \hat{z} , which is plotted by the red curves in Fig. 3.2. Since the model assumes $|\mathbf{m}| \ll 1$, our solution breaks down at extremely large fields, which is partially reflected in Fig.

3.3 and discussed later.

The field-like torque and the damping-like torque play very different roles in driving the dynamics of magnetic moments. As illustrated in Fig. 3.1(b), the damping-like torque cants both magnetic moments towards the same in-plane direction, which will subsequently leverage the exchange torque between \mathbf{m}_1 and \mathbf{m}_2 so that the Néel vector \mathbf{n} develops an out-of-plane component. By contrast, the field-like torque acts as an effective field that directly drives the net magnetic moment so that the AC current induces an in-plane rotation of \mathbf{m} . Since $\mathbf{m} \perp \mathbf{n}$ by definition, a direct consequence is that \mathbf{n} undergoes an in-plane oscillation. Correspondingly, in the absence of tilting, damping-like torques vanish in the XY scan ($\theta_H = 90^\circ$), and field-like torques vanish in YZ scan ($\phi_H = 90^\circ$). However, any amount of tilting of the easy plane will prevent this vanishing and both field-like and damping-like torques will have contributions in XY and YZ scans.

Because of the small magnetic moment present in α -Fe₂O₃ above its Morin transition, perpendicular coupling between the Néel vector and the external field is easily achievable at moderate field strengths. The easy plane and the external field direction together are adequate to uniquely set the equilibrium direction of the Néel vector and a $\gtrsim 1$ T in-plane component of the applied field can fully align the Néel vector to overcome any in-plane magnetic anisotropy.

We fit the experimental results with 3 free parameters: the direction of the hard axis \mathbf{e}_h and the amplitudes of the spin-orbit torques (H_{FL} and H_{DL}). For every scan, first we fit the 1st harmonic response, where we extract the current-independent constant R_0 in equation 3.4. Then together with the R_0 , we use material parameters from the literature $H_D = 2$ T, $H_K = 0.01$ T and $H_{ex} = 900$ T [84–86] to fit the responses with our model. These fits allow us to extract the amplitudes of effective fields associated with the spin-orbit torques per current density which are $H_{FL}/J_{AC} \approx 7.5 \times 10^{-2}$ T/(10¹² A/m²) and $H_{DL}/J_{AC} \approx 4.2 \times 10^{-4}$ T/(10¹² A/m²).

A slight tilting ($\sim 3^\circ$) of the hard-axis \mathbf{e}_h from the \hat{z} -direction is needed in order to simultaneously capture the form of each and every one of the field scans. This tilt is especially crucial in 1st harmonic out-of-plane scans (XZ and YZ), where in order to get any non-zero response from

our model, we need some degree of canting of the easy plane. Moreover, to explain the shape of the response, an additional cosine term is needed, which we interpret as the ordinary Hall effect response of Pt.

3.4 SEPARATING THE HALL EFFECT AND THE SPIN SEEBECK CONTRIBUTIONS

There are also effects arising from the ordinary Hall effect induced by the perpendicular field component and from the spin Seebeck effect (SSE) due to a thermal gradient in the \hat{z} direction caused by Joule heating. Figure 3.3 summarizes how we extracted these contributions. On the left (Fig. 3.3(a) and (c)), we show the field dependence of 1st harmonic YZ and 2nd harmonic XY scans. And, on the right (Fig. 3.3(b) and (d)), we show the separated contributions of Hall effect and SSE from those scans, respectively. The field dependence of the signals can be used to isolate different contributions to the signal, as well as to show the model field dependence with the experimental results.

Figure 3.3(b) shows the Hall effect contribution in 1st harmonic and YZ scans. Since the expected Hall contribution is in the form $R_H^{1\omega} = HR_0^H \cos \theta$, the linear trend with applied field supports our claim. Similarly, Fig. 3.3(d) shows decomposition of $R_{xy}^{2\omega}$ into two components: Field-like SOT (blue) $R_{FL}^{2\omega}$ and spin Seebeck effect (orange) $R_{SSE}^{2\omega}$. In this case, the expected signals are of the form $R_{FL}^{2\omega} = HR_0^{FL} \cos 2\alpha \cos \alpha$ and $R_{SSE}^{2\omega} = HR_0^{SSE} \cos \alpha$ for field-like and SSE contributions, respectively. The form of the SSE contribution indicates that the effect is associated with the excess moment in the so called the transverse spin Seebeck geometry, in which the signal scales linearly with the applied field [87]. Furthermore, the remaining field-like component decreases with increasing applied magnetic field and follows a $1/H$ dependence, as in Eq. 5. We attribute the deviation from a $1/H$ dependence at low and high fields to the fact that our model assumptions are not valid in those limits. Specifically at low fields, the field amplitude is not enough

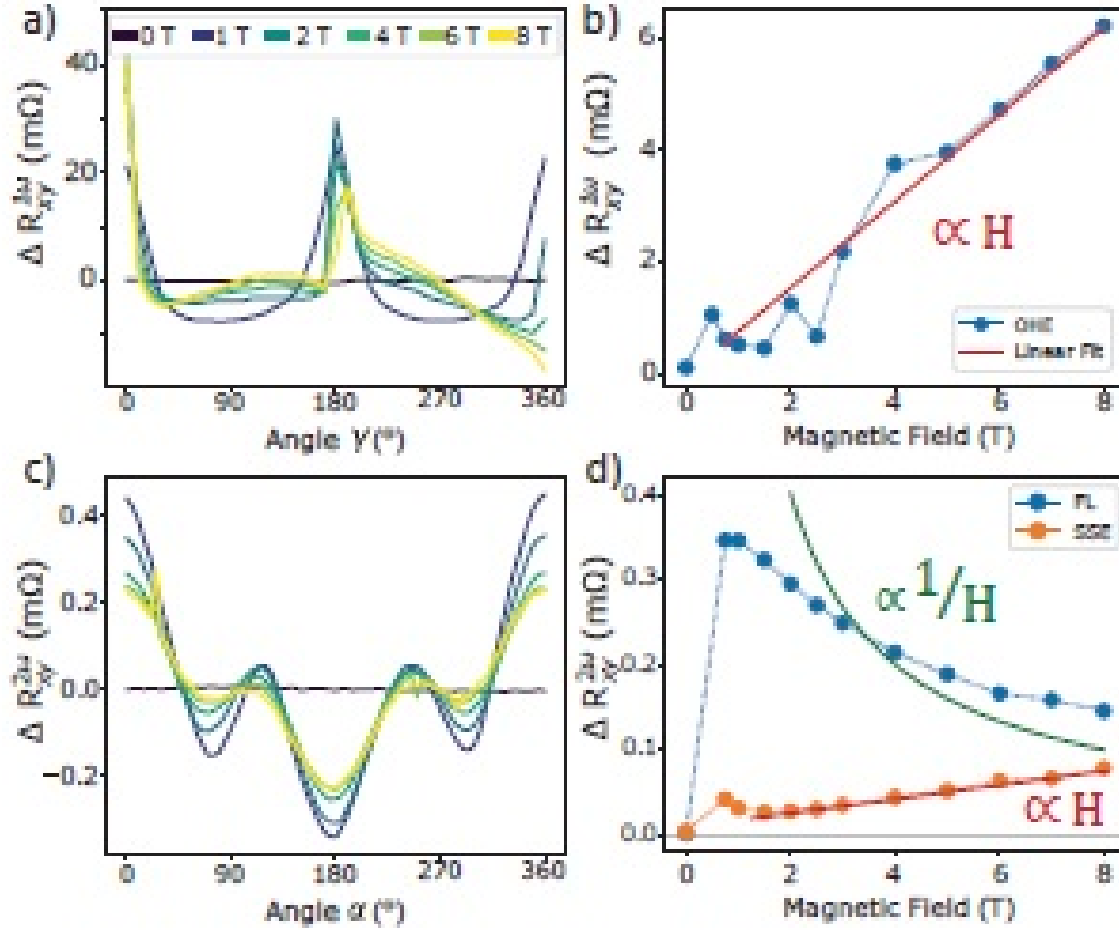


Figure 3.3: Separating Hall effect and spin Seebeck effect contributions. a) Field dependence of 1st harmonic response in YZ scan, from 0 to 8 T as indicated by the legend. b) The Hall effect in 1st harmonic YZ scan (a), as a function of applied field. The linear trend line supports the claim that the origin of the signal is the ordinary Hall effect. c) Field dependence of 2nd harmonic response in XY scan, which shares the same legend as (a). d) Antiferromagnetic spin Seebeck effect (SSE) separated from field-like SOT in 2nd harmonic XY scan (c), as a function of applied field. The field-like component scales as $1/H$, whereas the SSE component scales linearly with H .

to saturate all the domains, and at high field the assumption of excess moment being negligible, $|m| \ll 1$, is invalid.

3.5 SPIN-MIXING CONDUCTANCE OF THE AFM/HM INTERFACE

Our experimental results show that the field-like torque is about two orders of magnitude larger than the damping-like torque, distinct from what is found in ferromagnets [88, 89]. This implies that in the spin mixing conductance $g = g_r + ig_i$ —which characterizes the spin transmission across the interface—the imaginary part g_i far exceeds the real part g_r , as $H_{\text{DL}} \sim g_r J_{\text{AC}}$ and $H_{\text{FL}} \sim g_i J_{\text{AC}}$ (see more detailed discussion in section 3.10). To get at the origin of this unusual observation, we calculate g_i and g_r for a compensated interface by considering interfacial spin-dependent scattering processes, because electrons can deliver angular momenta to the magnetic moments near the interface through spin-flip scattering [70, 90], which manifests as spin torques exerting on the AFM. The interfacial scattering here depends on three parameters: the electron hopping energy t in the NM (determined by the Fermi energy), the proximity-induced hopping t_m on the AFM side of the interface² and the interfacial exchange coupling J between conduction electrons in the NM and the magnetic moments in the AFM. In Fig. 3.4 we plot the dependence of g_r and g_i on two dimensionless parameters $\lambda = J/t$ and $\delta = t_m/t$.

We see from Fig. 3.4 that regions with small λ and δ have $g_i/g_r > 1$. This ratio can become extremely large when λ becomes even smaller, which, when comparing with our experiment, indicates that the Pt/ α -Fe₂O₃ interface just falls in the region of very small λ and δ . In general, the ratio g_i/g_r can vary over a wide range of values depending on λ and δ , thus it is expected that the relative strength of the field-like and damping-like torques can vary significantly in different materials.

²In AFM, the spin and sublattice degrees of freedom are locked together. Therefore, a spin-flip scattering must involve electron hopping between the two sublattices on the AFM side of the interface. Since the AFM is insulating by itself, such a process must rely on the proximity-induced t_m .

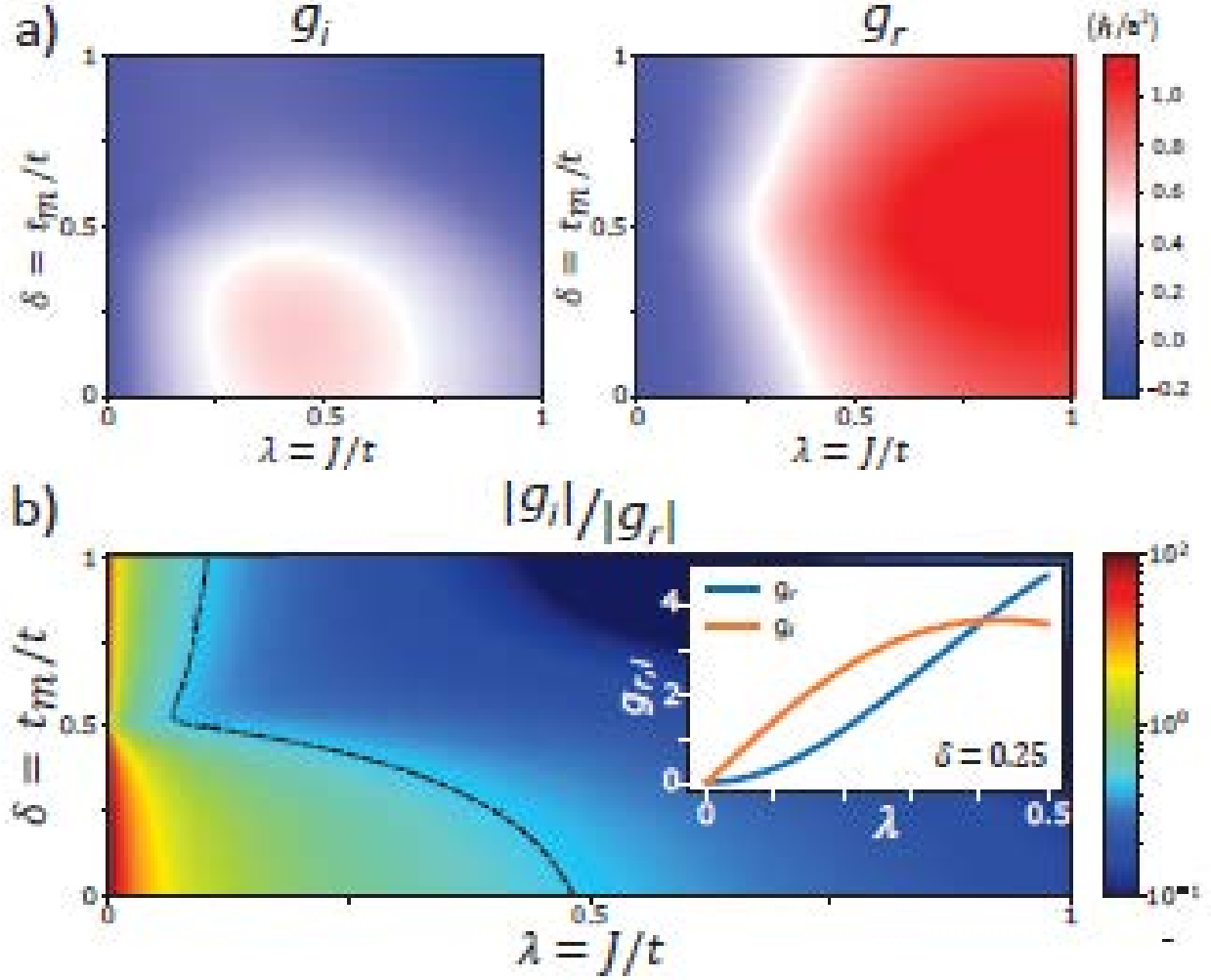


Figure 3.4: a) Imaginary (left) and real (right) parts of the spin mixing conductance ($g = g_r + ig_i$) of an AFM/NM interface. The scale is indicated by the shared color bar on the right, with units of \hbar per unit area a^2 on the interface, where a is the lattice constant. b) Ratio of $|g_i|$ to $|g_r|$. As λ approaches zero $|g_i|$ dominates over $|g_r|$. The dashed line shows $|g_i| = |g_r|$, which separates the field-like torque dominating region ($g_i > g_r$) on the left from the damping-like torque dominating region ($g_r > g_i$) on the right. The color bar scale is logarithmic in this case. The inset shows a line cut of g_r and g_i vs. λ at $\delta=0.25$. Even though they both approach zero as λ goes to zero, g_r decreases faster than g_i and their ratio g_i/g_r diverges.

3.6 FIELD DEPENDENCE OF THE HARMONIC SIGNAL

In Fig. 3.5 we show the full data set used for full analysis of spin-orbit torques and separation of the spin Seebeck effect and ordinary Hall effect. It consists of 1st and 2nd harmonic resistances in XY, XZ and YZ scans, as a function of external field strength. Figure 3.2 shows the data and the fit at $\mu_0 H = 3$ T as our model's approximations best apply to intermediate field strengths. Notice in out-of-plane scans (XZ and YZ), there are jumps in the response around 0° and 180°. This is because as the field becomes perpendicular to the surface, the in-plane component of the field vanishes. That means the in-plane magnetic anisotropy and the in-plane field needed to maintain a single domain state become important, which was ignored in the model.

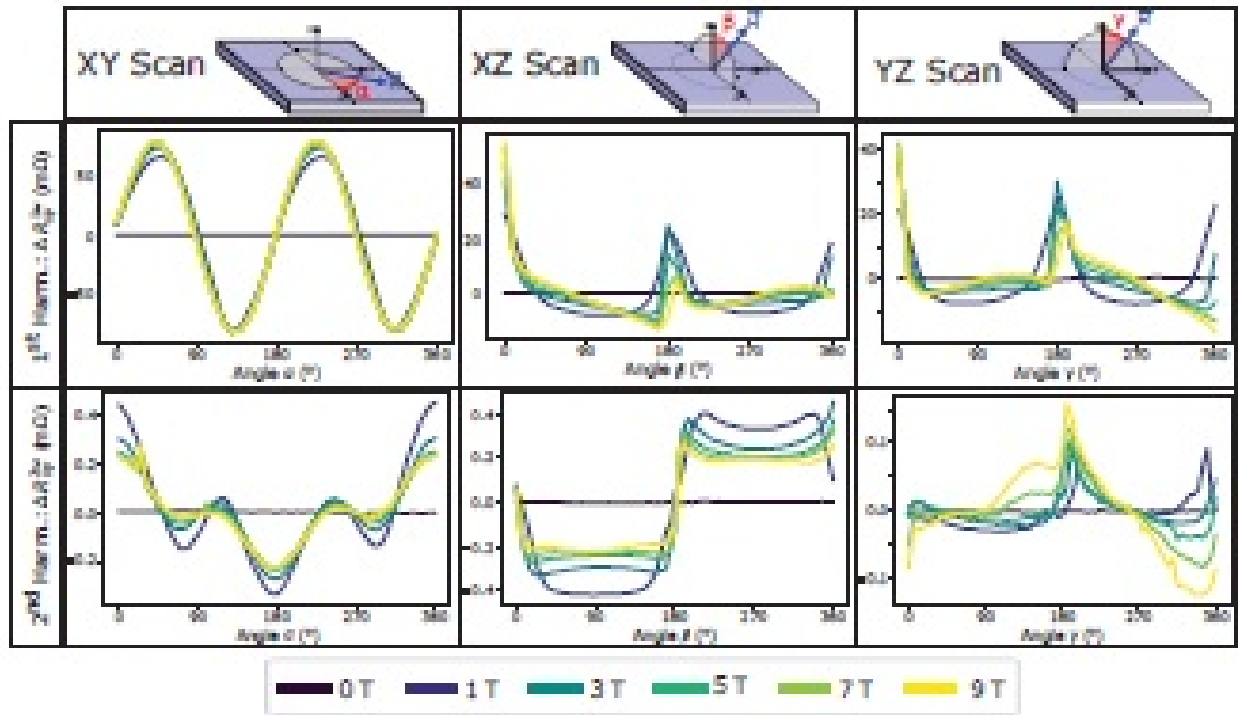


Figure 3.5: Full angular dependence of 1st and 2nd harmonic (rows) resistance signals in XY, XZ and YZ scans (columns) as a function of magnetic field strength. External magnetic field strength is scanned from 0 to 9 T as indicated by the legend. Geometry of magnetic field scans in the 3 principal planes (XY, XZ and YZ scans) and the definition of the angles α , β and γ are shown at the top. The current amplitudes are 100 μ A and 1.5 mA in the 1st and 2nd harmonic measurements, respectively. The current is always along \hat{x} direction and the resulting spin accumulation σ_{AC} is in the \hat{y} direction.

3.7 FINITE ELEMENT SIMULATIONS OF OERSTED FIELDS

As equation 3.4 suggest, the contribution of field-like torques and the Oersted fields to the second harmonic signal has the same symmetry. Therefore one must check the amplitude of Oersted fields before concluding the signal is due to the field-like torques. Oersted fields around the Pt wire are computed using finite-element method via COMSOL MultiPhysics® software. The simulation was done using the electromagnetism package in a 2-dimensional setting. The current density is 6×10^{10} A/m² in +z direction, out of the page in Fig. 3.6. This simulation showed that in very close vicinity of the Pt surface (< 30 nm), the amplitude of the Oersted fields is about 2×10^{-5} T, which is two orders of magnitude smaller than field-like torques at the same current density ($H_{FL} \approx 4.5 \times 10^{-3}$ T). Equation 1.1 shows that field-like torques and Oersted fields have identical effects on the 2nd harmonic resistance response. This finite element simulation allows us to conclude the signal is dominated by the field-like torques and not by Oersted fields.

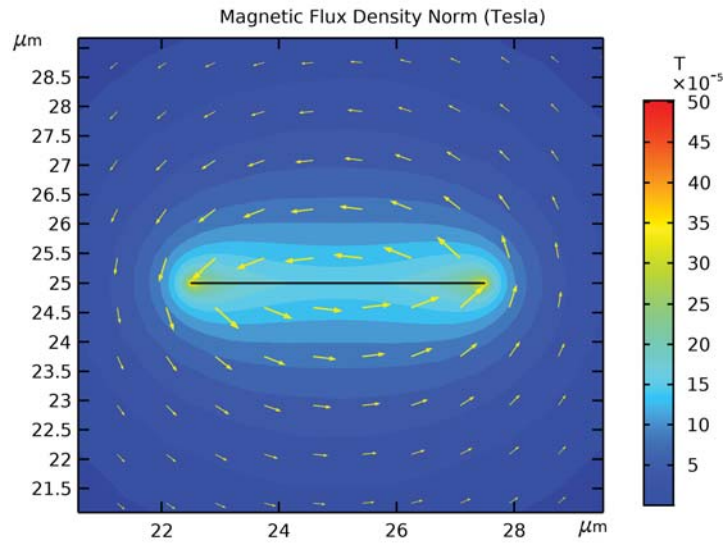


Figure 3.6: Finite-element simulation of Oersted fields created by a metal wire of dimensions of $5 \mu\text{m} \times 5$ nm. The current is in +z direction which is perpendicular to the page. Yellow arrows show the direction of local magnetic field vector and are proportional to its magnitude. The contour color map also indicates the norm of the magnetic field. In very close vicinity of the Pt surface (< 30 nm), the amplitude of the Oersted fields is around 2×10^{-5} T.

3.8 CURRENT DEPENDENCE OF HARMONIC SIGNALS

Here we take a present measurements of the current dependence of 1st and 2nd harmonic voltage signals from XY scans. The plots are shown on a log-log scale so the slope of the lines reveals the exponent n of current dependence of the voltage signal ($V \sim I^n$). As expected, the 1st harmonic voltage depends linearly on the current, whereas 2nd voltage depends quadratically on the current. This confirms that we are measuring the harmonic components without any mixing of the signals.

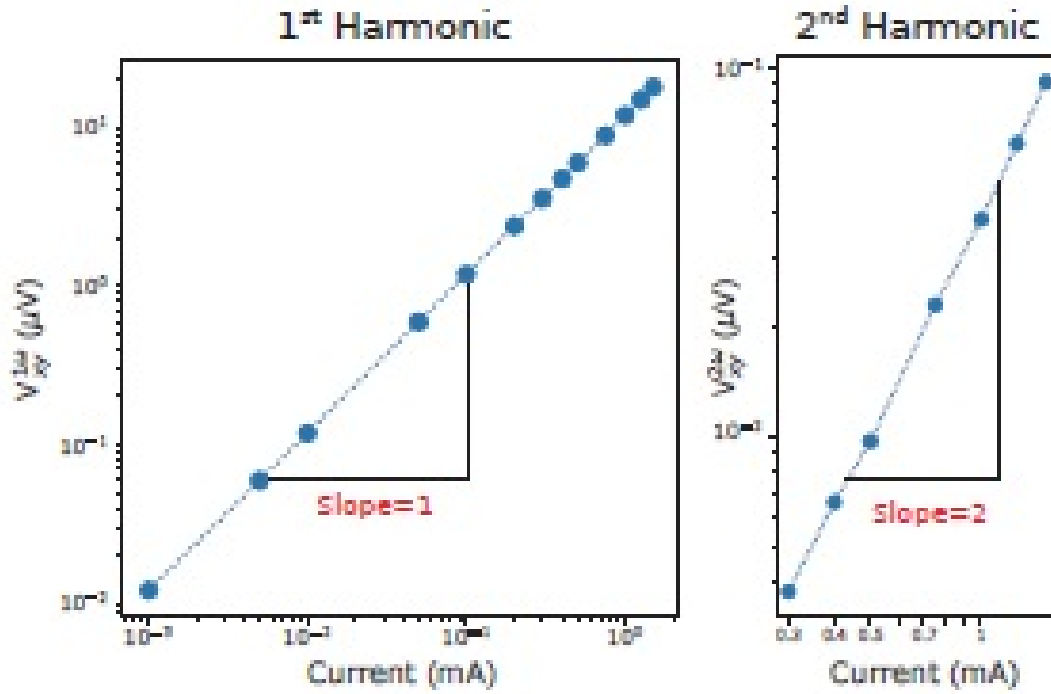


Figure 3.7: Current dependence of 1st and 2nd harmonic voltages in log-log scale. The slopes of the curves indicates exponent of the current dependence ($V \sim I^n$). As expected, the 1st harmonic voltage signal depends linearly on the current, whereas the 2nd harmonic voltage depends quadratically on the current.

3.9 EFFECTS OF FIELD-LIKE AND DAMPING-LIKE TORQUES

In this section, we will look more closely to the effects of spin-orbit torques on the antiferromagnetic magnetization dynamics in our system, by specifically isolating and comparing the effects of field-like and damping-like torques. The assumptions that were previously made about $\alpha\text{-Fe}_2\text{O}_3$ are still the same, i.e. it is an easy-plane system with DMI and we ignore the tri-axial anisotropy within the easy-plane.

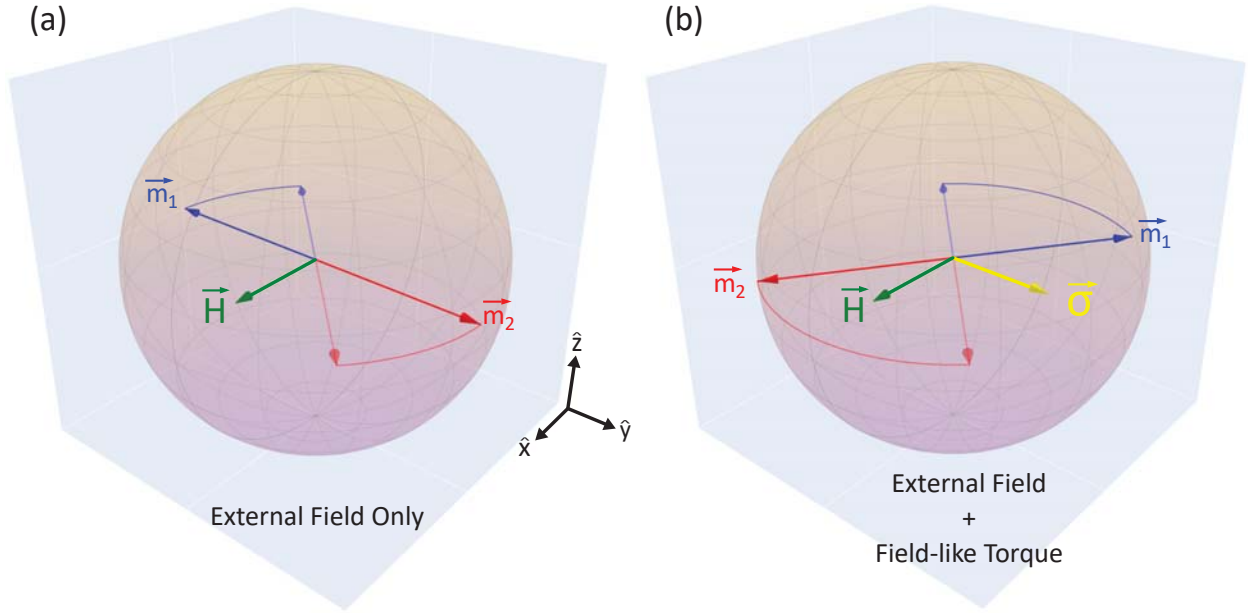


Figure 3.8: Time evolution of sublattice moments \vec{m}_1 and \vec{m}_2 under the effect of (a) external field only and (b) external field and field-like torque from a spin accumulation $\vec{\sigma}$. In both cases external field \vec{H} is in \hat{x} -direction and in (b) $\vec{\sigma}$ is in \hat{y} -direction indicated by the coordinate axes. Transparent arrows represent the arbitrarily chosen initial state. In case (a) at equilibrium state \vec{n} is perpendicular to \vec{H} and in case (b) \vec{n} is perpendicular to vector addition of $\vec{\sigma}$ and \vec{H} .

During the harmonic measurements, the actual effects of both torques are small compared to Gilbert damping and the external field, hence they are considered perturbative. They also oscillate with the frequency $\omega/2\pi = 953$ Hz, alternating their directions and counteracting themselves thousand times a second. Therefore, it is really hard to develop an intuitive picture for magnetization dynamics affected by spin-orbit torques. Here, we will look at cases where the effect of

torques are isolated, exaggerated and constant in time. Even though the torques are much larger than those present in the experiment, it will highlight the fundamental differences between the effects field-like and damping-like torques.

We will start by turning on only the external field \mathbf{H} first, which is along the \hat{x} axis. Figure 3.8(a) shows the time evolution of sublattice moments \mathbf{m}_1 and \mathbf{m}_2 under the effect of this magnetic field. The initial state was arbitrarily chosen to be in the XY plane and 45° from both \hat{x} and \hat{y} axes, and represented by the semi-transparent vectors. As expected sublattice moments \mathbf{m}_1 and \mathbf{m}_2 keep their antiparallel alignment while rotating in the easy-plane and they reach to the equilibrium state which is perpendicular to the external field \mathbf{H} .

Next, we turn on the spin accumulation σ along the \hat{y} axis, but only include the effects of field-like torque. Figure 3.8(b) shows the time evolution of the Néel vector from the same initial state. Again sublattice moments \mathbf{m}_1 and \mathbf{m}_2 rotate within the easy-plane, but this time the equilibrium state is perpendicular to the vector addition of σ and \mathbf{H} ³. This is exactly the expected behavior of the magnetization if there were an external effective field \mathbf{H}_{eff} in place of σ , hence the name field-like torque.

For the damping-like torque, depending on the magnitude of the torques, there are two different scenarios. Figure 3.9(a) depicts the scenario when the damping like torque is small compared to Gilbert damping α . The damping-like torque cants the sublattice moments towards each other and subsequently the exchange torque causes the Néel vector rotate out-of-plane. But the damping effect is strong enough so the rotation dies out and Néel vector settles to the equilibrium position that is perpendicular to \mathbf{H} . Whereas, when damping-like torque is large enough to overcome damping in Fig. 3.9(b), the Néel vector keeps rotating out-of-plane and perpendicular to the σ because damping-like torque is counteracting the Gilbert damping and sustaining enough energy for the system to oscillate indefinitely. In this specific case the external \mathbf{H} does not have

³It is not a coincidence that Néel vector ends up perpendicular to the vector addition of σ and \mathbf{H} . The amplitude of the effective field associated with field-like torque is chosen to be same as the external field

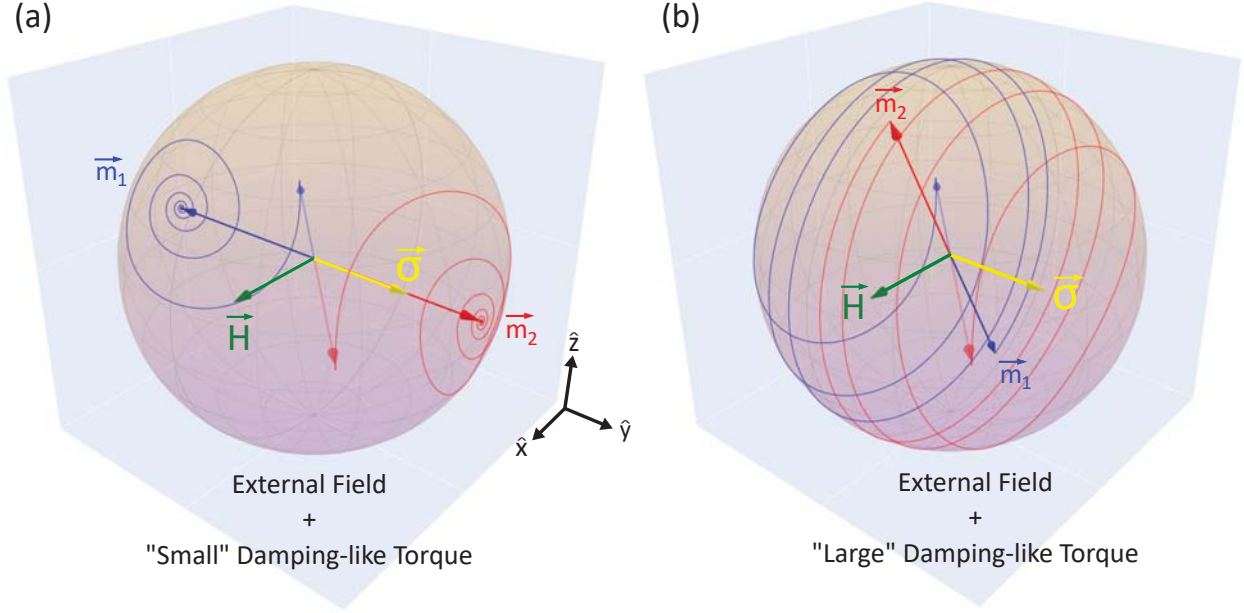


Figure 3.9: Time evolution of sublattice moments \vec{m}_1 and \vec{m}_2 under the effect of (a) external field and small damping like torques and (b) external field and large damping like torques. In both cases external field \vec{H} is in \hat{x} -direction and $\vec{\sigma}$ is in \hat{y} -direction similar to Fig. 3.8. Transparent arrows represent the arbitrarily chosen initial state. In case (a), at equilibrium state sublattice moments start to precess around the spin accumulation $\vec{\sigma}$, but the anti-damping effect is not large enough to sustain the oscillations so it reaches equilibrium state that is perpendicular to \vec{H} . In case (b), the anti-damping effect is large enough to overcome damping and \vec{n} starts rotating in the XZ plane which is perpendicular to $\vec{\sigma}$.

an appreciable effect on the dynamics of the system.

3.10 CALCULATION OF THE SPIN-MIXING CONDUCTANCE

To explain why the FL torque is much larger than the DL torque, we must determine the imaginary part of the spin-mixing conductance g_i and its relative strength with respect to the real part g_r . For coherent spin pumping in terms of $\vec{n} = (\vec{m}_1 - \vec{m}_2)/2$ and $\vec{m} = (\vec{m}_1 + \vec{m}_2)/2$, the spin-mixing conductance appears in the spin current as

$$\frac{2\pi}{\mathcal{A}} \vec{I}_s = g_r(\vec{n} \times \dot{\vec{n}} + \vec{m} \times \dot{\vec{m}}) - g_i \dot{\vec{m}}, \quad (3.6)$$

where \mathcal{A} is the area of the interface, g_r and g_i are scaled into the areal density of spin angular momenta (the units will be specified below). Since g_i only contributes to the AC component of spin pumping and \mathbf{m} itself is very small, its role was ignored in the study of spin pumping where only the DC component can be measured. For this reason, only g_r was calculated while g_i was overlooked in previous studies [90, 91]. However, for current-induced torques and their manifestations in the harmonic signal, the situation becomes drastically different.

Using Onsager's reciprocity relations, the DL and FL torques acting on the two sublattices $\mathbf{m}_{1,2}$ are

$$\boldsymbol{\tau}_{1,2}^{\text{DL}} = J_{\text{AC}} \frac{a^3}{ed_M} g_r f_d \mathbf{m}_{1,2} \times [\mathbf{m}_{1,2} \times \boldsymbol{\sigma}], \quad (3.7)$$

$$\boldsymbol{\tau}_{1,2}^{\text{FL}} = J_{\text{AC}} \frac{a^3}{ed_M} g_i f_d \boldsymbol{\sigma} \times \mathbf{m}_{1,2}, \quad (3.8)$$

where J_{AC} is the applied AC current density, a is the lattice constant, e is the electron charge, d_M is the AFM thickness, and $f_d = f_d(\theta_{\text{SH}}, \lambda_N, \sigma_N, d_N)$ is a dimensionless diffusion factor determined by the material properties of the NM with θ_{SH} , λ_N , σ_N and d_N the spin-Hall angle, spin diffusion length, conductivity and thickness of the NM, respectively. The diffusion factor f_d can vary significantly depending on the materials details of the NM, but in the exchange limit $|\mathbf{m}| \ll |\mathbf{n}|$, it does not change the relative strength of $\boldsymbol{\tau}_{\text{DL}}$ and $\boldsymbol{\tau}_{\text{FL}}$ so we do not have to specify its form.

Following Refs. [90, 91], the spin-mixing conductance $g = g_r + ig_i$ can be obtained by calculating the spin-dependent scattering on an AFM/NM interface. Without loss of generality, we consider an AFM/NM interface with simple cubic lattice and a shared lattice constant a on both sides. This simplified model is sufficiently good to capture the essential physics, as variations of lattice structure only introduces quantitative differences in the results. As illustrated in Fig. 3.10(a), we consider a G-type compensated interface with electrons from the NM only coupled to the magnetic moments on the outermost magnetic layer. The coordinate system is chosen such that the interface normal is along x ; y and z axes are rotated by $\pi/4$ with respect to lattice as illustrated

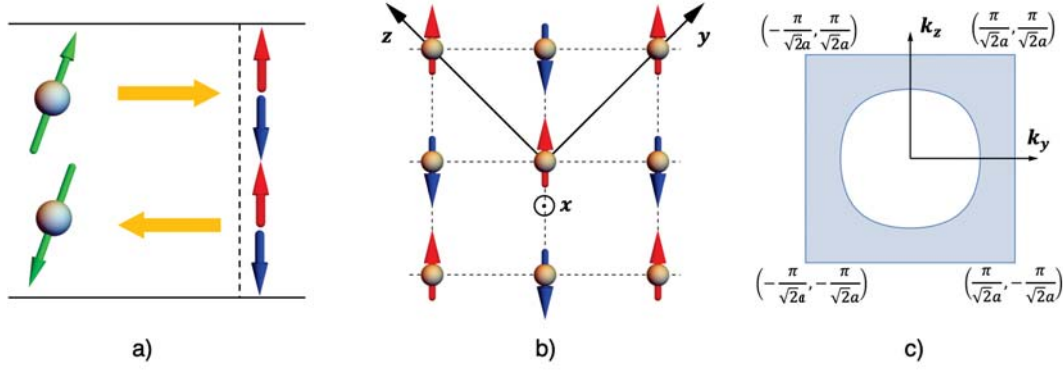


Figure 3.10: a) Illustration of spin-flip scattering at the AFM/NM interface. b) Coordinate system on the interface. c) The region of integration is shaded, where k_y and k_z satisfy $2 \cos \frac{k_y a}{\sqrt{2}} \cos \frac{k_z a}{\sqrt{2}} < 1$. Figure is taken from [90].

in Fig. 3.10(b).

The scattering of electrons at the interface can be characterized by a scattering matrix S in which the spin and pseudo-spin (sublattice) degrees of freedom are intertwined. Since we are considering an insulating AFM, only the reflected waves are propagating, while the transmitted waves decay exponentially. In the exchange limit, $|\mathbf{m}| \ll |\mathbf{n}|$, the scattering matrix reduces to to [90, 91]

$$S = S_0 \hat{\tau}_0 \hat{\sigma}_0 + S_w \hat{\tau}_1 \hat{\sigma}_0 + \Delta S [\hat{\tau}_3 (\mathbf{n} \cdot \hat{\sigma}) + \hat{\tau}_0 (\mathbf{m} \cdot \hat{\sigma})], \quad (3.9)$$

where $\hat{\tau}_i$ denote the Pauli matrices for the pseudospin (sublattice) degree of freedom while $\hat{\sigma}_i$ are the spin Pauli matrices; $\hat{\tau}_0$ and $\hat{\sigma}_0$ are identity matrices. Here, the first two terms represent spin-independent reflections, whereas the last two terms correspond to the spin-dependent Umklapp scattering and normal scattering, respectively. Because $|\mathbf{n}| \gg |\mathbf{m}|$, the Umklapp scattering turns out to be crucial, which is directly related to the lateral hopping energy t_m on the magnetic side of the interface. A finite t_m is attributed to the proximity effect such that the outermost magnetic layer in direct contact to the normal metal becomes conducting. Depending on the strength of proximity effect, t_m/t ranges from 0 to 1 where t is the hopping energy in the bulk of NM (determined by the Fermi energy).

By matching the wave functions on the interfaces under current density normalization conditions, the spin-mixing conductance can be derived as

$$g_r = \frac{\hbar}{\pi^2} \iint_{\mathcal{D}} |\Delta S|^2 dk_y dk_z, \quad (3.10)$$

$$g_i = \frac{\hbar}{\pi^2} \iint_{\mathcal{D}} \text{Im}[S_0^* \Delta S] dk_y dk_z, \quad (3.11)$$

where the integration region \mathcal{D} is described by $2 \cos \frac{k_y a}{\sqrt{2}} \cos \frac{k_z a}{\sqrt{2}} < 1$ in the first Brillouin zone, as shown in Fig. 3.10c). While previous theoretical studies only showed the expression of $|\Delta S|^2$ (i.e., the integrand of g_r), here we derive the expressions of both components as

$$|\Delta S|^2 = \frac{4\lambda^2(1-K^2)}{[\lambda^2 + 1 + 4\delta(\delta-1)K^2]^2}, \quad (3.12)$$

$$\text{Im}[S_0^* \Delta S] = \frac{2\lambda\sqrt{1-K^2} [(K^2-1)(\lambda^2 + 4K^2\delta^2) + 1 - 4K^2\delta^2]}{[\lambda^2 + 1 + 4\delta(\delta-1)K^2]^2}, \quad (3.13)$$

where $K = 2 \cos \frac{k_y a}{\sqrt{2}} \cos \frac{k_z a}{\sqrt{2}}$, $\lambda = J/t$ and $\delta = t_m/t$ with J the interfacial exchange coupling between conduction electrons in the NM and magnetic moments in the AFM. Combining Eq. (3.10) - (3.13), we can compute g_r and g_i as functions of λ and δ . In Fig. 3.4, it is clear that in the lower left region bounded by the dashed line, g_i can be much larger than g_r while they both approach zero when λ goes to zero.

3.11 CONCLUSION OF THE CHAPTER

In conclusion, we determined the type and amplitude of SOTs in antiferromagnetic α -Fe₂O₃/Pt bilayers. An important finding is that the field-like torques are two orders of magnitude larger than damping-like torques, implying that the spin-mixing conductance of the α -Fe₂O₃/Pt interface has the unusual property of having a large imaginary component. It also points to magneto-elastic effects likely being the dominant mechanism of current-induced switching of the Néel

vector of in α -Fe₂O₃ [29, 31, 68]. Our method can be extended to other AFM/HM systems by starting with the appropriate model and assumptions (e.g. magnetic anisotropies, DMI) to determine harmonic response [83]. Overall, this work demonstrates a way to quantify SOTs and opens up a promising path for future studies on similar AFM/HM heterostructures as well as a means that can be used in optimizing SOT on AFM for applications.

4 | CONCLUSION AND PERSPECTIVES

This thesis summarizes my graduate studies on antiferromagnetic insulators α -Fe₂O₃ and NiO, specifically their antiferromagnetic domain structures and current induced dynamics. In the introduction, I presented some of the prerequisite knowledge to understand the research goals of both of my projects, as well as a brief introduction to the field of antiferromagnetic spintronics. I also presented the state-of-the-art by highlighting some of the recent and impactful research articles and discussed some open questions in the field.

In Chapter 2, I presented the findings of imaging studies on two insulating antiferromagnets. In α -Fe₂O₃/Pt bilayers, repeatable current-induced switching of antiferromagnetic moments was detected. The images revealed that only a small fraction of the domains reorient, which is consistent with the electrical measurements. Depending on the location and the repeatability of the switching, two types of changes associated with the current pulses were identified: reversible and irreversible. Although it is likely that both SOT and thermally induced magnetostriction contribute to switching, experiments with high current density pulses demonstrated clearly that thermal effects alone can induce changes in the Néel order. In order to understand switching mechanisms better, future studies on AFM order are needed where the impacts of SOT and thermal effects are separated. This can be achieved by isolating the metal layers from the α -Fe₂O₃ electrically but not thermally, either using a specially designed lithographic pattern or with a spacer layer that is electrical insulator but a thermal conductor. Alternatively using a suitable piezoelectric substrates can give precise control over the amount of strain applied and would

help quantify the magneto-elastic effects. And finally a systematic study using different metals layer some with opposite spin-Hall angles (e.g. W or Ta) and some without spin-orbit coupling (e.g. Al or Cu) can help in understanding the switching mechanisms. In NiO/Pt bilayers, the effect of the substrate was studied by comparing 4 different substrates, MgO and piezoelectric PMN-PT, each grown along two different crystallographic directions. But only on MgO(001) substrates the antiferromagnetic domain contrast was large enough to conduct a systematic study. We measured the domain contrast as a function of x-ray polarization and in-plane sample rotation angle. We found that there is a crystal field component to the XMLD and a large out-of-plane component to the Néel vector, which is different that bulk value. Further optimization of growth parameters of NiO on piezoelectric substrates (especially PMN-PT) is needed to realize current free antiferromagnetic switching.

In Chapter 3, harmonic Hall measurements were conducted with the goal of quantifying the spin-orbit torques in $\text{Fe}_2\text{O}_3/\text{Pt}$, the same system we observed current induced switching. As a result of this study, we developed a general method that can be extended similar AFM/HM systems by modeling and measuring harmonic responses. The results surprisingly shows that damping like torques are significantly smaller than field like torques in our $\text{Fe}_2\text{O}_3/\text{Pt}$ samples. This implies that the spin-mixing conductance of the AFM/HM interface of our samples has the unusual property of having a large imaginary component. It also points to magneto-elastic effects likely being the dominant mechanism of current-induced switching of the Néel vector in our previous study. To summarize, this study demonstrates a way to quantify spin-orbit torques and opens up a promising path for future studies on similar AFM/HM heterostructures. Extending this method to other AFMs such as NiO would be natural continuation to this study. The main challenge here is applying large enough magnetic fields to rotate the Néel vector, since NiO doesn't have an easy-plane like $\alpha\text{-Fe}_2\text{O}_3$. Alternatively trying to optimize the interface of Fe_2O_3 by changing heavy metal layer or by using a ultra-thin layer of ferromagnet in between the AFM and the heavy metal might increase the efficiency of damping-like torques. In general, these type of studies can

act as a means that can be used in optimizing SOT on AFM for applications, especially for finding ways to increasing the real part of the spin-mixing conductance of the interface.

LIST OF PUBLICATIONS AND CONFERENCES

PUBLICATIONS

1. Yizhang Chen, Debangsu Roy, **Egecan Cogulu**, Houchen Chang, Mingzhong Wu, Andrew D. Kent, "First harmonic measurements of the spin Seebeck effect", Appl. Phys. Lett. **113**, 202403 (2018) [[92](#)].
2. Lauren J Riddiford, Jacob J. Wisser, Satoru Emori, Peng Li, Debangsu Roy, **Egecan Cogulu**, Olaf van't Erve, Yong Deng, Shan X. Wang, Berend T. Jonker, Andrew D. Kent, Yuri Suzuki, "Efficient spin current generation in low-damping $\text{Mg}(\text{Al,Fe})_2\text{O}_4$ thin films", Appl. Phys. Lett. **115**, 122401 (2019) [[93](#)].
3. Yizhang Chen, **Egecan Cogulu**, Debangsu Roy, Jinjun Ding, Jamileh B. Mohammadi, Paul G. Kotula, Nancy A. Missert, Mingzhong Wu, Andrew D. Kent, "Spin transport in an insulating ferrimagnetic-antiferromagnetic-ferrimagnetic trilayer as a function of temperature", AIP Advances **9**, 105319 (2019) [[94](#)].
4. Arun Parthasarathy, **Egecan Cogulu**, Andrew D. Kent, Shaloo Rakheja, "Precessional spin-torque dynamics in biaxial antiferromagnets", Phys. Rev. B **103**, 024450 (2021) [[72](#)].
5. **Egecan Cogulu**, Nahuel N. Statuto, Yang Cheng, Fengyuan Yang, Rajesh V. Chopdekar, Hendrik Ohldag, Andrew D. Kent, "Direct imaging of electrical switching of antiferromag-

- netic Néel order in α -Fe₂O₃ epitaxial films", Phys. Rev. B **103**, L100405 (2021) [68].
6. Laura Rehm, Georg Wolf, Bartek Kardasz, **Egecan Cogulu**, Yizhang Chen, Mustafa Pinarbasi, Andrew D. Kent, "Thermal Effects in Spin-Torque Switching of Perpendicular Magnetic Tunnel Junctions at Cryogenic Temperatures", Phys. Rev. Applied **15**, 034088 (2021) [95].
 7. **Egecan Cogulu**, Hantao Zhang, Nahuel N. Statuto, Yang Cheng, Fengyuan Yang, Ran Cheng, Andrew D. Kent, "Quantifying Spin-Orbit Torques in Antiferromagnet/Heavy Metal Heterostructures", arXiv:2112.12238 (2021) [96].
 8. Yang Cheng, **Egecan Cogulu**, Rachel D Resnick, Justin J Michel, Nahuel N. Statuto, Andrew D. Kent, Fengyuan Yang, "Third Harmonic Characterization of Antiferromagnetic Heterostructures", arXiv:2112.13159 (2021) [97].

CONFERENCE PRESENTATIONS

1. APS March Meeting 2018, "Unidirectional Spin Hall Magnetoresistance in $\text{Y}_3\text{Fe}_5\text{O}_{12}/\text{NiO}/\text{Pt}$ Structures", Los Angeles, California.
2. APS March Meeting 2019, "Spin Seebeck Effect in $\text{Y}_3\text{Fe}_5\text{O}_{12}/\text{NiO}/\text{Pt}$ Thin Film Heterostructures", Boston, Massachusetts.
3. MMM 2019, "Large Enhancement in Spin Transport Efficiency in $\text{Y}_3\text{Fe}_5\text{O}_{12}/\text{NiO}/\text{Pt}$ Heterostructures", Las Vegas, Nevada.
4. MMM 2020, "X-Ray Magnetic Linear Dichroism Studies of Electrical Switching of Antiferromagnetic Order in $\alpha\text{-Fe}_2\text{O}_3$ Epitaxial Films", Virtual.
5. Intermag 2021, "X-Ray Magnetic Linear Dichroism Studies of Electrical Switching of Antiferromagnetic Order in $\alpha\text{-Fe}_2\text{O}_3$ Epitaxial Films", Virtual.
6. APS March Meeting 2021, "X-ray Magnetic Linear Dichroism Studies of Electrical Switching of Antiferromagnetic Order in $\alpha\text{-Fe}_2\text{O}_3$ Epitaxial Films", Virtual.
7. AVS 67, "X-ray Magnetic Linear Dichroism Studies of Electrical Switching of Antiferromagnetic Order in $\alpha\text{-Fe}_2\text{O}_3$ Epitaxial Films", Virtual.
8. 2022 Joint MMM-Intermag Conference, "Quantifying Spin-Orbit Torques in AFM/HM Heterostructures by Harmonic Hall Measurements", New Orleans, Louisiana.
9. APS March Meeting 2022, "Quantifying Spin-Orbit Torques in AFM/HM Heterostructures by Harmonic Hall Measurements", Chicago, Illinois.

A | APPENDIX

HARMONIC MEASUREMENTS ON YIG/NiO/Pt TRILAYER HETEROSTRUCTURES

In this appendix, I will summarize my studies of harmonic Hall measurements conducted on tri-layer heterostructures of the form ferrimagnet-antiferromagnet-heavy metal (YIG-NiO-Pt) to detect spin transport through an insulating antiferromagnetic layer. In the measurements, a temperature gradient across the structure is created by applying high current densities to the heavy metal on top (Pt) and the amplitude of inverse spin Hall effect (ISHE) is detected as a function of temperature and magnetic field. The results were then compared to a control sample where there is no antiferromagnetic NiO layer. A sharp increase is observed around 110 K in the amplitude of spin Seebeck signal only in the sample with NiO. The fact that the peak doesn't exist in the control sample suggests that the origin is either the NiO layer or the YIG/NiO interface. We also measured the exchange bias effect as a function of NiO thickness, in order to characterize the effect of thin antiferromagnetic NiO layer on the ferrimagnetic YIG.

A.1 SAMPLE CHARACTERISTICS AND MEASUREMENT GEOMETRY

20 nm of $\text{Y}_3\text{Fe}_5\text{O}_{12}$ (yttrium iron garnet or YIG for short) were deposited on $\text{Gd}_3\text{Ga}_5\text{O}_{12}$ (GGG) substrates by Prof. Wu's research group at Colorado State University. Then the YIG samples were

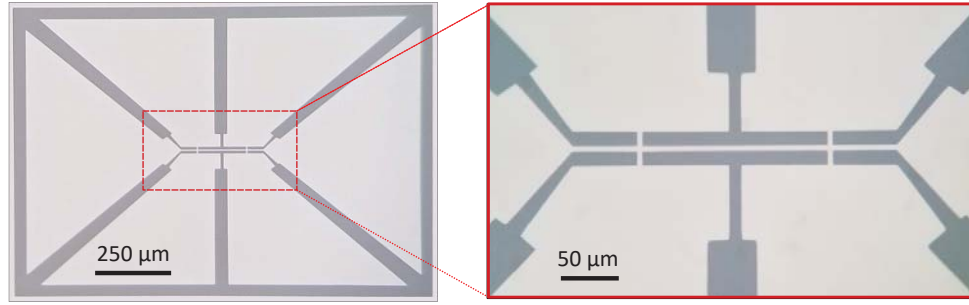


Figure A.1: Optical microscopy image of a Hall-bar structure. Darker regions are electrically insulating NiO and lighter regions are highly conductive Pt. The scale bars visible for each image.

transferred to NYU where they were surface cleaned by Ar^+ plasma for 30 seconds inside the deposition chamber and subsequently 2, 5 and 13 nm of NiO layers deposited from a NiO target using 100 Watts RF power in presence of 3 mTorr gas pressure (consisting of 90% Argon and 10% Oxygen) at 600 °C. Finally 5 nm of platinum is deposited at 150 °C using 30 W of power, in-situ without breaking the vacuum. Hall-bar structures were patterned using e-beam lithography and etched by Ar^+ milling. Figure A.1 shows an optical microscopy image of the resulting Hall bar structure. Darker regions are where Pt is etched away and insulating whereas lighter regions are covered with Pt.

A.2 MEASURING THE SPIN SEEBECK EFFECT

Spin Seebeck Effect is the generation of incoherent spin waves by a thermal gradient inside a ferromagnet [98]. It is usually measured in longitudinal geometry —where spin current is parallel to the thermal gradient — with the help of the Inverse Spin Hall Effect (ISHE) through a heavy metal and it is one of the most efficient and practical ways of creating spin waves.

In our heterostructures, thermal gradients in the \hat{z} -direction are created because of the AC current passing from Pt layer. Thermally generated spins from the ferrimagnetic YIG layer diffuse through the NiO and converted into a voltage signal at the Pt layer by the inverse spin Hall effect. Since spin Seebeck effect a thermal effect and depends on the current amplitude quadratically,

this creates a detectable signal in the 2nd harmonic response. The external field sets the direction of YIG magnetization and as we rotate the field in the xy -plane the ISHE voltage detected through Pt layer changes, as shown in Fig. A.2(a).

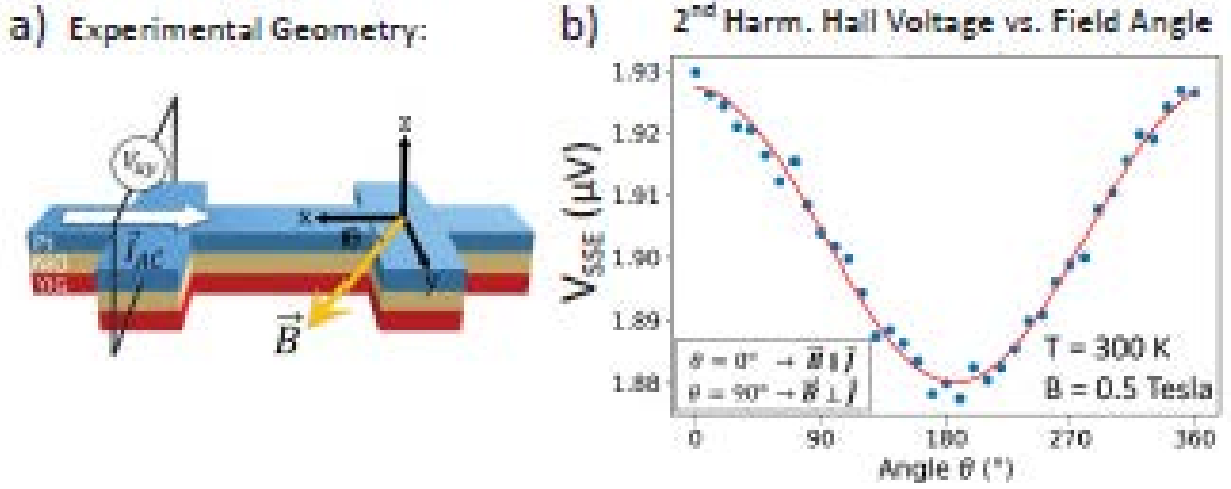


Figure A.2: (a) Schematic of sample and measurement geometry. The current is always in the \hat{x} -direction and the magnetic field \vec{B} is scanned in the XY plane where the angle θ is measured from the x -axis. (b) Example fit of the second harmonic response at $T = 300$ K and $|\vec{B}| = 0.5$ Tesla.

We use the following function to fit the transverse 2nd harmonic voltage response $V_{xy}^{2\omega}$, as we rotate the external field \vec{B} in the XY -plane:

$$V_{xy}^{2\omega} = V_{SSE} \sin(\theta + \phi) + C, \quad (A.1)$$

where V_{SSE} is the amplitude of the spin Seebeck effect, θ is the angle between the in plane field and the \hat{x} axis, ϕ is the phase of the signal and C is the constant 2nd harmonic voltage offset. Figure A.2(b) shows an example fit at field amplitude $|\vec{B}| = 0.5$ Tesla and $T = 300$ K.

A.3 TEMPERATURE DEPENDENCE OF THE SPIN SEEBECK EFFECT

We have done the in-plane rotation experiment that is shown in Fig. A.2(b) for a range of temperature values (10 K to 300 K) to for both YIG/NiO/Pt and YIG/Pt control samples.

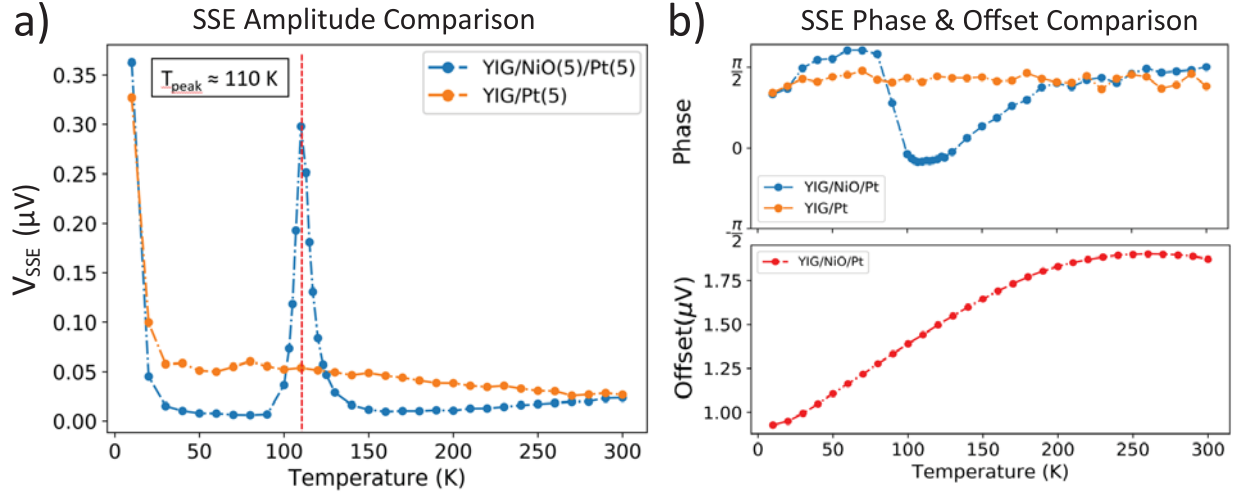


Figure A.3: (a) Temperature dependence of the Spin Seebeck Effect on YIG/Pt and YIG/NiO/Pt layers. The sharp increase of amplitude only present in the sample with NiO. (b)

Figure A.3 summarizes the temperature dependence of the fit parameters from Eq. A.1 and compares fit parameters of YIG/NiO/Pt to the control sample YIG/Pt. The amplitude of the SSE is generally reduced in samples with NiO as expected. However, a large sharp peak in the SSE response is observed around 110 K. Additionally the phase of the SSE signal ϕ shifts by 90° at the same peak amplitude temperature. But the offset C behaves similarly regardless of the existence of the NiO layer. It is not clear if this peak is associated with an increased spin conductivity of the NiO or there is an additional contribution to spin Seebeck effect coming from NiO at that specific temperature. The fact that phase of the signal suggest the coupling between NiO moments and YIG moments changes at the critical temperature $T = 110$ K.

A.4 FIELD DEPENDENCE OF THE SPIN SEEBECK EFFECT

We have also looked at the external field amplitude dependence of the spin Seebeck effect. Figure 2 summarizes how the spin Seebeck amplitude behaves as a function of temperature at 3 different external field amplitudes, $|\vec{B}| = 0.1, 0.5$ and 1 Tesla. Note that 1 Tesla is more than enough to saturate Fe moments in the YIG. The peak around stays approximately at the sample temperature but its linewidth and amplitude increases with increasing magnetic field. This is resembles paramagnetic behavior as the signal strength increases with the field amplitude.

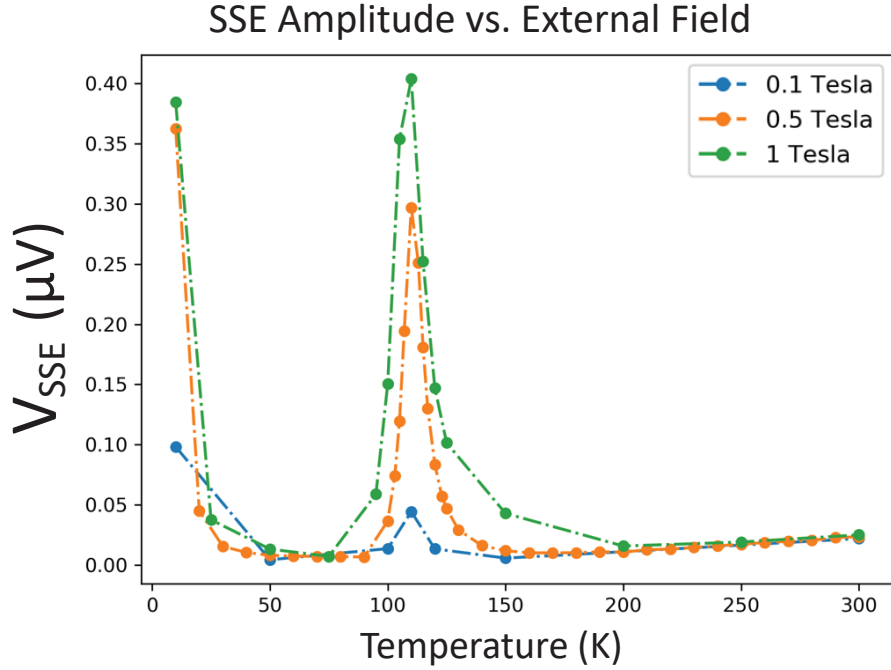


Figure A.4: SSE amplitude as a function of temperature at different external field amplitudes $|\vec{B}| = 0.1, 0.5$ and 1 Tesla. The peak at 110 K is visible at all 3 curves but the amplitude of the peak clearly increases with increasing external field amplitude.

A.5 THICKNESS AND TEMPERATURE DEPENDENCE OF THE EXCHANGE BIAS EFFECT

Exchange bias is an effect where antiferromagnetic thin film such as NiO causes a shift in the magnetization curve, also known as the M-H curve, of a ferromagnetic film. We measured the thickness and temperature dependence of the exchange bias with the expectancy to help us understand the nature of the peak in the SSE amplitude.

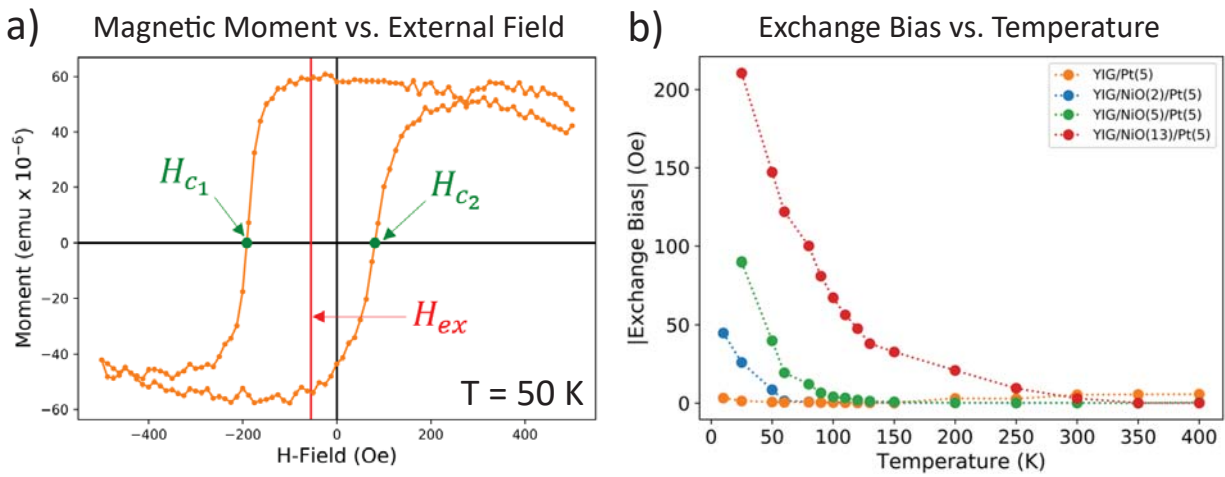


Figure A.5: (a) An example M-H curve of the tri-layer structure YIG/NiO(5)/Pt at $T = 50$ K. Coercive fields H_{c1} and H_{c2} are marked by green arrows and the average of the two coercive fields is calculated as exchange bias amplitude H_{ex} . (b) Exchange bias amplitude H_{ex} as a function of thickness of the NiO layer and the temperature.

Figure A.5 summarizes the results of the exchange bias measurements on 4 different samples with NiO thickness 0, 2, 5 and 13 nanometers. In general exchange bias amplitude and the temperature of the onset of the exchange bias increases with increasing thickness of the NiO layer. More interestingly, for the YIG/NiO(5)/Pt sample the onset of the exchange bias is around 110 K, where the peak of the SSE amplitude is measured.

To summarize, we have characterized the spin-Seebeck effect in YIG/NiO/Pt structures with very thin NiO layers. A comparison between results on YIG/NiO/Pt and YIG/Pt shows spin trans-

port greatly increases at some critical temperature. This increase in the spin-Seebeck effect might be correlated with an increase in the magnetic susceptibility of NiO. Our results suggest that the spin-Seebeck effect can be used to characterize the response of thin antiferromagnetic materials and optimize their spin-transport characteristics, but further investigations are needed to identify the exact origin of the signal.

BIBLIOGRAPHY

- [1] M. N. Baibich et al. “Giant Magnetoresistance of (001)Fe/(001)Cr Magnetic Superlattices”. In: *Phys. Rev. Lett.* 61 (21 Nov. 1988), pp. 2472–2475. DOI: [10.1103/PhysRevLett.61.2472](https://doi.org/10.1103/PhysRevLett.61.2472).
- [2] G. Binasch et al. “Enhanced magnetoresistance in layered magnetic structures with antiferromagnetic interlayer exchange”. In: *Phys. Rev. B* 39 (7 Mar. 1989), pp. 4828–4830. DOI: [10.1103/PhysRevB.39.4828](https://doi.org/10.1103/PhysRevB.39.4828).
- [3] Louis Néel. *Nobel Lectures, Physics 1963-1970*. Elsevier Publishing Company, Dec. 1970.
- [4] Kaori Fukunaga and Marcello Picollo. “Terahertz spectroscopy applied to the analysis of artists’ materials”. In: *Applied Physics A* 100.3 (Mar. 2010), pp. 591–597. DOI: [10.1007/s00339-010-5643-y](https://doi.org/10.1007/s00339-010-5643-y).
- [5] I. Dzyaloshinsky. “A thermodynamic theory of “weak” ferromagnetism of antiferromagnetics”. In: *Journal of Physics and Chemistry of Solids* 4.4 (Jan. 1958), pp. 241–255. DOI: [10.1016/0022-3697\(58\)90076-3](https://doi.org/10.1016/0022-3697(58)90076-3).
- [6] Albert Fert, Vincent Cros, and João Sampaio. “Skyrmions on the track”. In: *Nature Nanotechnology* 8.3 (Mar. 2013), pp. 152–156. DOI: [10.1038/nnano.2013.29](https://doi.org/10.1038/nnano.2013.29).
- [7] Charles Kittel and Donald F. Holcomb. “Introduction to Solid State Physics”. In: *American Journal of Physics* 35.6 (June 1967), pp. 547–548. DOI: [10.1119/1.1974177](https://doi.org/10.1119/1.1974177).

- [8] Isaiah Gray et al. “Spin Seebeck Imaging of Spin-Torque Switching in Antiferromagnetic Pt/NiO Heterostructures”. In: *Phys. Rev. X* 9 (4 Oct. 2019), p. 041016. DOI: [10.1103/PhysRevX.9.041016](https://doi.org/10.1103/PhysRevX.9.041016).
- [9] Helena Reichlova et al. “Imaging and writing magnetic domains in the non-collinear anti-ferromagnet Mn₃Sn”. In: *Nature Communications* 10.1 (Nov. 2019). DOI: [10.1038/s41467-019-13391-z](https://doi.org/10.1038/s41467-019-13391-z).
- [10] I. Gross et al. “Real-space imaging of non-collinear antiferromagnetic order with a single-spin magnetometer”. In: *Nature* 549.7671 (July 2017), pp. 252–256. DOI: [10.1038/nature23656](https://doi.org/10.1038/nature23656).
- [11] J.-Y. Chauleau et al. “Multi-stimuli manipulation of antiferromagnetic domains assessed by second-harmonic imaging”. In: *Nature Materials* 16.8 (May 2017), pp. 803–807. DOI: [10.1038/nmat4899](https://doi.org/10.1038/nmat4899).
- [12] Jia Xu et al. “Imaging antiferromagnetic domains in nickel oxide thin films by optical birefringence effect”. In: *Physical Review B* 100.13 (Oct. 2019). DOI: [10.1103/physrevb.100.134413](https://doi.org/10.1103/physrevb.100.134413).
- [13] Ivan K. Schuller et al. “Role of the antiferromagnetic bulk spins in exchange bias”. In: *Journal of Magnetism and Magnetic Materials* 416 (Oct. 2016), pp. 2–9. DOI: [10.1016/j.jmmm.2016.04.065](https://doi.org/10.1016/j.jmmm.2016.04.065).
- [14] K. O’Grady, L.E. Fernandez-Outon, and G. Vallejo-Fernandez. “A new paradigm for exchange bias in polycrystalline thin films”. In: *Journal of Magnetism and Magnetic Materials* 322.8 (Apr. 2010), pp. 883–899. DOI: [10.1016/j.jmmm.2009.12.011](https://doi.org/10.1016/j.jmmm.2009.12.011).
- [15] Axel Hoffmann. “Spin Hall Effects in Metals”. In: *IEEE Transactions on Magnetics* 49.10 (Oct. 2013), 5172–5193. ISSN: 0018-9464. DOI: [10.1109/TMAG.2013.2262947](https://doi.org/10.1109/TMAG.2013.2262947).
- [16] Chi-Feng Pai et al. “Spin transfer torque devices utilizing the giant spin Hall effect of tungsten”. In: *Applied Physics Letters* 101.12 (Sept. 2012), p. 122404. DOI: [10.1063/1.4753947](https://doi.org/10.1063/1.4753947).

- [17] M.I. Dyakonov and V.I. Perel. “Current-induced spin orientation of electrons in semiconductors”. In: *Physics Letters A* 35.6 (July 1971), pp. 459–460. DOI: [10.1016/0375-9601\(71\)90196-4](https://doi.org/10.1016/0375-9601(71)90196-4).
- [18] J. E. Hirsch. “Spin Hall Effect”. In: *Physical Review Letters* 83.9 (Aug. 1999), pp. 1834–1837. DOI: [10.1103/physrevlett.83.1834](https://doi.org/10.1103/physrevlett.83.1834).
- [19] Y. K. Kato et al. “Observation of the Spin Hall Effect in Semiconductors”. In: *Science* 306.5703 (Dec. 2004), pp. 1910–1913. DOI: [10.1126/science.1105514](https://doi.org/10.1126/science.1105514).
- [20] H. Nakayama et al. “Spin Hall Magnetoresistance Induced by a Nonequilibrium Proximity Effect”. In: *Physical Review Letters* 110.20 (May 2013), p. 206601. DOI: [10.1103/physrevlett.110.206601](https://doi.org/10.1103/physrevlett.110.206601).
- [21] Geert R. Hoogeboom et al. “Negative spin Hall magnetoresistance of Pt on the bulk easy-plane antiferromagnet NiO”. In: *Applied Physics Letters* 111.5 (July 2017), p. 052409. DOI: [10.1063/1.4997588](https://doi.org/10.1063/1.4997588).
- [22] Johanna Fischer et al. “Spin Hall magnetoresistance in antiferromagnet/heavy-metal heterostructures”. In: *Phys. Rev. B* 97 (1 Jan. 2018), p. 014417. DOI: [10.1103/PhysRevB.97.014417](https://doi.org/10.1103/PhysRevB.97.014417).
- [23] Lise Meitner. “Über den Zusammenhang zwischen a- und b-Strahlen”. In: *Zeitschrift für Physik* 9.1 (Dec. 1922), pp. 145–152. DOI: [10.1007/bf01326963](https://doi.org/10.1007/bf01326963).
- [24] G Bradley Armen et al. “The resonant Auger effect”. In: *Journal of Physics B: Atomic, Molecular and Optical Physics* 33.2 (Jan. 2000), R49–R92. DOI: [10.1088/0953-4075/33/2/201](https://doi.org/10.1088/0953-4075/33/2/201).
- [25] J. Stohr and S. Anders. “X-ray spectro-microscopy of complex materials and surfaces”. In: *IBM Journal of Research and Development* 44.4 (July 2000), pp. 535–551. DOI: [10.1147/rd.444.0535](https://doi.org/10.1147/rd.444.0535).

- [26] G. Schütz et al. “Absorption of circularly polarized x rays in iron”. In: *Physical Review Letters* 58.7 (Feb. 1987), pp. 737–740. DOI: [10.1103/physrevlett.58.737](https://doi.org/10.1103/physrevlett.58.737).
- [27] Arne Brataas, Andrew D. Kent, and Hideo Ohno. “Current-induced torques in magnetic materials”. In: *Nature Materials* 11.5 (Apr. 2012), pp. 372–381. DOI: [10.1038/nmat3311](https://doi.org/10.1038/nmat3311).
- [28] Samik DuttaGupta et al. “Spin-orbit torque switching of an antiferromagnetic metallic heterostructure”. In: *Nature Communications* 11.1 (Nov. 2020). DOI: [10.1038/s41467-020-19511-4](https://doi.org/10.1038/s41467-020-19511-4).
- [29] Yang Cheng et al. “Electrical Switching of Tristate Antiferromagnetic Néel Order in α -Fe₂O₃ Epitaxial Films”. In: *Phys. Rev. Lett.* 124 (2 Jan. 2020), p. 027202. DOI: [10.1103/PhysRevLett.124.027202](https://doi.org/10.1103/PhysRevLett.124.027202).
- [30] Xianfeng Liang et al. “A Review of Thin-Film Magnetoelastic Materials for Magnetoelectric Applications”. In: *Sensors* 20.5 (Mar. 2020), p. 1532. DOI: [10.3390/s20051532](https://doi.org/10.3390/s20051532).
- [31] Pengxiang Zhang et al. “Quantitative Study on Current-Induced Effect in an Antiferromagnet Insulator/Pt Bilayer Film”. In: *Phys. Rev. Lett.* 123 (24 Dec. 2019), p. 247206. DOI: [10.1103/PhysRevLett.123.247206](https://doi.org/10.1103/PhysRevLett.123.247206).
- [32] J.C. Slonczewski. “Current-driven excitation of magnetic multilayers”. In: *Journal of Magnetism and Magnetic Materials* 159.1-2 (June 1996), pp. L1–L7. DOI: [10.1016/0304-8853\(96\)00062-5](https://doi.org/10.1016/0304-8853(96)00062-5).
- [33] L. Berger. “Emission of spin waves by a magnetic multilayer traversed by a current”. In: *Physical Review B* 54.13 (Oct. 1996), pp. 9353–9358. DOI: [10.1103/physrevb.54.9353](https://doi.org/10.1103/physrevb.54.9353).
- [34] Ran Cheng, Di Xiao, and Arne Brataas. “Terahertz Antiferromagnetic Spin Hall Nano-Oscillator”. In: *Phys. Rev. Lett.* 116 (20 May 2016), p. 207603. DOI: [10.1103/PhysRevLett.116.207603](https://doi.org/10.1103/PhysRevLett.116.207603).

- [35] Junxue Li et al. “Spin current from sub-terahertz-generated antiferromagnetic magnons”. In: *Nature* 578.7793 (Jan. 2020), pp. 70–74. DOI: [10.1038/s41586-020-1950-4](https://doi.org/10.1038/s41586-020-1950-4).
- [36] Priyanka Vaidya et al. “Subterahertz spin pumping from an insulating antiferromagnet”. In: *Science* 368.6487 (2020), pp. 160–165.
- [37] P. Wadley et al. “Electrical switching of an antiferromagnet”. In: *Science* 351.6273 (Jan. 2016), p. 587. DOI: [10.1126/science.aab1031](https://doi.org/10.1126/science.aab1031).
- [38] K. Olejnik et al. “Antiferromagnetic CuMnAs multi-level memory cell with microelectronic compatibility”. In: *Nature Communications* 8.1 (May 2017). DOI: [10.1038/ncomms15434](https://doi.org/10.1038/ncomms15434).
- [39] S. Yu. Bodnar et al. “Writing and reading antiferromagnetic Mn₂Au by Néel spin-orbit torques and large anisotropic magnetoresistance”. In: *Nature Communications* 9.1 (Jan. 2018).
- [40] H. Meer et al. *Direct imaging of current-induced antiferromagnetic switching revealing a pure thermomagnetoelastic switching mechanism*. 2020.
- [41] C. C. Chiang et al. “Absence of Evidence of Electrical Switching of the Antiferromagnetic Néel Vector”. In: *Phys. Rev. Lett.* 123 (22 Nov. 2019), p. 227203. DOI: [10.1103/PhysRevLett.123.227203](https://doi.org/10.1103/PhysRevLett.123.227203).
- [42] A. Churikova et al. “Non-magnetic origin of spin Hall magnetoresistance-like signals in Pt films and epitaxial NiO/Pt bilayers”. In: *Applied Physics Letters* 116.2 (2020), p. 022410. DOI: [10.1063/1.5134814](https://doi.org/10.1063/1.5134814).
- [43] V. Baltz et al. “Antiferromagnetic spintronics”. In: *Rev. Mod. Phys.* 90 (1 Feb. 2018), p. 015005. DOI: [10.1103/RevModPhys.90.015005](https://doi.org/10.1103/RevModPhys.90.015005).
- [44] Ioan Mihai Miron et al. “Perpendicular switching of a single ferromagnetic layer induced by in-plane current injection”. In: *Nature* 476.7359 (Aug. 2011), p. 189. ISSN: 0028-0836. DOI: [{10.1038/nature10309}](https://doi.org/10.1038/nature10309).

- [45] Luqiao Liu et al. “Spin-Torque Switching with the Giant Spin Hall Effect of Tantalum”. In: *Science* 336.6081 (May 2012), 555–558. ISSN: 0036-8075. DOI: [10.1126/science.1218197](https://doi.org/10.1126/science.1218197).
- [46] X. Z. Chen et al. “Antidamping-Torque-Induced Switching in Biaxial Antiferromagnetic Insulators”. In: *Phys. Rev. Lett.* 120 (20 May 2018), p. 207204. DOI: [10.1103/PhysRevLett.120.207204](https://doi.org/10.1103/PhysRevLett.120.207204).
- [47] Markus Meinert, Dominik Graulich, and Tristan Matalla-Wagner. “Electrical Switching of Antiferromagnetic Mn₂Au and the Role of Thermal Activation”. In: *Phys. Rev. Applied* 9 (6 June 2018), p. 064040. DOI: [10.1103/PhysRevApplied.9.064040](https://doi.org/10.1103/PhysRevApplied.9.064040).
- [48] X. F. Zhou et al. “Strong Orientation-Dependent Spin-Orbit Torque in Thin Films of the Antiferromagnet Mn₂Au”. In: *Phys. Rev. Applied* 9 (5 May 2018), p. 054028. DOI: [10.1103/PhysRevApplied.9.054028](https://doi.org/10.1103/PhysRevApplied.9.054028).
- [49] Pengxiang Zhang et al. “Quantitative Study on Current-Induced Effect in an Antiferromagnet Insulator/Pt Bilayer Film”. In: *Phys. Rev. Lett.* 123 (24 Dec. 2019), p. 247206. DOI: [10.1103/PhysRevLett.123.247206](https://doi.org/10.1103/PhysRevLett.123.247206).
- [50] Takahiro Moriyama et al. “Spin torque control of antiferromagnetic moments in NiO”. In: *Scientific Reports* 8.1 (Sept. 2018), p. 14167.
- [51] Baldrati, L. and Gomonay, O. and Ross, A. and Filianina, M. and Lebrun, R. and Ramos, R. and Leveille, C. and Fuhrmann, F. and Forrest, T. R. and Maccherozzi, F. and Valencia, S. and Kronast, F. and Saitoh, E. and Sinova, J. and Kläui, M. “Mechanism of Néel Order Switching in Antiferromagnetic Thin Films Revealed by Magnetotransport and Direct Imaging”. In: *Phys. Rev. Lett.* 123 (17 Oct. 2019), p. 177201. DOI: [10.1103/PhysRevLett.123.177201](https://doi.org/10.1103/PhysRevLett.123.177201).
- [52] S. Yu. Bodnar et al. “Imaging of current induced Néel vector switching in antiferromagnetic Mn₂Au”. In: *Physical Review B* 99.14 (Apr. 2019). DOI: [10.1103/physrevb.99.140409](https://doi.org/10.1103/physrevb.99.140409).

- [53] T. Janda et al. “Magneto-Seebeck microscopy of domain switching in collinear antiferromagnet CuMnAs”. In: *Physical Review Materials* 4.9 (Sept. 2020). DOI: [10.1103/physrevmaterials.4.094413](https://doi.org/10.1103/physrevmaterials.4.094413).
- [54] A. H. Morrish. *Canted Antiferromagnetism: Hematite*. World Scientific, Jan. 1995. DOI: [10.1142/2518](https://doi.org/10.1142/2518).
- [55] Tatsuo Fujii et al. “Spin-flip anomalies in epitaxial α -Fe₂O₃ films by Mössbauer spectroscopy”. In: *Journal of Magnetism and Magnetic Materials* 135.2 (July 1994), pp. 231–236. DOI: [10.1016/0304-8853\(94\)90351-4](https://doi.org/10.1016/0304-8853(94)90351-4).
- [56] Andrew Doran et al. “Cryogenic PEEM at the Advanced Light Source”. In: *Journal of Electron Spectroscopy and Related Phenomena* 185.10 (2012), p. 340. ISSN: 0368-2048. DOI: <https://doi.org/10.1016/j.elspec.2012.05.005>.
- [57] Pieter Kuiper et al. “X-ray magnetic dichroism of antiferromagnet Fe₂O₃: The orientation of magnetic moments observed by Fe 2p x-ray absorption spectroscopy”. In: *Phys. Rev. Lett.* 70 (10 Mar. 1993), pp. 1549–1552. DOI: [10.1103/PhysRevLett.70.1549](https://doi.org/10.1103/PhysRevLett.70.1549).
- [58] A. Scholl. “Observation of Antiferromagnetic Domains in Epitaxial Thin Films”. In: *Science* 287.5455 (Feb. 2000), pp. 1014–1016. DOI: [10.1126/science.287.5455.1014](https://doi.org/10.1126/science.287.5455.1014).
- [59] SeongHun Park et al. “Strain control of Morin temperature in epitaxial α -Fe₂O₃ (0001) film”. In: *EPL (Europhysics Letters)* 103.2 (July 2013), p. 27007. DOI: [10.1209/0295-5075/103/27007](https://doi.org/10.1209/0295-5075/103/27007).
- [60] Jean-Michel Kiat et al. “Monoclinic structure of unpoled morphotropic high piezoelectric PMN-PT and PZN-PT compounds”. In: *Physical Review B* 65.6 (Jan. 2002). DOI: [10.1103/physrevb.65.064106](https://doi.org/10.1103/physrevb.65.064106).
- [61] F. L. A. Machado et al. “Spin-flop transition in the easy-plane antiferromagnet nickel oxide”. In: *Physical Review B* 95.10 (Mar. 2017). DOI: [10.1103/physrevb.95.104418](https://doi.org/10.1103/physrevb.95.104418).

- [62] Lucia Aballe et al. “The ALBA spectroscopic LEEM-PEEM experimental station: layout and performance”. In: *Journal of Synchrotron Radiation* 22.3 (Apr. 2015), pp. 745–752. DOI: [10.1107/s1600577515003537](https://doi.org/10.1107/s1600577515003537).
- [63] C. Schmitt et al. “Identification of Néel Vector Orientation in Antiferromagnetic Domains Switched by Currents in NiO/Pt Thin Films”. In: *Phys. Rev. Applied* 15 (3 Mar. 2021), p. 034047. DOI: [10.1103/PhysRevApplied.15.034047](https://doi.org/10.1103/PhysRevApplied.15.034047).
- [64] E. V. Gomonay and V. M. Loktev. “Spintronics of antiferromagnetic systems (Review Article)”. In: *Low Temperature Physics* 40.1 (Jan. 2014), pp. 17–35. DOI: [10.1063/1.4862467](https://doi.org/10.1063/1.4862467).
- [65] T. Jungwirth et al. “Antiferromagnetic spintronics”. In: *Nature Nanotechnology* 11.3 (Mar. 2016), pp. 231–241. DOI: [10.1038/nnano.2016.18](https://doi.org/10.1038/nnano.2016.18).
- [66] V. Baltz et al. “Antiferromagnetic spintronics”. In: *Rev. Mod. Phys.* 90 (1 Feb. 2018), p. 015005. DOI: [10.1103/RevModPhys.90.015005](https://doi.org/10.1103/RevModPhys.90.015005).
- [67] Shunsuke Fukami, Virginia O. Lorenz, and Olena Gomonay. “Antiferromagnetic spintronics”. In: *Journal of Applied Physics* 128.7 (Aug. 2020), p. 070401. DOI: [10.1063/5.0023614](https://doi.org/10.1063/5.0023614).
- [68] Egecan Cogulu et al. “Direct imaging of electrical switching of antiferromagnetic Néel order in α -Fe₂O₃ epitaxial films”. In: *Phys. Rev. B* 103 (10 Mar. 2021), p. L100405. DOI: [10.1103/PhysRevB.103.L100405](https://doi.org/10.1103/PhysRevB.103.L100405).
- [69] Helen V. Gomonay and Vadim M. Loktev. “Spin transfer and current-induced switching in antiferromagnets”. In: *Phys. Rev. B* 81 (14 Apr. 2010), p. 144427. DOI: [10.1103/PhysRevB.81.144427](https://doi.org/10.1103/PhysRevB.81.144427).
- [70] Ran Cheng et al. “Spin Pumping and Spin-Transfer Torques in Antiferromagnets”. In: *Phys. Rev. Lett.* 113 (5 July 2014), p. 057601. DOI: [10.1103/PhysRevLett.113.057601](https://doi.org/10.1103/PhysRevLett.113.057601).
- [71] Can Onur Avci et al. “Interplay of spin-orbit torque and thermoelectric effects in ferromagnet/normal-metal bilayers”. In: *Phys. Rev. B* 90 (22 Dec. 2014), p. 224427.

- [72] Arun Parthasarathy et al. “Precessional spin-torque dynamics in biaxial antiferromagnets”. In: *Phys. Rev. B* 103 (2 Jan. 2021), p. 024450. DOI: [10.1103/PhysRevB.103.024450](https://doi.org/10.1103/PhysRevB.103.024450).
- [73] Qiming Shao et al. “Roadmap of Spin–Orbit Torques”. In: *IEEE Transactions on Magnetics* 57.7 (July 2021), pp. 1–39. DOI: [10.1109/tmag.2021.3078583](https://doi.org/10.1109/tmag.2021.3078583).
- [74] Lijun Zhu, Daniel C. Ralph, and Robert A. Buhrman. “Maximizing spin-orbit torque generated by the spin Hall effect of Pt”. In: *Applied Physics Reviews* 8.3 (2021), p. 031308. DOI: [10.1063/5.0059171](https://doi.org/10.1063/5.0059171).
- [75] L. Baldrati et al. “Full angular dependence of the spin Hall and ordinary magnetoresistance in epitaxial antiferromagnetic NiO(001)/Pt thin films”. In: *Phys. Rev. B* 98 (2 July 2018), p. 024422. DOI: [10.1103/PhysRevB.98.024422](https://doi.org/10.1103/PhysRevB.98.024422).
- [76] Yang Cheng et al. “Anisotropic magnetoresistance and nontrivial spin Hall magnetoresistance in Pt/ α -Fe₂O₃ bilayers”. In: *Phys. Rev. B* 100 (22 Dec. 2019), p. 220408. DOI: [10.1103/PhysRevB.100.220408](https://doi.org/10.1103/PhysRevB.100.220408).
- [77] G. Y. Guo et al. “Intrinsic Spin Hall Effect in Platinum: First-Principles Calculations”. In: *Physical Review Letters* 100.9 (Mar. 2008), p. 096401. DOI: [10.1103/physrevlett.100.096401](https://doi.org/10.1103/physrevlett.100.096401).
- [78] Yan-Ting Chen et al. “Theory of spin Hall magnetoresistance”. In: *Phys. Rev. B* 87 (14 Apr. 2013), p. 144411. DOI: [10.1103/PhysRevB.87.144411](https://doi.org/10.1103/PhysRevB.87.144411).
- [79] Tomohiro Taniguchi, J. Grollier, and M. D. Stiles. “Spin-Transfer Torques Generated by the Anomalous Hall Effect and Anisotropic Magnetoresistance”. In: *Physical Review Applied* 3.4 (Apr. 2015), p. 044001. DOI: [10.1103/physrevapplied.3.044001](https://doi.org/10.1103/physrevapplied.3.044001).
- [80] Masamitsu Hayashi et al. “Quantitative characterization of the spin-orbit torque using harmonic Hall voltage measurements”. In: *Phys. Rev. B* 89 (14 Apr. 2014), p. 144425. DOI: [10.1103/PhysRevB.89.144425](https://doi.org/10.1103/PhysRevB.89.144425).

- [81] R. Lebrun et al. “Anisotropies and magnetic phase transitions in insulating antiferromagnets determined by a Spin-Hall magnetoresistance probe”. In: *Communications Physics* 2 (May 2019), p. 50. DOI: [10.1038/s42005-019-0150-8](https://doi.org/10.1038/s42005-019-0150-8).
- [82] M.H. Seavey. “Acoustic resonance in the easy-plane weak ferromagnets α -Fe₂O₃ and FeBO₃”. In: *Solid State Communications* 10.2 (Jan. 1972), pp. 219–223. DOI: [10.1016/0038-1098\(72\)90385-7](https://doi.org/10.1016/0038-1098(72)90385-7).
- [83] Hantao Zhang and Ran Cheng. “Theory of the Harmonic Hall Responses of Spin-Torque Driven Antiferromagnets”. In: *arXiv.org* (2021). DOI: [10.48550/ARXIV.2112.12772](https://doi.org/10.48550/ARXIV.2112.12772).
- [84] Samuel J. Williamson and Simon Foner. “Antiferromagnetic Resonance in Systems with Dzyaloshinsky-Moriya Coupling; Orientation Dependence in α -Fe₂O₃”. In: *Phys. Rev.* 136 (4A Nov. 1964), A1102–A1106. DOI: [10.1103/PhysRev.136.A1102](https://doi.org/10.1103/PhysRev.136.A1102).
- [85] Koichi Mizushima and Shuichi Iida. “Effective In-Plane Anisotropy Field in α -Fe₂O₃”. In: *Journal of the Physical Society of Japan* 21.8 (Aug. 1966), pp. 1521–1526. DOI: [10.1143/jpsj.21.1521](https://doi.org/10.1143/jpsj.21.1521).
- [86] P. R. Elliston and G. J. Troup. “Some antiferromagnetic resonance measurements in α -Fe₂O₃”. In: *Journal of Physics C Solid State Physics* 1.1 (Feb. 1968), pp. 169–178. DOI: [10.1088/0022-3719/1/1/320](https://doi.org/10.1088/0022-3719/1/1/320).
- [87] Gerrit E. W. Bauer, Eiji Saitoh, and Bart J. van Wees. “Spin caloritronics”. In: *Nature Materials* 11.5 (Apr. 2012), pp. 391–399. DOI: [10.1038/nmat3301](https://doi.org/10.1038/nmat3301).
- [88] Yaroslav Tserkovnyak, Arne Brataas, and Gerrit EW Bauer. “Spin pumping and magnetization dynamics in metallic multilayers”. In: *Physical Review B* 66.22 (2002), p. 224403.
- [89] K Xia et al. “Spin torques in ferromagnetic/normal-metal structures”. In: *Physical Review B* 65.22 (2002), p. 220401.

- [90] Ran Cheng. “Aspects of antiferromagnetic spintronics”. PhD thesis. The University of Texas at Austin, 2014.
- [91] Ran Cheng et al. “Spin pumping and spin-transfer torques in antiferromagnets”. In: *Physical review letters* 113.5 (2014), p. 057601.
- [92] Yizhang Chen et al. “First harmonic measurements of the spin Seebeck effect”. In: *Applied Physics Letters* 113.20 (Nov. 2018), p. 202403. DOI: [10.1063/1.5053120](https://doi.org/10.1063/1.5053120).
- [93] Lauren J. Riddiford et al. “Efficient spin current generation in low-damping $\text{Mg}(\text{Al}, \text{Fe})_2\text{O}_4$ thin films”. In: *Applied Physics Letters* 115.12 (Sept. 2019), p. 122401. DOI: [10.1063/1.5119726](https://doi.org/10.1063/1.5119726).
- [94] Yizhang Chen et al. “Spin transport in an insulating ferrimagnetic-antiferromagnetic-ferrimagnetic trilayer as a function of temperature”. In: *AIP Advances* 9.10 (Oct. 2019), p. 105319. DOI: [10.1063/1.5116549](https://doi.org/10.1063/1.5116549).
- [95] L. Rehm et al. “Thermal Effects in Spin-Torque Switching of Perpendicular Magnetic Tunnel Junctions at Cryogenic Temperatures”. In: *Physical Review Applied* 15.3 (Mar. 2021). DOI: [10.1103/physrevapplied.15.034088](https://doi.org/10.1103/physrevapplied.15.034088).
- [96] Egecan Cogulu et al. “Quantifying Spin-Orbit Torques in Antiferromagnet/Heavy Metal Heterostructures”. In: (2021). DOI: [10.48550/ARXIV.2112.12238](https://doi.org/10.48550/ARXIV.2112.12238).
- [97] Yang Cheng et al. “Third Harmonic Characterization of Antiferromagnetic Heterostructures”. In: (2021). DOI: [10.48550/ARXIV.2112.13159](https://doi.org/10.48550/ARXIV.2112.13159).
- [98] K. Uchida et al. “Observation of the spin Seebeck effect”. In: *Nature* 455.7214 (Oct. 2008), pp. 778–781. DOI: [10.1038/nature07321](https://doi.org/10.1038/nature07321).

ProQuest Number: 29061944

INFORMATION TO ALL USERS

The quality and completeness of this reproduction is dependent on the quality and completeness of the copy made available to ProQuest.



Distributed by ProQuest LLC (2022).

Copyright of the Dissertation is held by the Author unless otherwise noted.

This work may be used in accordance with the terms of the Creative Commons license or other rights statement, as indicated in the copyright statement or in the metadata associated with this work. Unless otherwise specified in the copyright statement or the metadata, all rights are reserved by the copyright holder.

This work is protected against unauthorized copying under Title 17,
United States Code and other applicable copyright laws.

Microform Edition where available © ProQuest LLC. No reproduction or digitization of the Microform Edition is authorized without permission of ProQuest LLC.

ProQuest LLC
789 East Eisenhower Parkway
P.O. Box 1346
Ann Arbor, MI 48106 - 1346 USA